Principal Investigator - Final Report
November 1, 2009 – September 30, 2015
Date of Report: January 31, 2016

Award Number:	DE-EE0000366
Project Title:	Center for Efficiency in Sustainable Energy Systems Task 1: Improved Energy Efficiency for Industrial Processes Task 2: Analysis of a Solid Oxide Fuel Cell Operating on Landfill Gas Task 3 Demonstration of an Urban Wind Turbine System
Project Period:	November 1, 2009 to September 30, 2015
Recipient Organization:	Youngstown State University
Partners:	Task 1: none Task 2: NexTech Materials Task 3: Orbital Research
Technical Contact:	Martin Abraham, One University Plaza, Youngstown, OH 44555, 330.941.3103, martin.abraham@ysu.edu
Business Contact:	Michael A. Hripko, One University Plaza, Youngstown, OH 44555, 330-941-3091, facsimile 330.941.2075, mahripkon@ysu.edu

---

1. **Project Objective:**

The main goal of the *Center for Efficiency in Sustainable Energy Systems* is to produce a methodology that evaluates a variety of energy systems. The methodology reviews process performance, life cycle, and financial aspects common to many processes. The program will evaluate processes at energy-intensive manufacturing facilities, and apply principles developed through this analysis on a sustainable energy storage technology (fuel cells) and a sustainable energy generation technology (wind).

2. **Background:**

Task I. Improved Energy Efficiency for Industrial Processes: This task, completed in partnership with area manufacturers, analyzes the operation of complex manufacturing facilities to provide flexibilities that allow them to improve active-mode power efficiency, lower standby-mode power consumption, and use low cost energy resources to control energy costs in meeting their economic incentives; (2) Identify devices for the efficient transformation of instantaneous or continuous power to different devices and sections of industrial plants; and (3) use these manufacturing sites to demonstrate and validate general principles of power management.

Task II. Analysis of a solid oxide fuel cell operating on landfill gas: This task consists of: (1) analysis of a typical landfill gas; (2) establishment of a comprehensive design of the fuel cell system (including the SOFC stack and BOP), including durability analysis; (3) development of suitable reforming methods and catalysts that are tailored to the specific SOFC system concept; and (4) SOFC stack fabrication with testing to demonstrate the salient operational characteristics of the stack, including an analysis of the overall energy conversion efficiency of the system.

Task III. Demonstration of an urban wind turbine system: This task consists of (1) design and construction of two side-by-side wind turbine systems on the YSU campus, integrated through power control systems with grid power; (2) preliminary testing of aerodynamic control effectors (provided by a small business partner) to demonstrate improved power control, and evaluation of the system performance, including economic estimates of viability in an urban environment; and (3) computational analysis of the wind turbine system as an enabling activity for development of smart rotor blades that contain integrated sensor/actuator/controller modules to enhance energy capture and reduce aerodynamic loading and noise by way of virtual aerodynamic shaping.

3. **Project Accomplishments/Results:**

Task 1 Industrial Assessment

Subtask 1.1. Project Management.

During the many years of this project, various individuals have been engaged in the activities; however, Dr. Martin Abraham has remained as the administrative lead throughout. Following completion of the contract, technical and budgetary reports were provided in a timely fashion. The PI worked with University administration and sub-contract recipients to ensure completion of tasks, and with university facilities personnel for the installation of wind turbines on campus.

Although completion of the final report represents the last formal activity within this grant, YSU personnel will continue to monitor the performance of the wind turbines to ensure their use as learning instruments for YSU students.

The 3rd Sustainable Energy Forum was conducted at YSU June 5 – 7, 2011. With over 200 participants, this forum reached new heights both in attendees and participation of distinguished speakers. Featured speakers included Dr. Dr. Henry Kelly, Acting Assistant Secretary and Principal Deputy Assistant Secretary for the Office of Energy Efficiency and Renewable Energy (EERE), US Department of Energy, Congressman Tim Ryan (OH-17), and Mr. Eric Spiegel, President and CEO of Siemens America. The forum provided an excellent opportunity for networking among industry leaders, government officials, and researchers.

The 4th and 5th Sustainable Energy Forum were subsequently held in June 2012 and June 2013, with a series of speakers representing the manufacturing community. National speakers were selected from key constituencies. Roughly 150 – 200 individuals attended each event.

Although not a direct focus of this effort, During the past quarter, YSU completed installation of the 57 kW solar array on the roof of Moser Hall in 3rd quarter 2011. Information is included in a brief article available on the STEM website at http://ysustem.wordpress.com/2011/10/26/solar-panels-installed-on-roof-of-moser-hall/. Output from the array is also reported via the web at http://live.deckmonitoring.com/?id=youngstown_state_university. In 2012, connectivity to this array was made through a kiosk display at OH Wow, the children's science museum located in downtown Youngstown, providing broader access of this information to the community.

Subtask 1.2 Energy audits.
We organized an energy management training session held on February 22, 2011, which was advertised through a regional manufacturing association to provide wide-ranging notification. During the 90 minute presentation, Professor Costarell discussed the national trends for the cost of oil natural gas and their relationship to the economy. A major observation was that 7000 Btu of energy are needed for every dollar of GDP. This is down from twice the energy needed per dollar back in the 1940's, indicating that the economy is less focused on heavy industry. Also observed was that the major focus of energy reduction was on industrial users, not residential users. Though both groups use a similar amount of energy there are 124,000,000 residential customers in the US (2007) compared to only 800,000 industrial customers, a factor of 150 times larger.

Over two dozen companies were represented a the seminar, ranging from heavy manufacturing businesses with $5,000,000 per year energy expenses, to small, light manufacturing facilities. Also present were representatives from the Congressional District Ohio
17 and the Ohio Department of Development. Several sites were identified for visits. Following the workshop, YSU faculty and students assessed the energy use of two local businesses and identified low cost energy savings opportunities with very short returns on investment.

The first business was a light-manufacturing company that assembles eye glasses. The 5,000 sf facility has older T12 lighting which easily qualifies for upgrades with 2 to 3 year paybacks. The site was referred to participate in the First Energy Commercial Lighting Program, where $800 per kW of lighting costs is rebated to the facility.

The second site was a hydraulic distribution center with minimal repair and assembly functions. The main electric loads for the 10,000 sf facility are lighting, mostly from 100W and 400W metal halide lamps. As with the previous audit, this site was referred to the First Energy Commercial Lighting Program where lighting replacement is likely to have a one year or less return on investment.

Overall, these sites had very little energy expense to begin with, so large dollar savings were not possible. As a result, the remaining audits will focus on the small to medium size industries with 500 employees or less and annual energy expenses in the $100,000 to $2,500,000 range.

Subtask 1.3. Integrate systems analysis methods

This task was planned to take place following completion of the energy audits conducted as subtask 1.2. Shortly after initiating work on that element, it became apparent that this would not be feasible, based on the information that was gained from the audits. As a result, this subtask was removed from the list of deliverables.

Task 2. Landfill Fuel Cell Power Generation

Solid Oxide Fuel Cells (SOFCs) were constructed and evaluated as a means of obtaining electrical energy from landfill gas.

Subtask 2.1 Analysis of landfill gas.

After several false starts, we were able to secure access to the Mahoning Landfill in New Springfield. We developed the chromatographic capability for quantitating the principal gases coming from the landfill: CH_4, CO_2, and N_2. We have also mastered the use of RAE tubes for analyzing H_2S levels. Their CH_4 concentration is just > 50% of total gaseous effluent, while CO_2 is 36%. The balance is N_2. We have also determined that the H_2S concentration is 120 ppm. H_2S is usually the primary catalyst poison coming from landfills. For the purposes of this project, this constitutes sufficient characterization of the landfill gas composition.

Two trips were made to the Mahoning Landfill in New Springfield to collect samples of landfill gas. Inflatable, septum-sealed, half-liter Teflon bags were employed. Six gas samples were obtained on the August 9, 2011. These were used for general gas chromatographic-mass spectral analysis, as well as attempted determination of H_2S content. The initial chromatographic settings were not optimal, and will require adjustment to obtain reasonable spectra. A mass spectral analyzer specifically set to measure H_2S did not detect measurable levels. This led to speculation that the H_2S content was unstable and had somehow decomposed. It was resolved to return to the landfill and make immediate readings with RAE Gas Detection tubes. On the second trip, made on the September 7, 2011, on-the-spot-analysis of the landfill gas indicated that the landfill gas contained 120-140 ppm of hydrogen sulfide and 1-2 ppm of mercaptan. The bags were again tested immediately upon return to the lab and once again three days later. The apparent H_2S level had fallen to just over 100 ppm after return to campus, and 90 ppm three days later, indicating that the stagnant, contained landfill gas was losing on order of 10% of its H_2S content per day. This is certainly believable, as the landfill gas contains ~1%, or 10,000 ppm O_2, more than enough oxidant to completely consume the H_2S content. This has a bearing on the validity of bringing pressurized tanks of landfill gas back to the lab to test over a period of days.

To corroborate these readings, discussions commenced with the YSU Environmental Science department, which has an ICP (inductively coupled plasma) torch and an OES (optical emission spectrometer). The ICP-OES should easily be able to measure the nominal 120 ppm sulfur level. The spectrometer should also be able to measure Si, which is also an element of interest. It does not detect Cl, however. An adapter that allows gaseous sample introduction into the torch was ordered and received. A cylinder of CH_4 containing 100 ppm H_2S was obtained as a reference standard. Coupled with flowmeters and companion pure CH_4 or other gas cylinders, it should be possible to produce H_2S at any concentration and generate a calibration curve. However, the CGA 330 regulator for the spiked gas cylinder was found to be leaky and had to be returned to the manufacturer. Once this issue is resolved, ICP-OES measurement of sulfur content in landfill gas will proceed.

Two additional trips were made to the Mahoning Landfill in New Springfield to collect samples of landfill gas. This time one-liter Teflon gas sampling bags were employed, twice as large as previously. The larger sampling enabled us to obtain more 100 mL tests of the original sample before exhausting it. We also brought a 5-gallon empty propane tank to contain the gas. This was to be used for either ICP-OES analysis or long-term (up to one week) of operation of the NextCell⇔. An explosion-proof compressor was acquired to perform the filling of the tank. In the second visit, three 5-gallon tanks were filled and then plumbed together in the lab.

Two independent measurements of the landfill gas using two different chromatographic detectors ensured that we could quantitate the major constituents of the gas. The first detector employed was a Pulsed Discharge Helium Ionization Detector. The pulsed discharge ionization helium detector is a very sensitive and universal detector. Its sensitivity is 50 times better than methods using a flame ionization detector and 500 times better than thermal conductivity detectors. Landfill gas is known to contain numerous compounds in it and hence this technique was used to analyze landfill gas. GC-PDHID experiments were conducted using a Shimadzu–GC 2010 model. The column (shin carbon) was held at 35 °C for 5 min and then ramped at a rate of 6 °C per min for 25 min to reach 160 °C. The chromatogram is shown in Figure 2.1-1 below.

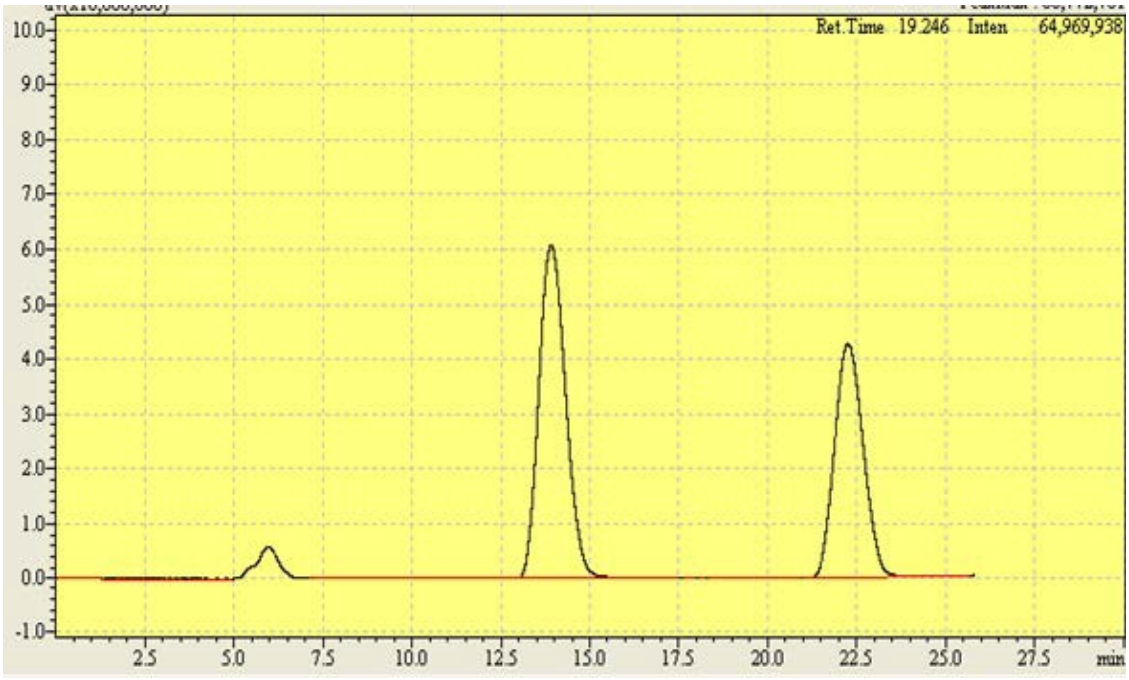

Figure 2.1-1. Gas chromatograph of landfill gas using a PDHID detector

The chromatogram from the PDHID showed three major peaks, which are, from left to right, an unresolved peak for nitrogen and oxygen, a methane peak, and a carbon dioxide peak. Minor constituents, including H_2S, were not observed.

If only large constituents are to be observed, a thermal conductivity detector (TCD) may work just as well. It is based on the difference between the thermal conductivities of the carrier gas (helium) and constituents of the analyte. In Figure 2.1-2 below, the major constituents present in the landfill gas are once again observed. The TCD was attached to a Varian gas chromatograph. The oven temperature was set to 220 °C. The flow was set to 10 mL/min. It had two columns: one analyzed carbon dioxide (Poropak) and the other column (molecular sieve) quantified for the other constituents of the landfill gas.

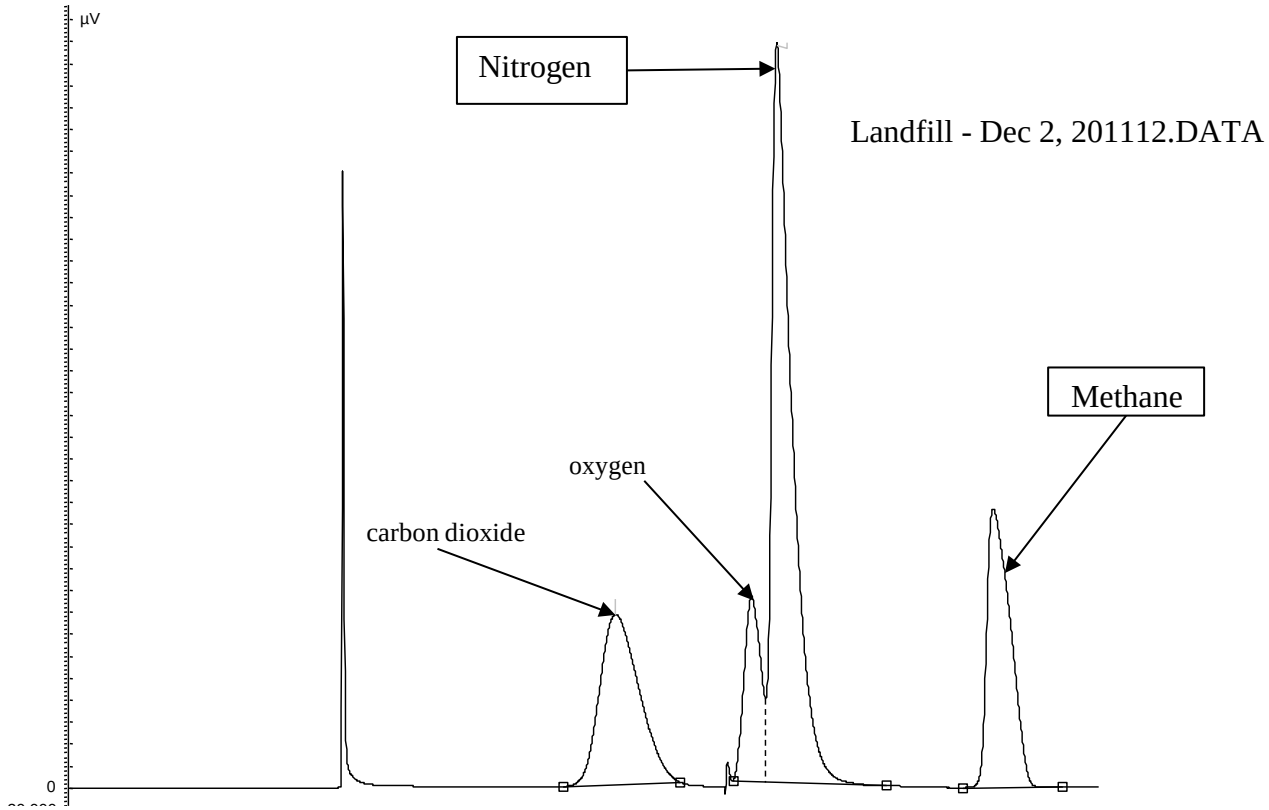

Figure 2.1-2. Gas chromatogram of landfill gas from a TCD detector

The ordering of the peaks changed from the PDHID experiment, due to the different columns involved, but in terms of composition the results are the same. The first peak from the left is just an artifact from switching columns. Continuing from left to right, CO_2, air, and methane were observed. Nearly complete resolution of the air peak into O_2 and N_2 was achieved. The composition of the landfill gas was calculated and is shown in Table 2.1-1 below. The results were close to the literature values and the data provided by the engineer at the landfill site.

Table 2.1-1. Landfill gas composition from TCD detector

Landfill gas (major constituents)	Concentrations
Methane	54%
Carbon dioxide	39%
Air	7%

Once again, no signal due to H_2S was observed, even though measurements at the landfill using RAE gas detection tubes showed 120 ppm. Examining the landfill gas-filled, 5-gallon propane tanks back at the lab showed zero H_2S residual only 3 h after filling. Even the Teflon sample bags lost their H_2S content over the course of a week. There is a fundamental instability in the landfill gas with respect to H_2S. Ostensibly it is the 1% O_2 content that ultimately consumes it. In the case of the propane tanks, there might be a catalytic effect on the walls of the tank, or the H_2S may be reacting with it directly, producing a thin skin of metal sulfides. Either way, it was

determined that while the major constituents of the landfill gas can be collected and stored, the reactive contaminants, which are predominately H_2S, are not.

One problem identified in the above analysis was that the integrated areas from the effluent gases were considerably smaller than the entering gases. There were two reasons for this anomaly. One was leakage through the alumina felt seals inside the furnace; the other was loss of sensitivity in the thermal conductivity detector. This latter effect was attributed to a build-up of water vapor inside the system. Our advice from the chromatograph manufacturer was that the system could handle small amounts of water. It is true that in terms of relative peak areas, the components determined by the gas chromatograph were roughly proportional, but trying to quantitate component amounts between runs was going to be impossible. Therefore, we added a molecular sieve bed between the ice water cold trap and the autosampler. With two stages of water vapor removal, the chromatograph readily delivered reproducible results.

Attempts at collecting gas samples at the landfill and evaluating them on campus were still unsuccessful. As shown below in Figure 2.1-3, even a Teflon® sample bag would lose its H_2S content over the course of a week. Therefore, in order to operate the fuel cell and demonstrate that it was operated on real landfill gas, it will be necessary to bring the fuel cell to the landfill and run it with gas immediately after it comes out of the ground.

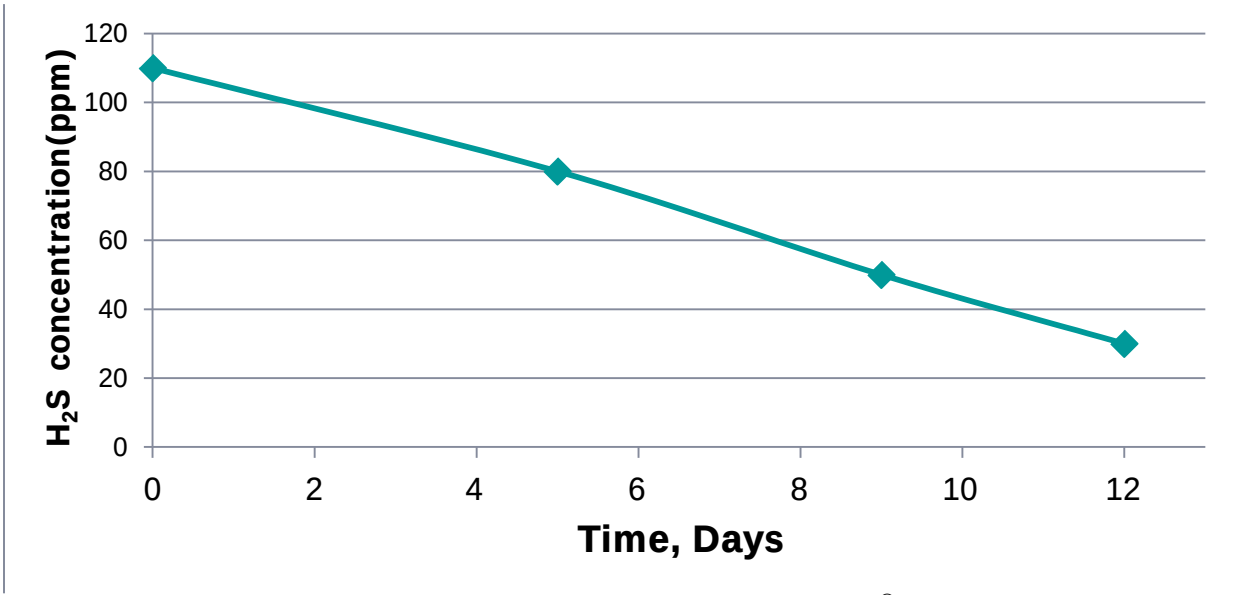

Figure 2.1-3. Decay of H_2S content inside a Teflon® sample bag.

Subtask 2.2 Assembly of an SOFC test cell.

Flat cell testing: A Lindberg/Blue M box furnace was acquired and modified to accommodate the Crofer^{V} (special high-temperature chromium/iron alloy) manifold plates necessary to contain the 28 cm^2 active area NextCell^{TM} electrode/electrolyte assembly. The modification consisted of drilling four holes through the rear of the furnace wall to the outside, fitting the rear panel with

0.375" brass bulkhead adapters, and inserting 0.25" i.d. alumina tubes through them to the furnace cavity. The alumina tubes act as thermally insulating guides for the Crofer inlet and outlet manifold tubes. The alumina guide tubes also serve to electrically isolate the body of the furnace from the galvanic potential that is generated inside the fuel cell.

High temperature (750 ^{o}C) N_2 leak-testing of the fuel cell was performed by attaching gas flow meters fore and aft of the manifold tubes and observing the relative flow rate. The single cell assembly consisted of the NextCell, two alumina fiber gaskets, and a silver mesh cathode current collector and a nickel mesh anode current collector sandwiched between the Crofer manifold plates. The NextCell assembly itself consists of a lanthanum manganite cathode, a scandia-stabilized zirconia ceramic electrolyte, and a nickel-zirconia cermet anode. Five pounds per square inch pressure was applied to the Crofer plates. Pressure was applied via barbell weights stacked onto a vertically oriented, 1" stainless steel (#304) shaft. The shaft neatly breaches the furnace wall through a fume exhaust port in the top of the furnace. To hold the weights steady, a steel chuck was designed and machined to fit on the upper end of the stainless shaft. It accommodated a cold finished #1018 steel rod onto which the weights were stacked. The total weight of steel shafts, chuck, and barbells is 65 lb, corresponding to 5 lb/in^2. The planar fuel cell assembly essentially fills the bottom of the furnace cavity, so no subsidence of the furnace floor is expected. Once again, to isolate the fuel cell voltage from the body of the furnace, it is necessary to place an alumina felt pad underneath the steel shaft where it touches the top Crofer plate.

Some gas leakage was observed even after heating to 750 ^{o}C for several hours; to resolve this issue it was necessary to wet the gaskets with an alumina slurry supplied by NexTech to fill the voids between the fibers before bringing to temperature.

Button cell testing: External voltage was applied to the button cell consisting of a bare scandia-zirconia circular wafer (button) electrolyte under air atmosphere and contacted by Pt wire to observe electrolytic O_2 pumping. The wires functionally act as contact electrodes and current collectors. The contact area is quite small in this configuration, however, so that the resistance of the cell at 750 ^{o}C was on order of 7400 Ω. This makes for sub-milliampere currents, which would be difficult to monitor.

To lower cell resistance, it will be necessary to sinter porous electrode deposits onto the electrolyte wafer, in a similar manner that is done for commercial SOFC's. To develop our capability in this regard and have a standard of comparison to subsequent electrode formulations, it was attempted to deposit porous platinum electrodes. A reference was found where said electrodes could be deposited using chloroplatinic acid. A concentrated aqueous solution of H_2PtCl_6 was applied to an electrolyte wafer, dried, and heated to 500 ^{o}C. Much effort was expended attempting to make this fabrication procedure succeed. Thermogravimetric analysis of $H_2PtCl_6 \cdot xH_2O$ confirmed that the vendor-guaranteed metals basis was obtained at the recommended processing temperature. However, the Pt deposit spread across the entire wafer, moving around the edge and onto the underside. The deposit was moderately electrically conductive, on order of 100's of ohms. Apparently a heavy vapor of $PtCl_4$ travels across the electrolyte before decomposing to the metal. Various masking agents were applied with limited success.

Earlier references (e.g., D. Braunshtein, D.S. Tannhauser, and I. Riess, Solid State Ionics, **3/4** (1981) 509-512) on SOFC test cells refer to "Pt paste" electrodes. These were generated by applying a solution referred to as "Liquid Bright Platinum." Actually, there are many such

solutions in the electroless plating business; our intent was to avoid those containing Ag or Au. We finally located a vendor for Liquid Bright Platinum #6082, which contains fine suspended Pt particles, and after firing contains Pt only. A transition of owners in recent years made it difficult to find. A 25 g quantity of the Pt paste precursor was ordered and used to prepare porous electrodes.

Preparations to deposit nickel-zirconia cermet anodes also progressed. We had purchased electrolyte wafers with the $LaMnO_3$ cathode already attached, since our interest is focused on the effect of landfill gas on the anode. However, it was determined that the cermet anode needed to be sintered at a temperature much higher than what is used to sinter the cathode (1400 ^oC versus 1100 ^oC). Exposing the cathode to 1400 ^oC would fully close the porous structure necessary to maintain high contact area. Thus it was necessary to deposit anode first to a plain electrolyte wafer and then follow with the cathode. NexTech supplied us with an "LSM ink" that we can employ for cathode deposition. We used a published literature procedure for depositing the cermet anode, as NexTech maintains a proprietary interest in their anode formulation that would complicate our subsequent structural and elemental analysis. The Lindberg 54233 tube furnace that can deliver 1500 ^oC was relocated to an adjacent lab, with corresponding electrical service (220 V, 50 A) following it, allowing, Ni cermet sintering to proceed.

A Probostat$^\vee$ button cell unit was purchased and brought on-line. A grainy suspension (#6082) of Liquid Bright Platinum was purchased from Heraeus Materials Technology (formerly Engelhard) and used to prepare Pt paste (porous solid) electrodes on NexTech zirconia wafer electrolytes. An electrolytic voltage was applied to the cell and electrochemical oxygen-pumping was observed. The next step was to measure a galvanic voltage by supplying air to a strontium-doped lanthanum manganite (Sr-$LaMnO_3$, or LSM) cathode and supplying H_2 to a nickel/zirconia cermet anode.

Button cells have been fabricated, mounted into the Probostat$\vee$ test cell, and current-voltage curves obtained. Electron micrographs of Pt paste electrodes and a strontium-doped lanthanum manganite cathode are shown in Figure 2.2-1 below. Micrographs 1a and 1b clearly show the combination of large, 10+ $\propto$m grains of Pt interspersed with finely divided, porous Pt particles. The brush-applied coating made for a much more irregular but also more porous deposit. This deposit adheres to the YSZ electrolyte button much more effectively than the doctor-bladed layer.

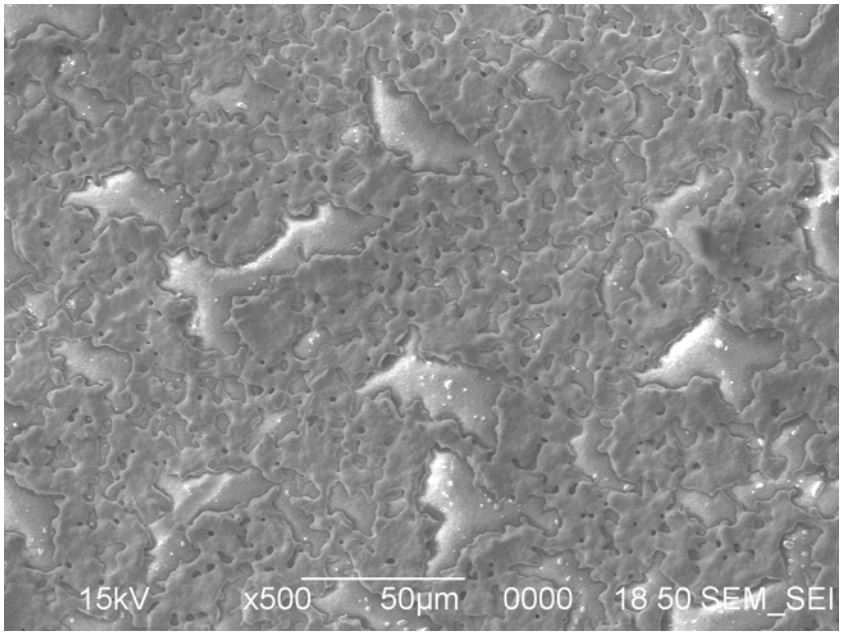

a) Doctor blade application of Pt paste electrode.

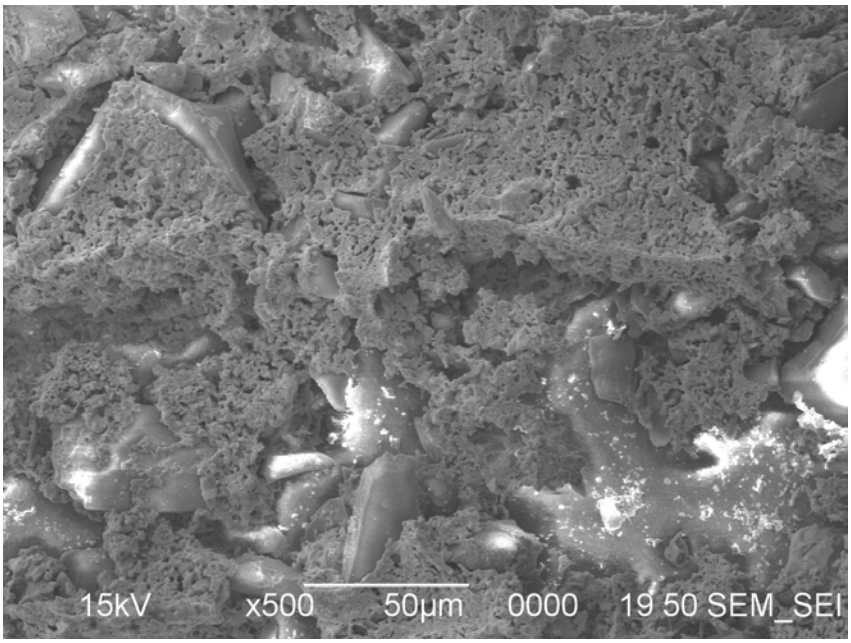

b) Brush application of Pt paste electrode.

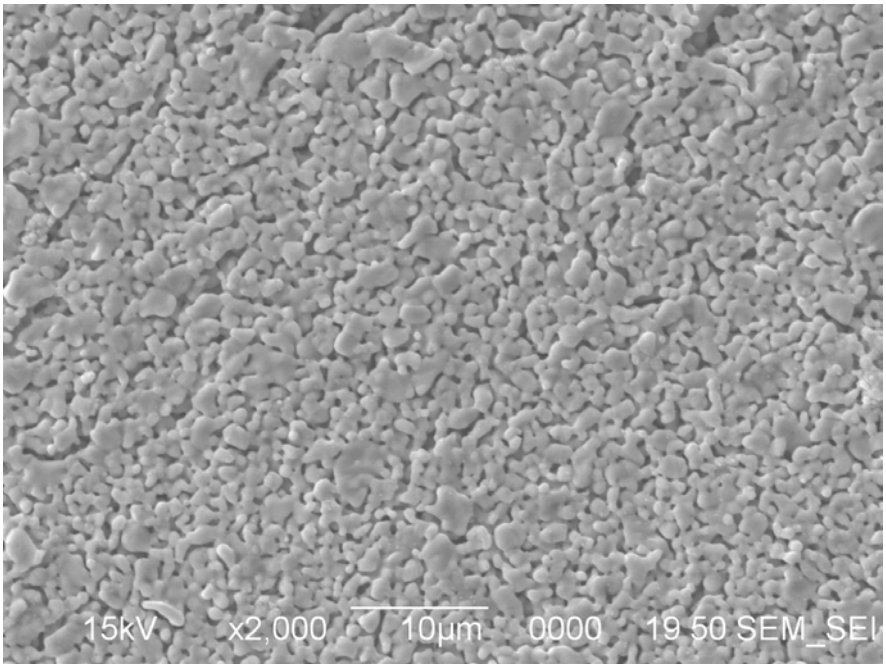

c) Sr-doped, lanthanum manganite cathode.

Figure 2.2-1. Scanning electron micrographs of SOFC electrode deposits

The cathode micrograph (2.2-1c) shows a uniformly porous array of fused, 1-3 ∝m particulates.

Nickel cermet electrodes were also prepared. Salts of yttrium, nickel, and zirconium were co-precipitated in a buffer solution, collected, and applied to YSZ to form the anode. Adhesion was once again a problem. A press was used to compress the anode onto the electrolyte, but the solid electrolyte was too delicate and cracked in the process. The cermet was successfully applied when terpineol was used to disperse the paste instead of diethanolamine. The anode was fired at 1500°C, while the cathode was fired at 1100°C. No micrographs for the cermet are shown, because the Ni is deposited in the form of a non-conducting oxide, resulting in charging distortion of the SEM image.

A current-voltage curve for a YSZ electrolyte with Pt paste anode and cathode is shown below in Figure 2.2-2. Both anode and cathode compartments are under air, so as to demonstrate electrolytic O_2-pumping. The curve consists of a straight line, indicating that ohmic resistance losses, mainly through the electrolyte, are the major sources of impedance in the device. Even so, from the slope of the curve we can calculate that the cell resistance is only 2.8 &.

Voltage	Current	Platinum electrodes Cell Resistance :2.8 ohms
0.12	0.04	
0.23	0.06	
0.33	0.08	
0.43	0.08	
0.53	0.09	
0.63	0.1	
0.73	0.11	
0.84	0.12	
0.93	0.13	

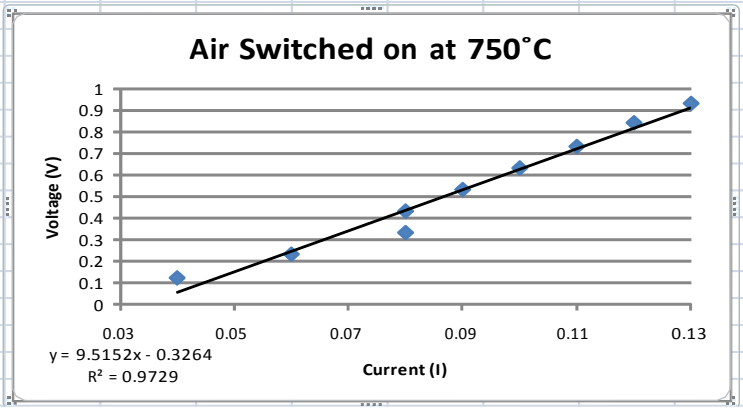

Figure 2.2-2. Current-voltage curve for O_2-pumping across electrolyte interface.

Having successfully tested oxygen transport across the YSZ electrolyte under air atmospheres in the Probostat$^{\vee}$, first with Pt anode and cathode, and then with Pt anode and lanthanum strontium manganite (LSM) cathode, it was time to supply a reducing gas to the anode and derive a galvanic voltage. The voltammetric results will be shown in the following subtask section. The remaining steps in this subtask were to fabricate Ni-YSZ cermet anodes and obtain galvanic data using H_2 as fuel gas. The cermets were formed by co-precipitating Ni, Y, and Zr salts, forming a slurry in terpineol solvent, doctor blade application onto YSZ electrolyte substrates, and firing at 1500 ^{o}C. The resulting porous dispersion is shown below in Figure 2.2-3.

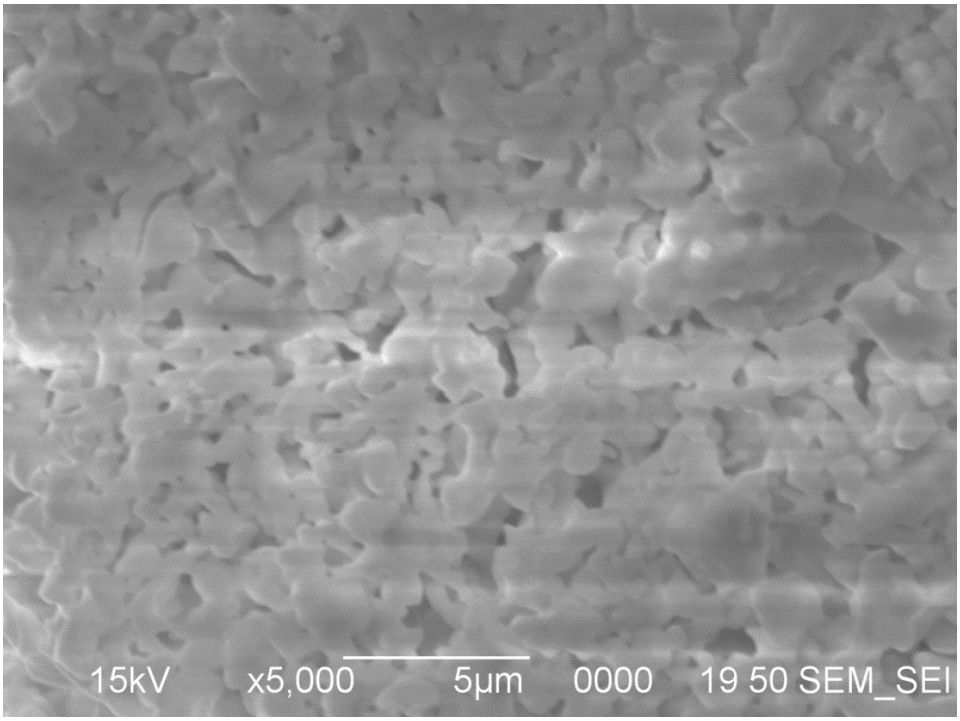

Figure 2.2-3. Scanning electron micrograph of a Ni-YSZ cermet electrode

Obtaining a gas-tight seal for the button cell electrolytes is a continuing challenge, with on order of half the finished electrode-electrolyte assemblies cracking during cell assembly and conditioning. The Hionics® brand of ZrO_2 electrolyte buttons containing Sc as dopant instead of Y were supposedly more flexible, but no improvement in the likelihood of cracking was noted. Either way, those electrolytes that do survive the sealing procedure have given galvanic open circuit voltages in the range of 0.9-1.1 V, and currents on order of a few milliamperes.

For the NextCell^{V} testing, the main issue was figuring out what to do about the lateral dimensions of the electrolyte assemblies. The NextCells are about 2 cm wider than the Crofer manifold plates that seal them. The furnace containing the fuel cell was intended to provide a close fit around the manifold plates, so that the wider NextCell scrapes against the sides of the furnace cavity. That makes it difficult to place the assembled fuel cell inside the oven without causing the thin electrolyte to crack. Having custom-fabricated electrolytes that were the same dimensions as the manifold plates was going to be quite expensive, so instead a high speed diamond blade wet saw was acquired and the extra width was trimmed off from the standard electrolyte product. The Crofer plates act as a makeshift vise to hold the electrolyte rigid while being cut.

Obtaining gas-tight seals in both Probostat and NextCell fuel cells and obtaining galvanic current-voltage data constituted completion of Subtask 2.2.

Subtask 2.3 Monitor cell performance as a function of input gas composition.

Discussions were held with NexTech as to what composition should be employed for simulated landfill gas. They were employing 30.0% CH_4, 33.3% H_2, and 36.7% CO_2, with added water

vapor on order of 1-2:1 H_2O:CH_4 content. That composition is more like gasified coal than landfill gas, as that is what they use in the SECA program. Based on literature data and our analysis of actual landfill gas, the methane should be increased to 40-45% along with CO_2, while the input H_2 should be negligible and N_2 should be 10-15%. NexTech indicated a willingness to switch to a more realistic gas composition as per our recommendation.

A flat cell consisting of Crofer manifold plates sandwiching a NextCell^{V} electrode/electrolyte assembly was assembled and inserted into a specially modified box furnace to accommodate the inlet and outlet gas tubes. Weights stacked vertically onto the manifold plates were expected to maintain segregated gas volumes at anode and cathode. Achieving the necessary gas-tight seals on the NextCell was a challenge, but slight repositioning the cell inside the furnace, and employing a machined 304 stainless steel plate to distribute the normal force to the outer edge of the cell has been successful.

Mass flow controllers for each of the input gases (CH_4, CO_2, H_2, and air) were calibrated and configured for remote control of the gases, allowing us to accurately set the flow rates and mixing ratios from a computer. The computer was also configured for remote access, allowing for future control of an SOFC on-site at a landfill from YSU campus.

Means for humidifying the anode gases were purchased and assembled. A self-regulating water reservoir was positioned over the humidification vessel so that the cell can be run for days at a time without having to expose the gas mixing head space to ambient air. Modification of the reservoir enabled its replenishment with minimal impact on the humidification process, thus enabling continuous fuel cell operation with only once per week water maintenance.

A method was developed to trim the NextCell^{V} electrode/electrolyte assemblies along the long edges to prevent chafing against the walls of the furnace, which can result in cracking. If the crack propagates into the active cell area, then fuel and oxidant gases would mix and react, reducing the efficiency of the cell and possibly generating a hot spot that could cause general cell failure. Conversations with NexTech indicated that they have no experience in such a procedure. We decided to try a Dremel tool with a circular diamond blade.

A cell was assembled without trimming the electrolyte edges, brought to temperature in the furnace (750°C) and exposed to nitrogen on the anode side and air on the cathode side. The cell was held at temperature for 24 hours. After the cell was allowed ample time to cool down, the Dremel tool was used to trim the edges of the electrolyte down to the size of the cell plates. This was performed with the NextCell still inside the Crofer manifold plates in order to prevent buckling of the thin electrolyte. The cell was then re-used under the same conditions, to determine whether a trimmed cell would work and if our alumina seals could be used more than once. After reaching temperature, we leak-tested the cell again and determined that the seal was lost and the cell was shut down for examination. The electrolyte was found to be cracked in several places, all of which appeared to have come from the edges. Since there were no visible cracks when assembling the cell, it was concluded that micro-fractures had formed while cutting the electrolyte, causing fissures to form over the entire surface area during the heating process.

Although edge-cracking remained a problem, we determined that we could assemble cells and bring them to operating conditions and pass a leak test 50% of the time. Therefore, we continued

on and tested a NextCell under variable flow rates of H_2 fed to the anode. Using a 1 k& load resistance, hydrogen was increased from 25 mL/min to 240 mL/min. The galvanic cell voltage increased monotonically from 0.949 V to 1.128 V over that range. In another experiment, H_2 flow was reduced from 70 mL/min to 0 mL/min. The voltage of the cell went from 1.024 V to 0.760 V at 5 mL/min. These results are consistent with encountering mass transport losses at lower flow rates.

A similar experiment was performed for the cathode. Hydrogen flow to the cathode was maintained at 70 mL/min while air was started at 0 mL/min and increased to 360 mL/min. No change in voltage occurred during the course of this trial. The kinetics of oxygen uptake into the electrolyte were comparatively slower than that for hydrogen, so there was no mass transport effect to overcome.

In actual practice, the biogas fuel was to be diluted and reformed with water vapor, not N_2, so the effect of varying water content on cell voltage was examined. A NextCell was tested at 20 mL/min H_2 to the anode and 20 mL/min air to the cathode. The temperature of the humidification chamber was increased from room temperature (about 23°C) to 90°C, corresponding to a water vapor partial pressure rise from 21 to 526 mm Hg. Measuring across a 100 & load resistor, there was a small drop in voltage from 0.929 V to 0.909 V. Thus, water vapor has a very modest effect on cell voltage. This experiment was repeated after shorting out the load resistor, i.e., at closed circuit. Voltage fell from 0.946 V to 0.925 V as humidity increased. Currents were on order of one ampere, so that with an active area of 28 cm^2, the current density was 35 mA/cm^2.

The primary constituent of landfill gas that has fuel value is methane. Thus we investigated the effect of methane flow rate on cell voltage. The voltage was recorded from 0 mL/min to 30 mL/min, increasing in increments of 10 mL/min, and allowing 30 minutes between steps for the system to adjust. The cell voltage was seen to increase from 0 V to 0.789 V. Despite running the methane through a water bath, some carbonization was observed.

To prevent coking of the methane, a measure of water vapor must be provided. A 50:50 water vapor content is insufficient, as shown in Figure 2.3-1 below. A black sooty cone formed at the entry port to the anode chamber. The water content should be at least 2:1, according to complete methane-reforming stoichiometry:

$$CH_4 + 2H_2O \rightarrow CO_2 + 4H_2$$

In our set-ups, the water vapor is provided by passing the feed gases through a humidification apparatus. A heated 1.0 L glass flask fitted with Ace Thread O-ring seals and greased, clamped straight union joints is used to provide a water vapor atmosphere through which the fuel gases are fed. To transfer the humidified gas to the NextCell fuel cell, while providing flexibility between humidifier and furnace, flexible FEP tubing wrapped with a heating tape has been installed. For the Probostat, copper tubing wrapped with heating tape kept well above 100 ^{0}C is employed.

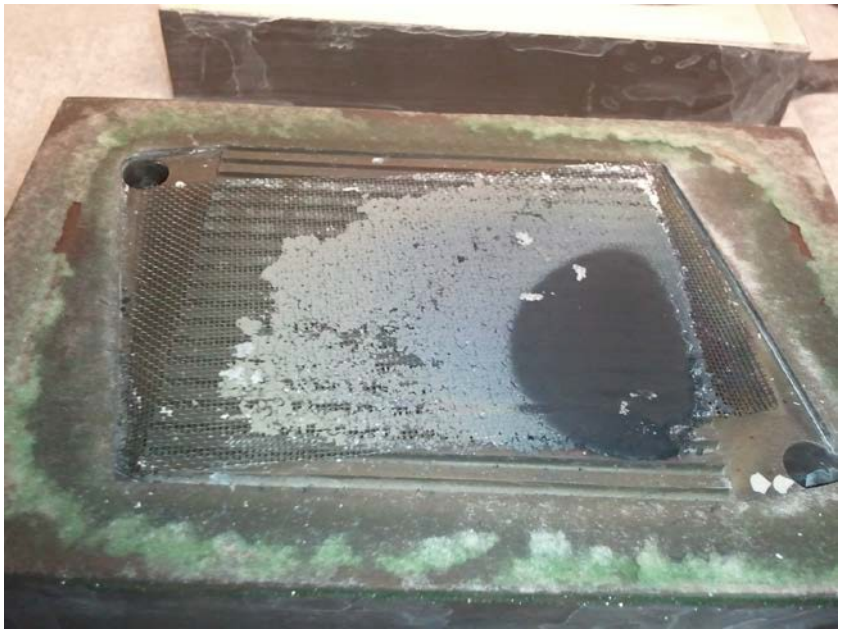

Figure 2.3-1. Soot formation under CH_4 in a NextCell due to insufficient water vapor.

The objective of this subtask is to understand the effect of varying relative concentrations of CH_4, CO_2, and H_2O vapor, and the effect of varying total flow rate, on galvanic cell performance. Those measurements were initiated by obtaining current-voltage plots using H_2 gas, as it will be formed when CH_4 and H_2O are fed in together, and it presents no risk of coking while adjusting input parameters. Button cells consisting of YSZ solid electrolyte and Pt and LSM electrodes were tested under H_2 feed to the Pt electrode and air to the LSM cathode. A manually operated load bank was varied to produce to current-voltage curve, which is shown in Figure 2.3-2. An open circuit voltage of 0.9 V was obtained, which then decayed under decreasing external load to less than 0.5 V at 50 mA. The mostly resistance-limited cell had an apparent value of 7 Ω.

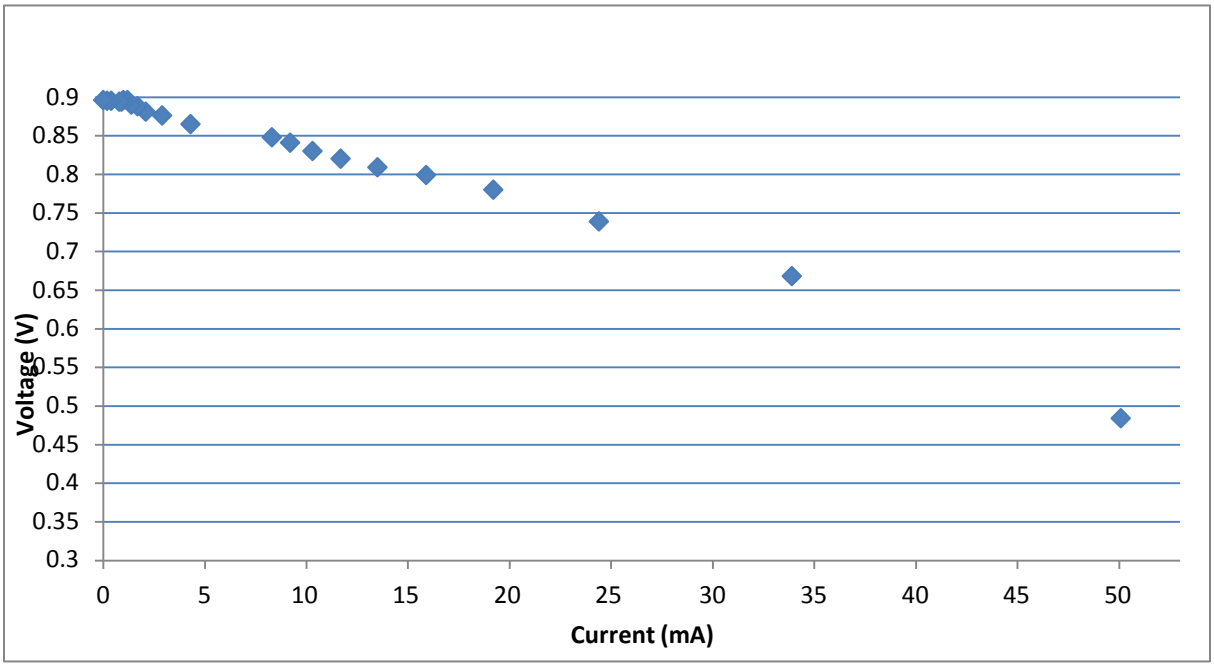

Figure 2.3-2. Current-voltage curve for Pt//YSZ//LSM galvanic button cell at 750 ^{o}C under H_2 and air at 25 mL/min.

A similar test was performed for a Ni-YSZ cermet anode and LSM cathode. The resulting current-voltage curve is shown below in Figure 2.3-3. After an initial slope of 115 Ω, there was a break in the curve at 0.6 V, followed by another linear segment with a slope of 275 Ω. The cermet is expected to be less conductive than the Pt paste electrode.

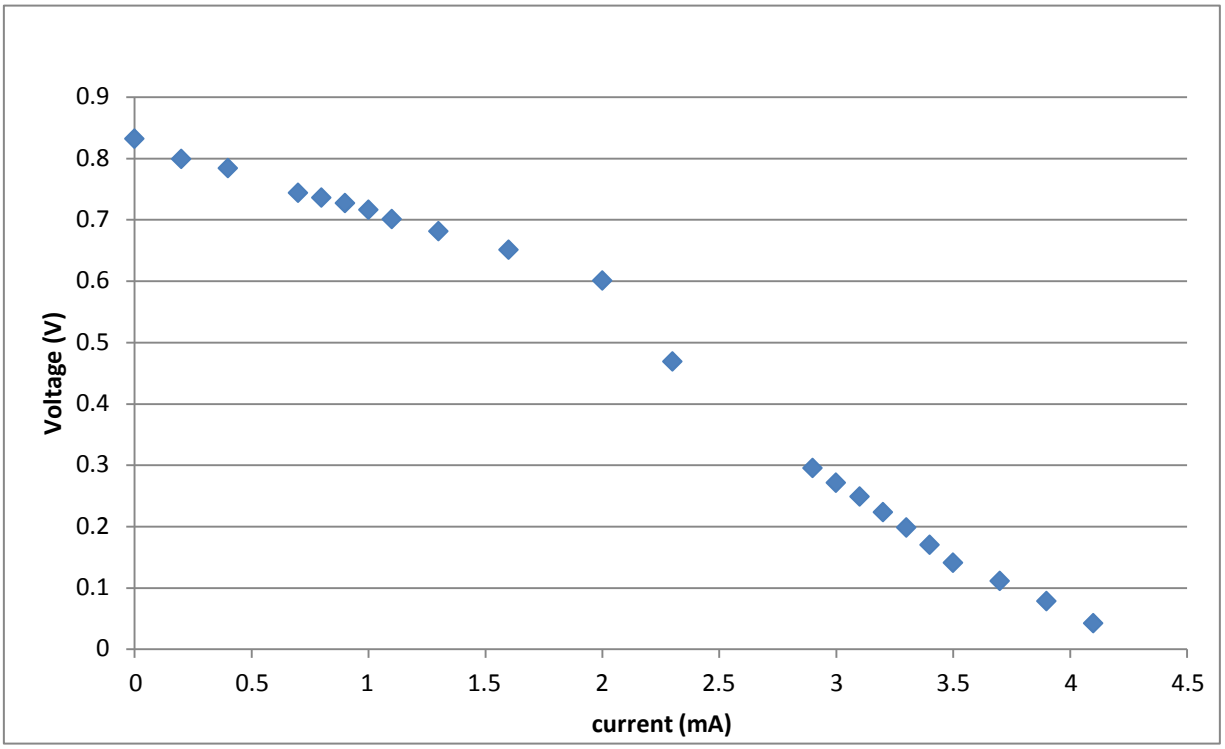

Figure 2.3-3. Current-voltage curve for Ni-YSZ cermet//YSZ//LSM galvanic button cell at 750^{o}C under H_2 and air at 25 mL/min.

Having obtained current-voltage curves using dry H_2, the next step was to observe the effect of added water vapor. This was performed using a Pt paste anode and a Ni-YSZ cermet anode. A slight drop in voltage was observed, consistent with dilution of the H_2 partial pressure by the water vapor. The next step was to mix CH_4, CO_2, and H_2O vapor and observe the effect on galvanic cell performance.

It was found that the water vapor had to be held at a significant partial pressure to avoid soot precipitation due to decomposed methane. Shown in Figure 2.3-4 below is a voltage versus time plot for a Ni-cermet//YSZ//LSM button cell exposed to 33% H_2O, 40% CH_4, and 27% CO_2 fuel gas. A steady drop in cell voltage is observed due to precipitation of carbon on the electrode:

$CH_4 \rightarrow C + 2H_2$.

To prevent soot deposition in theory, at least two equivalents of H_2O are required:

$CH_4 + 2H_2O \rightarrow CO_2 + 4H_2$

Therefore, the percent of H_2O must be at least double that of CH_4. It was thought that CO_2 might ameliorate the situation with some autothermal reforming:

$CH_4 + CO_2 \rightarrow 2CO + 2H_2$,

but under the conditions employed, it was not found to have an effect.

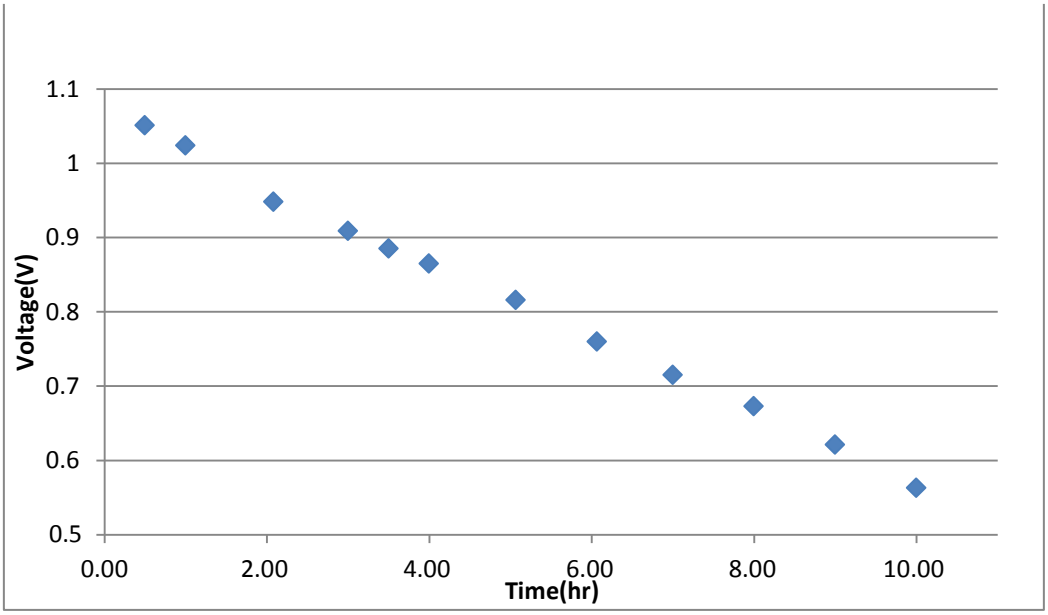

Figure 2.3-4. Decay of cell voltage versus time for a Ni-cermet//YSZ//LSM fuel cell under 33% H_2O, 40% CH_4, and 27% CO_2 fuel feed against air.

As it turned out, increasing the H_2O level to 50%, so that CH_4 content in the mixed gases was 30% and CO_2 was 20%, a 1.66 H_2O to CH_4 ratio, was sufficient to achieve a steady state. Current and voltage were nevertheless a function of external load placed across the cell, as shown in Figure 2.3-5.

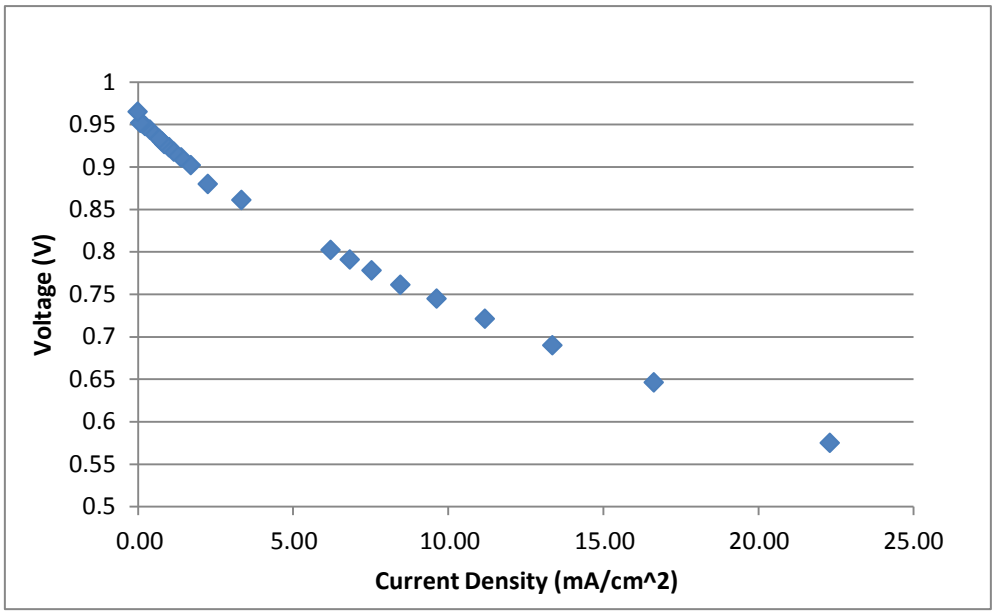

Figure 2.3-5. Graph of voltage vs current density for a Ni-cermet//YSZ//LSM fuel cell under 50% H_2O, 30% CH_4, and 20% CO_2 fuel feed against air.

A gas chromatograph with thermal conductivity detector was ordered from Gow-Mac so that gas composition could be monitored from 3 perspectives: (1) current-voltage curve; vary external load and measure I vs. V (2) corrosion/passivation of cell components; surface analysis (scanning electron and X-ray photoelectron spectroscopies); and (3) cell emissions; gas chromatographic analysis of gases exiting cell relative to input composition.

Efforts were undertaken to map out the reactions occurring with internal reforming of landfill gas and determine the best method for measuring the maximum power of the SOFC while utilizing CH_4 and CO_2 as a synthetic landfill gas. To begin, the gas chromatograph needed to be properly calibrated for each of the gases used in our experiment as well as any additional gases that were anticipated to be formed during the process. The major reactions occurring when landfill gas is reformed are as follows:

(1) Steam reforming

$CH_4(g) + H_2O(g) \rightarrow CO(g) + 3H_2$ $\quad \Delta H = 206.2$ kJ/mol

(2) Water gas shift

$CO(g) + H_2O(g) \rightarrow CO_2(g) + H_2(g)$ $\quad \Delta H = -41.1$ kJ/mol

(3) Carbon dioxide reforming

$CH_4(g) + CO_2(g) \rightarrow 2CO(g) + 2H_2(g)$ $\quad \Delta H = 247.0$ kJ/mol

(4) Methanation of carbon dioxide

$CO_2(g) + 4H_2(g) \rightarrow CH_4(g) + 2H_2O(g)$ $\quad \Delta H = -165.0$ kJ/mol

(5) Methane decomposition

$CH_4(g) \rightarrow C + 2H_2(g)$ $\quad \Delta H = 76.0$ kJ/mol

This series of reactions was found to occur simultaneously when reforming landfill gas; however depending on the conditions, the primary reactions occurring can be changed. In the system for this research the primary reaction is carbon dioxide reforming or dry reforming:

$$CH_4\,(g) + CO_2\,(g) \rightarrow 2CO\,(g) + 2H_2\,(g).$$

This is shown in the following gas chromatograms in Figures 2.3-5 and 2.3-6. The gas chromatograms show that CH_4 and CO_2 are reduced to 50% of their original composition and a significant H_2 peak is produced. If steam reforming was the dominant mechanism, the size of the CO_2 peak would have grown substantially in proportion to the amount of CH_4 exiting the fuel cell. Instead, the peaks were diminished in approximately the same proportion.

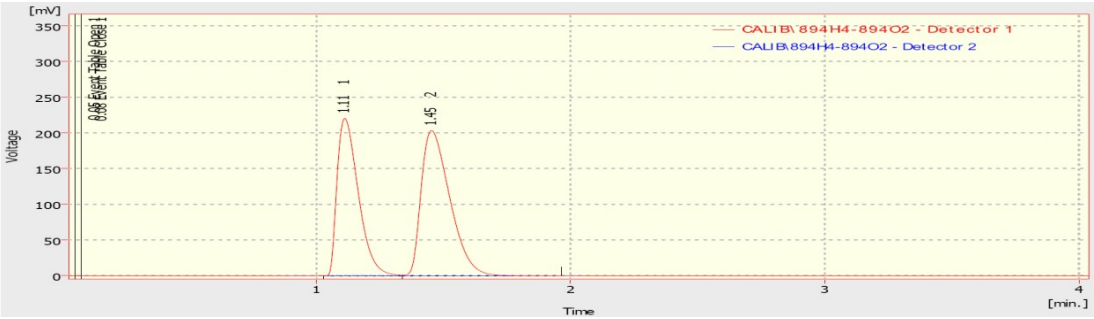

Figure 2.3-5. Gas chromatogram of dry methane and carbon dioxide before entering the fuel cell.

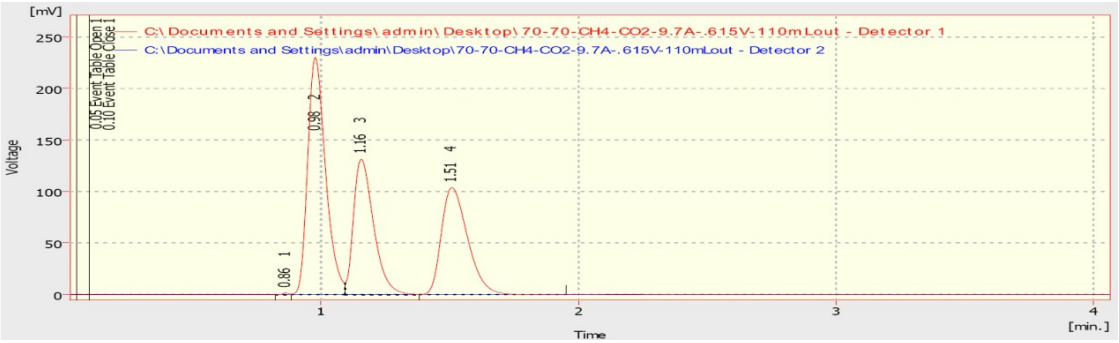

Figure 2.3-6. Gas chromatogram of fuel cell effluent after water removal. Methane and carbon dioxide are preceded by a large hydrogen peak, while their peaks are reduced in proportional amounts.

The next step was determining the maximum power point of the SOFC. Previously, an experiment to measure current vs. voltage as a function of the external resistance of the SOFC showed poorly reproducible results.

Shown below in Figure 2.3-7 is a graph of voltage and power versus current drawn from the device.

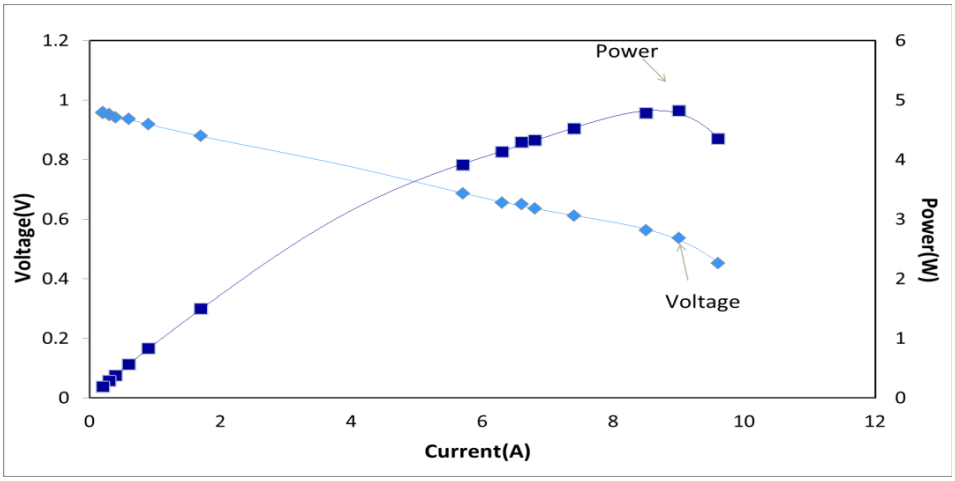

Figure 2.3-7. Current-voltage and power performance curve for an SOFC operated on 25% CH_4, 25% CO_2, and 50% water vapor.

A gas composition representative of humidified landfill gas was utilized. Note that the maximum power was 5 watts at 9 amperes for the 28 cm^2 cell. This corresponded to a load resistance of about 300 milliohms.

The change in gas composition as it passed through the fuel cell could also be monitored. A 1:1 CH_4 and CO_2 mix was humidified and supplied to the SOFC. In Figure 2.3-8, the chromatogram for the exit gases under low current operation (high load resistance) is shown. Peaks for three gases were found: from left to right, H_2, CH_4, and CO_2

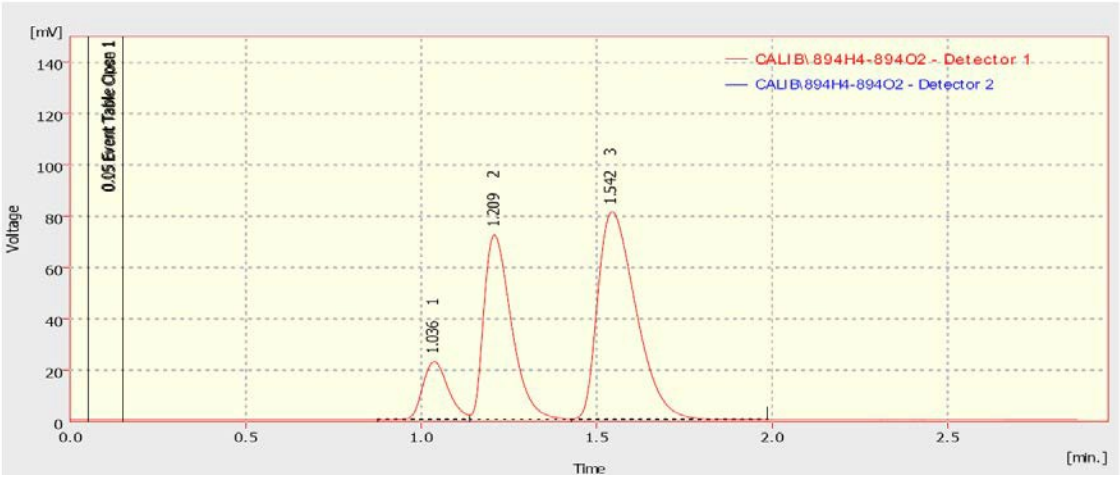

Figure 2.3-8: Cell output under 1:1:2 CH_4, CO_2, H_2O. Low current operation

The CH_4 and CO_2 were to be expected as incomplete consumption of the feed gases, but the H_2 peak apparently formed inside the cell either due to steam reforming and water gas shifting of the methane or autothermal reforming between the methane and carbon dioxide:

Steam reforming: $CH_4(g) + H_2O(g) \rightarrow CO(g) + 3H_2$

Water gas shift: $CO\,(g) + H_2O\,(g) \rightarrow CO_2\,(g) + H_2\,(g)$

Autothermal reforming: $CH_4(g) + CO_2(g) \rightarrow 2CO\,(g) + 2H_2(g)$

Under high current operation (low load resistance), the exit gas composition changed markedly. In Figure 2.3-9, the chromatogram shows that H_2 was largely missing, i.e., it is consumed in the electrochemical reaction. A new component, presumably carbon monoxide, CO, eluted at 3.29 minutes. This would imply that H_2 oxidation on the Ni/YSZ electrode/electrolyte interface proceeds more quickly than conversion of CO to CO_2.

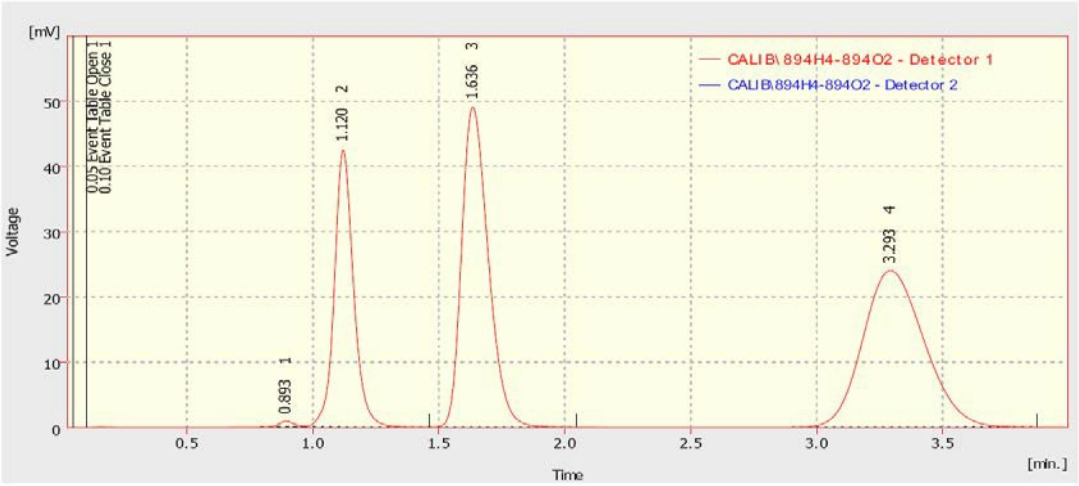

Figure 2.3-9. Cell output under 1:1:2 CH_4, CO_2, H_2O. high current operation

Additional work was conducted by NexTech Materials over the course of the project

(1) Completed the installation and commissioning of a test stand to be used for single-cell testing of large-area electrolyte-supported planar cells of NexTech's FlexCell design.

(2) Completed the stack design that will be used in this project for testing of stacks with simulated biogas as fuel. The primary modification to NexTech's existing stack design was the incorporation of catalysts into the anode chamber of the stack, to facilitate internal reforming of methane within the stack.

(3) Completed stack tests to validate important materials and components to the stack design that will be used for testing with simulated biogas fuel. These included: (a) incorporation of coatings on the cathode face of interconnects to mitigate poisoning of cathodes by chromium; (b) modification of stack sealing material and configurations; and (c) stack design changes to reduce pressure drops and improve fuel flow uniformity. Based on these modifications, considerable improvements were demonstrated in stack performance, reproducibility of performance and durability.

(4) Initiated large-area single-cell testing with the test stand that was commissioned during the previous quarter. Refined steam delivery methods required for single-cell testing with biogas based fuels.

(5) Initiated fabrication of large-area FlexCells for stack tests to be conducted with simulated biogas as fuel. Designed testing manifolds for large-area stacks, and outsourced the fabrication of these manifolds.
(6) Completed single-cell and stack tests to validate important materials and components to the stack design that will be used for testing with simulated biogas fuel. Goals of these tests included: (a) replacement of silver mesh with metal alloy meshes with appropriate corrosion-preventing coatings; development of cathode contact pastes that do not contain silver (to improve long-term stability); and (c) evaluating lower cost interconnect designs. Based on results of these tests, modifications were made to stack component designs.
(7) Continued to refine testing methodologies for large area cells, with re-design of the testing manifolds and deposition of corrosion protecting coatings.
(8) Completed the fabrication of large-area FlexCells for two different stack designs: G-13 (total area of 320 cm2 and active area of 160 cm2); and G-15 (total area of 540 cm2 and active area of 300 cm2).
(9) Completed a three-cell (G-13) stack test with various simulated biogas fuel compositions:
    1. With simulated sulfur-free pre-reformed biogas (23% CH_4, 33% H_2, 9% CO, 13% CO_2, and 22% H_2O) as fuel, the stack achieved a total power of 141 watts at 70 percent fuel utilization.
    2. With simulated sulfur-free raw biogas plus steam (40% CH_4, 20% CO_2, and 40% H_2O) as fuel, the stack achieved a total power of 141 watts at 70 percent fuel utilization.
    3. With simulated sulfur-free raw biogas (50% CH_4 and 50% CO_2) as fuel, the stack achieved a total power of 129 watts at 70 percent fuel utilization.
    4. Determined from the above tests that complete conversion of methane was not being achieved.
(10) Improved the methods for applying catalyst coatings to nickel-foam anode current collectors, which should lead to improved methane conversion in future stack tests.

Subtask 2.4 Evaluation of Gas Clean-up

Equipped with cylinders of CH_4, CO_2, and H_2, each with its own mass flow controller, a humidification vessel, and a cylinder of CH_4 deliberately tainted with 100 ppm of H_2S, monitored with its own floating ball flowmeter, we were able to adjust the five gases to various proportions and generate a family of current-voltage curves for Ni-cermet anode and LSM cathode.

The effect of added H_2S was quite pronounced. Adding just 5 ppm of H_2S to the fuel gas caused an approximate 80% drop in steady state current, as shown below in Figure 2.4-1.

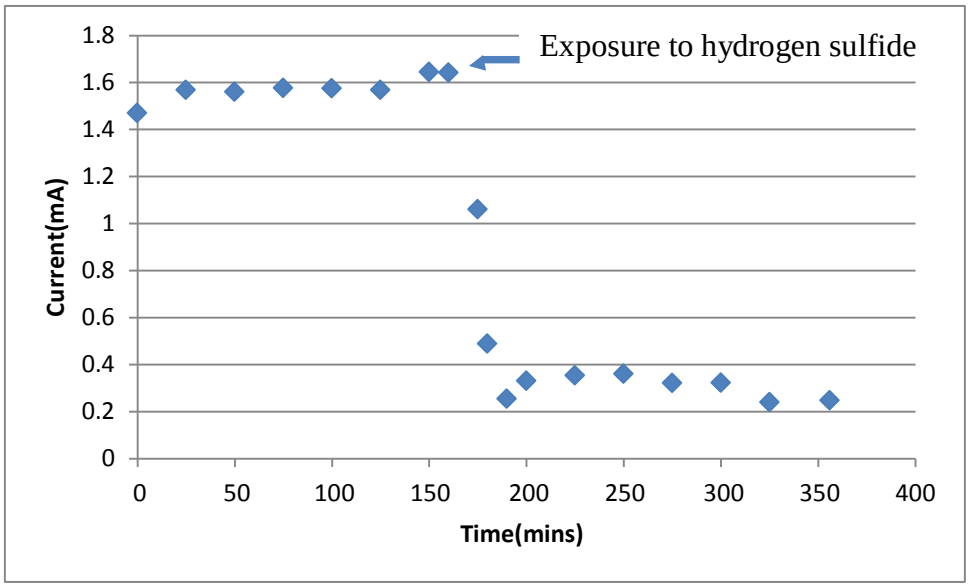

Figure 2.4-1. The effect of 5 ppm hydrogen sulfide on current over time for a Ni-cermet//YSZ//LSM fuel cell under 50% H_2O, 30% CH_4, and 20% CO_2 fuel feed against air

Two important aspects of the sulfur passivation were observed pertaining to reversibility, however. It was determined that the sulfur passivation effect could be reversed if the H_2S supply was halted, as shown in Figure 2.4-2. After reducing cell current due to H_2S exposure, the supply of sour gas was stopped. Cell current immediately began to recover, and over the course of the next 24 hours returned to within 80% of its initial value. This would indicate a type of equilibrium where the sulfur is returned to the gas phase, and the Ni-cermet surface returned to its original state. The supposed equilibrium would be

$$H_2S \rightleftharpoons S(ads) + H_2$$

The equation would imply that the presence of H_2 would aid in the removal of adsorbed sulfur from the electrode surface. This was examined by once again exposing a cell to H_2S, but this time including a background of H_2 in the fuel mixture. In Figure 2.4-3, it is shown that a 32% H_2 background reduces the equilibrium passivation effect of 5 ppm H_2S to only a couple percent of the initial current. The H_2 content could be reduced to nearly 10% without substantial current decay.

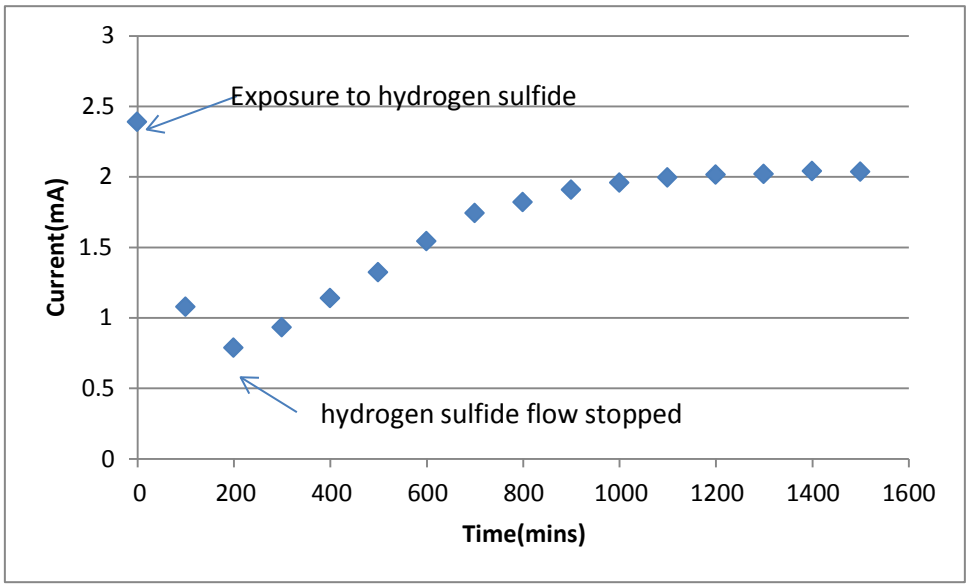

Figure 2.4-2. Reversibility of hydrogen sulfide effect on a Ni-cermet//YSZ//LSM fuel cell under 50% H_2O, 30% CH_4, and 20% CO_2 fuel feed with/without 5 ppm H_2S against air.

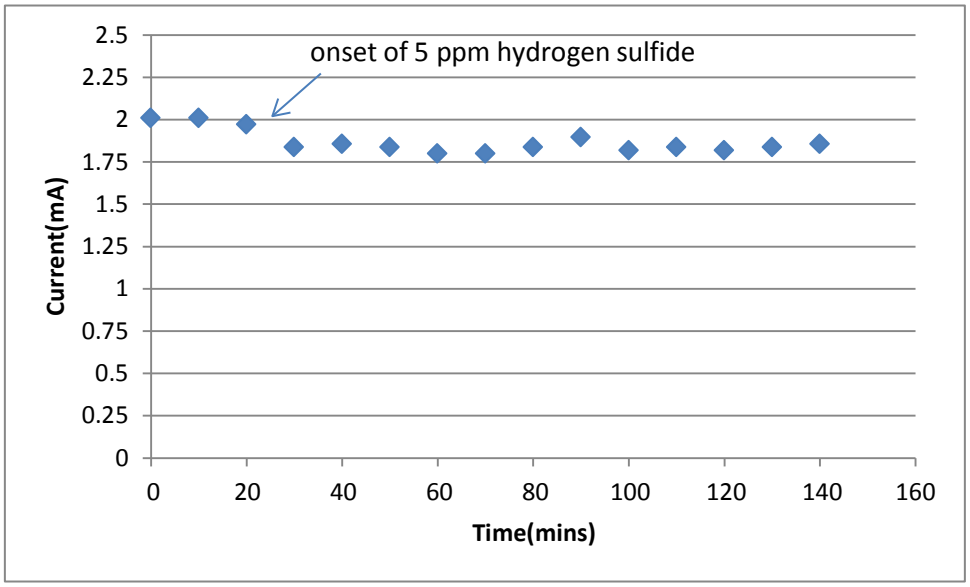

Figure 2.4-3. Effect of hydrogen background (32%) on hydrogen sulfide passivation (5 ppm) of the Ni-YSZ anode. Balance of gases: 50% H_2O, 11% CH_4, 7% CO_2.

Our efforts concentrated on the removal of hydrogen sulfide. We evaluated metal sulfides as adsorbents in the removal of H_2S. Sulfides tested include AgS, Cu(II)S, MoS_2, and WS_2. We also tested the efficiency of TiO_2-coated activated carbon for H_2S adsorption and also worked on regeneration of the adsorbent. Later on we switched to CdS to test its adsorbing capability towards H_2S and also to test its H_2 producing capability during regeneration. For the regeneration process, a Xe-arc lamp (1000 W) was used as a light source. We first platinized CdS via

photocatalytic reduction of chloroplatinic acid, H_2PtCl_6. Then we tested its photoactivity using different solutions. Scrubbed and adsorbed H_2S was simulated with a combination of sodium sulfide (0.24 M) and sodium sulfite (0.35 M). Sulfite ion was included to prevent formation of visible light-absorbing polysulfides (S_n^{2-}). Gas volume was measured by taking readings of water displaced in an inverted graduated cylinder.

It was observed rather serendipitously that the presence of a highly hydrophobic surface such as perfluorinated Teflon® enabled a higher rate of photocatalysis by the Pt-CdS adsorbent. This was observed initially as effervescence from a Teflon stir bar accidentally left in a test tube containing Pt-CdS under photolysis. Teflon strips cut from a sheet and deliberately added to a Pt-CdS dispersion gave the same effect. Results obtained in our experiments along with controls are tabulated in Table 2.4a below.

Table 2.4a. Gas volumes obtained via photolysis of Pt-CdS dispersed in aqueous solutions. Solution was 1.0 g Pt-CdS dispersed in 50 ml of water containing 0.24 M Na_2S and 0.35 M Na_2SO_3; 1000 W Xe-arc lamp.

Contents in test tube	Time exposed in hours	Gas evolved in ml
water + Teflon strip	2	3.5
S^{2-}/SO_3^{2-} + Teflon strip	2	2.5
Pt-CdS + Teflon strip+S^{2-}/SO_3^{2-}	2	17
Pt-CdS+ S^{2-}/SO_3^{2-}	2	14
Pt-CdS + water + Teflon strip	2	11
Pt-CdS+ S^{2-}/SO_3^{2-}+Teflon stir bar	2	21
Pt-CdS+water+ Teflon stir bar	2	10.5
water + Teflon stir bar	2	3
S^{2-}/SO_3^{2-}+Teflon stir bar	2	2.5
S^{2-}/SO_3^{2-} only	2	2.5
Water only	2	3

All samples showed at least some gas evolution, regardless of contents. The 2.5-3.5 ml volumes likely represent thermal expansion effects, i.e., irradiation of the test tube with the high intensity Xe lamp caused heating of the solution and expansion of the gas in the head space into the measuring column. The higher volumes represent real gas generation that was confirmed to be H_2 with the use of a quadrupole mass spectrometer. Evolution of H_2 is taken to represent removal of H_2S via

$$H_2S(g) + H_2O \rightarrow H^+(aq) + HS^-(aq)$$

$$HS^-(aq) + \text{light, CdS} \rightarrow S^o(s) + H^+(aq) + 2e^-$$

$$2H^+(aq) + 2e^- \rightarrow H_2(g)$$

net: $H_2S + (\text{water + light + CdS}) \rightarrow H_2(g) + S^o(s)$.

The highest volumes were obtained with the Teflon, sulfide solution, and photocatalyst combinations. A fair amount of gas was collected even in the absence of sulfide ion. In those cases, the electron equivalents required to evolve H_2 may have come via photoanodic corrosion of the CdS photocatalyst:

$$CdS + light \rightarrow Cd^{2+}(aq) + S^{o}(s) + 2e^{-}.$$

This situation is certainly to be avoided, hence the earlier emphasis on concentrating sulfide ion via adsorption. Detection of Cd^{2+} in the test solution plus other methods of intermingling the photocatalyst and a perfluorinated support are in progress.

Relative photocatalytic activity as measured by H_2 gas evolution is shown below in Table 2.4b. It is thought that reduction of water to evolve H_2 is the electron acceptor system to accompany sulfide oxidation, and so is a marker for photocatalytic activity.

Table 2.4b. Gas evolution from various CdS photocatalyst systems. Solution was 1.0 g of photocatalytst dispersed in 50 ml of water containing 0.24 M Na_2S and 0.35 M Na_2SO_3; 1000 W Xe-arc lamp.

Contents in test-tube	Time exposed in hours	Gas evolved in ml
water+teflon strip	2	3.5
S2-/SO32-+teflon strip	2	2.5
Pt-CdS+teflon strip+S2-/SO32-	2	17
Pt-CdS+S2-/SO32-	2	14
Pt-Cds+water+teflon strip	2	11
Pt-Cds+S2-/SO32-+teflon stir bar	2	21
Pt-CdS+water+ teflon stirbar	2	10.5
Pt-Cds+water	2	10
water+teflon stirbar	2	3
S2-/SO32-+teflon stir bar	2	2.5
S2-/SO32- only	2	2.5
Water only	2	3
CdS + water	2	3
CdS + S2-/SO32-	2	3
CdS + S2-/SO32- + teflon strip	2	6
CdS + S2-/SO32- + teflon stirbar	2	12
CdS + water + teflon strip	2	10
CdS + water + teflon stirbar	2	12
CdS+ sulphur + teflon(partition exp)	2	10

Initial work concentrated on various formulations based on cadmium sulfide, CdS and expanded to other metal sulfides: CuS, MoS_2, WS_2, and Ag_2S. Relative photocatalytic activity as measured by H_2 gas evolution is shown below in Tables 2.4c-f. Some CdS data is included in Table 2.4c for comparison.

CuS showsreasonable activity for H_2 evolution, but recurrent production of a blue solution was a sign of photooxidation of CuS to $CuSO_4$. In other words, photocorrosion was occurring. The other sulfides appeared to be stable.

Table 2.4c. Gas evolution from various CdS and CuS photocatalyst systems. Solution was 1.8 g of photocatalytst dispersed in 50 ml of water containing 0.24 M Na_2S and 0.35 M Na_2SO_3; 1000 W Xe-arc lamp.

Photocatalyst system	Time of Experiment (h)	Gas evolved (ml)
Pt-CuS water+teflon strip	2	8
Pt-CuS+S^{2-}/SO_3^{2-}+Teflon strip	2	7
Pt-CuS water+teflon stir bar	2	6
Pt-CuS+S^{2-}/SO_3^{2-}+ Teflon stir bar	2	16
Pt-CuS+water	2	8
Pt-CuS+S^{2-}/SO_3^{2-}	2	10
CdS+water	2	15
CuS+S^{2-}/SO_3^{2-}	2	9
CuS water+teflon strip	2	10
CuS+S^{2-}/SO_3^{2-}+Teflon strip	2	5
CuS+water+Teflon stir bar	2	11
CuS+S^{2-}/SO_3^{2-}+Teflon stir bar	2	8

Table 2.4d. Gas evolution experiment using MoS_2

Photocatalyst system	Time of Experiment (h)	Gas evolved (ml)
MoS_2 + water	2	14
Pt-MoS_2 +water	2	12
MoS_2 + S^{2-}/SO_3^{2-}	2	5
Pt-MoS_2 +S^{2-}/SO_3^{2-}	2	11
MoS_2 + water +Teflon strip	2	14
Pt-MoS_2 +water+ Teflon strip	2	13
MoS_2 + S^{2-}/SO_3^{2-} + Teflon strip	2	9
Pt-MoS_2 +S^{2-}/SO_3^{2-}+ Teflon strip	2	12

Table 2.4e. Gas evolution experiment using WS_2

Photocatalyst system	Time of Experiment (h)	Gas evolved (ml)
WS_2 + water	2	9
Pt-WS_2 +water	2	10
WS_2 + S^{2-}/SO_3^{2-}	2	9
Pt-WS_2 +S^{2-}/SO_3^{2-}	2	12
WS_2 + water + Teflon strip	2	7
Pt-WS_2 +water+Teflon strip	2	12
WS_2+ S^{2-}/SO_3^{2-} + Teflon strip	2	8
Pt-WS_2 +S^{2-}/SO_3^{2-}+ Teflon strip	2	14

Table 2.4e. Gas evolution experiment using Ag_2S

Photocatalyst system	Time of Experiment (h)	Gas evolved (ml)
Ag_2S + water	2	8
Pt- Ag_2S +water	2	13
Ag_2S + S^{2-}/SO_3^{2-}	2	7
Pt- Ag_2S +S^{2-}/SO_3^{2-}	2	12
Ag_2S + water + Teflon strip	2	11
Pt- Ag_2S +water+Teflon strip	2	12
Ag_2S + S^{2-}/SO_3^{2-} + Teflon strip	2	14
Pt- Ag_2S +S^{2-}/SO_3^{2-}+ Teflon strip	2	15

Based on these results, we a shifted the platinization method from photoreduction to chemical reduction using sodium borohydride, $NaBH_4$. CdS was platinized using 0.05 M $NaBH_4$, 1 g of CdS, and 0.673 g of chloroplatinic acid. The solution was filtered and the gas evolution experiment was carried on with the platinized CdS powder. A record 23 ml of gas evolution was observed with 1 g of adsorbent in 2 h using sulfide/sulfite solution.

To further check the effect of Teflon powder in the experiments, pellets of platinized CdS and fine Teflon powder were prepared and tested for gas evolution. The pellets contained 70% platinized CdS and 30% Teflon powder. A 15 ml volume of gas was evolved in 2 h under the same experimental conditions as in the tables above. A picture showing H_2 bubbles forming on the surface of the CdS/Teflon pellets is shown in Figure 2.4-4 below.

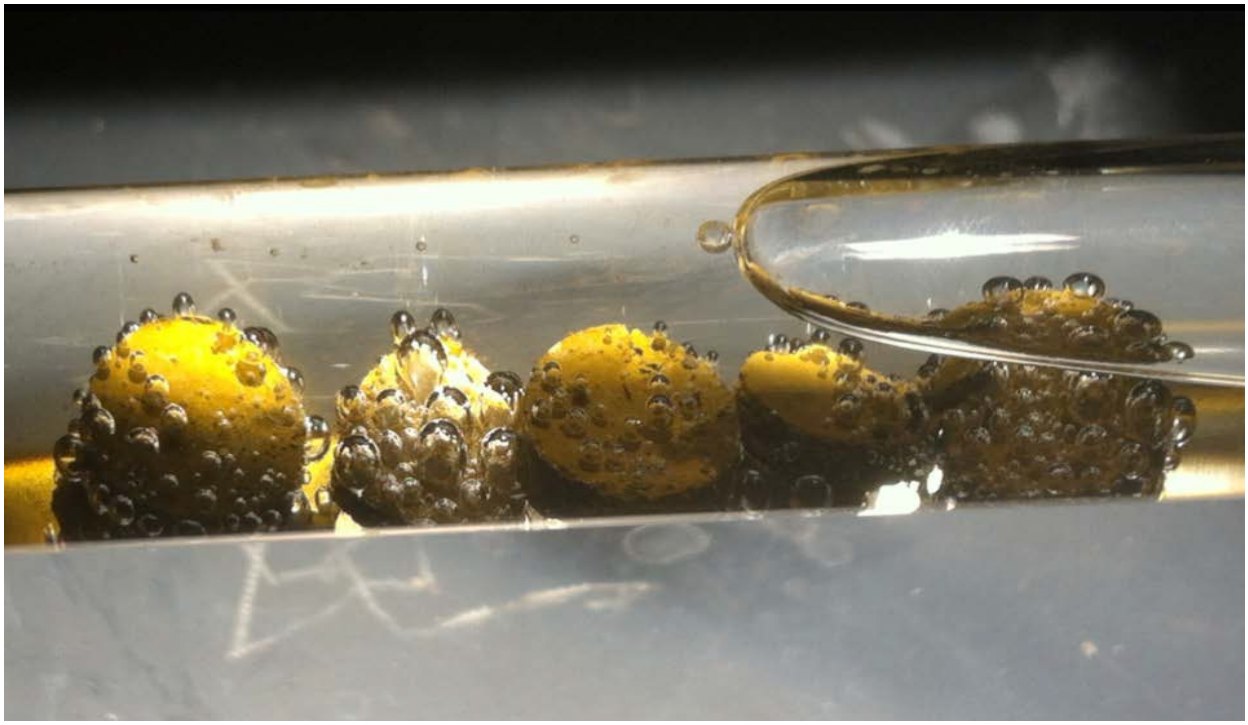

Figure 2.4-4. Evolution of hydrogen bubbles from the Pt-CdS/Teflon pellets under illumination.

After testing various sulfides like CdS, CuS, MoS_2, WS_2 and Ag_2S, we started testing the stability of these sulfides with a gravimetric analysis. In gravimetric analysis we measured the weight of the sample before and after experiment. Any weight lost by the semiconductor would likely be because of photo-corrosion. For example, we observed weight loss of about 0.0018 g in case of CdS. As the weight difference is very little, accurate readings were somewhat difficult, so we visited the ICP-OES (Inductive Coupled Plasma- Optical Emission Spectrometry) facility to analyze our samples. In a typical ICP-OES experiment, a solution containing unknown or unquantified compounds is nebulized into the plasma torch and heated to thousands of degrees Celsius. The thermal conditions break down the compounds into their constituent atoms. Some of the atoms are thermally energized into an electronic excited state. Light emission that occurs as the atoms cool is measured and used to identify which elements are present. Each of the filtrates from the photo experiments was analyzed for the presence of the respective metal ions. The following results were observed:

1. Silver sulfide:

   analysis wavelength : 328.068

   measured Ag^+ concentration : 0.8149 ppm

2. Cadmium sulfide:

   analysis wavelength : 226.502

   measured Cd^{2+} concentration : 0.0852 ppm

3. Tungsten sulfide:

   analysis wavelength : 209.860

   measured WO_4^{2-} concentration : 342.2 ppm (based on W)

4. Molybdenum sulfide:

   analysis wavelength : 204.598

   measured MoO_4^{2-} concentration : 2.567 ppm (based on Mo)

From the above results, it is evident that all of the photocatalysts are prone to photo-corrosion, but based on the concentrations from the results, tungsten sulfide seems to be more prone for photo-corrosion when compared to the other semiconductor adsorbents.

We also tested the role of Teflon in promoting H_2 bubble formation in the photo experiments by performing various tests. Hydrogen was bubbled vigorously into a test tube containing an abraded (mechanically roughened) Teflon strip along with varying solution constituents for 10 min. Afterwards, the strip would be inspected in-situ for bubble formation. Results are summarized in Table 2.4g below:

Table 2.4g. Qualitative observations on H_2 bubble formation

S.No	Contents in the test tube	Results
1	pH12 NaOH	Small bubbles were observed on the surface of abraded Teflon strip
2	Pt-CdS in water	Large bubbles were observed on the surface of the abraded Teflon strip
3	Water	Small bubbles were observed on the surface of the abraded Teflon strip
4	Pt-CdS in pH 12 NaOH	Small bubbles were observed on the surface of the abraded Teflon strip
5	Teflon + CdS + water	Minute bubbles rising up in solution and on abraded Teflon strip
6	Water + Pt-CdS + sand paper	Very small bubbles on the surface of abraded Teflon strip
7	Pt-CdS + SO_3^{2-}/HS^-	Medium sized bubbles all over the surface of abraded Teflon strip

It appears that platinized CdS in conjunction with non-alkaline pH is necessary to support facile H_2 bubble formation.

A related strategy is to split the adsorbing and photo-oxidative capabilities, and intimately mix two materials, one of which is a good adsorbent and the other a good photocatalyst. For an adsorbent we have been investigating activated carbon and other high surface area carbons for their ability to remove H_2S. To measure adsorption capacity, 100 mg of carbon was weighed out and added to 50 ml of water. A 0.1 M Na_2S solution was added dropwise to the carbon suspension. Adsorption was monitored via changes in pH and ion-selective electrode (ISE) potential measurements. When sulfide is adsorbed onto the carbon, the free sulfide concentration drops and is measured as a change in electropotential by the ISE. Lower sulfide levels in solution result in a more positive electropotential.

Theoretically 91 ml of sulfide solution should saturate the available carbon, but according to the ISE, the adsorption reaction continued even past 110 ml of 0.1 M Na_2S. The only way we could understand these results was to postulate conversion of the sulfide into nondetectable products. Therefore, we tested the filtrate for oxidation products.

To perform IR and UV-VIS spectra, standard solutions of sulfate and thiosulfate were prepared and the spectra compared to the filtrate from the experiment.

Table 2.4h. Infrared absorption peaks of oxidized sulfur compounds.

Wave number cm^{-1}	**Compound**
1107	Sodium sulfate
1118	Thiosulfate

1. IR of sulfides:
   From the IR results we found that the filtrate contains thiosulfate and sodium sulfate from the peaks.

2. UV-VIS spectra of sulfides:
   Filtrate was tested for oxidation products. UV-Visible spectra were recorded for the filtrate. From the wavelength position of the absorption peaks, presence of oxidation products was evident.

After obtaining the spectra of the filtrate, chemical tests were performed.

1. Thiosulfate test: Iodine was added dropwise into a beaker containing the filtrate solution. Decoloration of iodine was observed, which indicated possible presence of thiosulfate.

2. Iodometry: 5 ml of acetic acid was added to 10 ml of 0.025 N iodine solution. 100 ml of the test solution was added dropwise to this solution. To this 0.025 N sodium thiosulfate was added until the color of iodine was nearly gone. 5 ml of starch solution was added and again back titrated with sodium thiosulfate until completion. From the results we determined that there was sulfite present in the solution.

From the tests above it was evident that the sodium sulfide solution is being oxidized. This may be due to air leakage into the test vessel while measuring adsorption. A special cell is being built that will provide gas-tight seals for all the test probes.

Several forms of carbon, especially Vulcan XC-72 and activated carbon, were found to have exceptional sulfide uptake. Moreover, the carbons were so adept at removing sulfide from solution that the methodology had to be questioned, as the number of moles of sulfide adsorbed over a period of days exceeded the number of moles of carbon in the adsorbent! Qualitative testing revealed that sulfide was being oxidized beyond the elemental state to sulfate and thiosulfate. It was suspected that over the prolonged titration test (several days) air was leaking into the vessel and oxidizing the sulfide, with the carbon adsorbent acting as catalyst.

To confirm the effect of carbon and determine its true adsorption affinity for sulfide, a special 4-neck 300ml round bottomed flask was custom built for this experiment. Each neck had either an Ace-Thred O-ring seal or a ground glass joint with plastic joint clamps to obtain a gas-tight seal. The necks were used to hold a sulfide ion-selective electrode (ISE), a pH electrode, a gas inlet and a graduated addition funnel with double stopcocks. A 50 ml quantity of water was placed in the round bottomed flask and 1.0 g of adsorbent was added to it. Sulfide solution was placed in the addition funnel. The system was purged with Ar gas to remove background air. With the pH and ISE being monitored continuously, 5 ml of 1.0×10^{-2} M Na_2S was added to the system from the addition funnel and pH and ISE readings were recorded. After a lengthy time interval (about 12 h) pH and ISE readings were recorded again and another 5 ml of 1.0×10^{-2} M Na_2S solution was added. This was repeated again until there was no change in ISE reading. The ISE potential rose only a few mV, indicating modest sulfide adsorption. Deliberate admission of air caused a steady rise in ISE potential covering several hundred mV. Thus air was oxidizing the sulfide under catalytic action of the carbon. The landfill at New Springfield gives off gas that is 1% in O_2, which represents a large excess in comparison to H_2S, so possibly carbon could play a role in sulfide autoxidation.

Effect of Teflon:

During photo experiments we observed bubbles rising from the surface of a stirbar that was in contact with the platinized photocatalyst, as shown in Figure 2.4-4

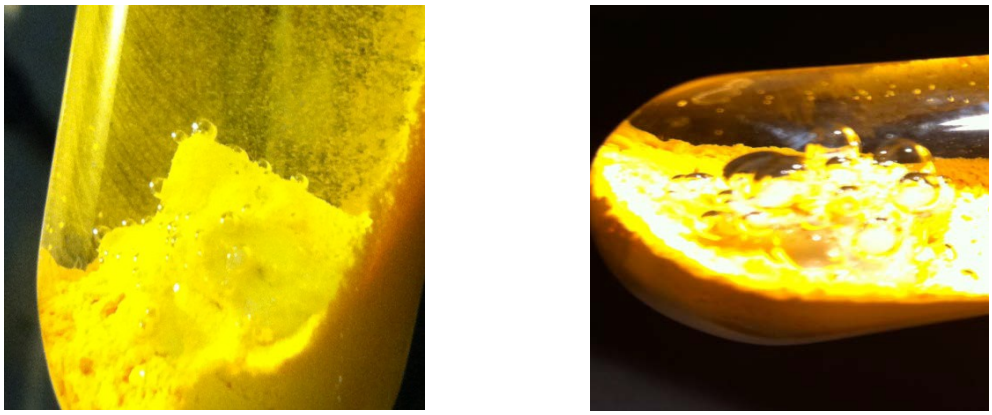

(a) (b)

Figure 2.4-4. Bubbles rising from Teflon stir bar

There was increased gas (hydrogen gas) volume when there was Teflon in the system as compared to platinized photocatalyst alone. Different treatments of Teflon such as Teflon sheet cut into strips, abraded Teflon strips and Teflon powder were tested to see the effect.
With a Teflon strip in the system there are bubbles on the surface of the strip as long as it is in contact with the platinized photocatalyst, as shown in Figure 2.4-5.

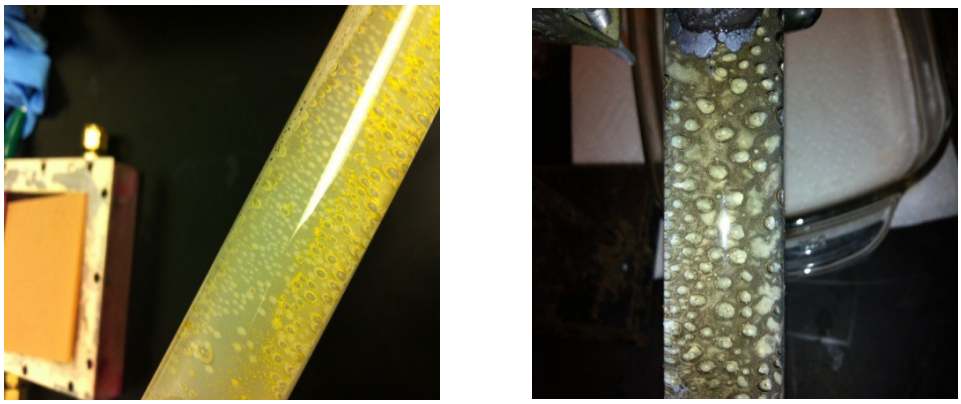

(a) **(b)**

Figure 2.4-5. Bubbles of hydrogen gas on Teflon strip.

With an abraded Teflon strip, even more gas bubbles were formed on the surface, as shown in Figure 2.4-6.

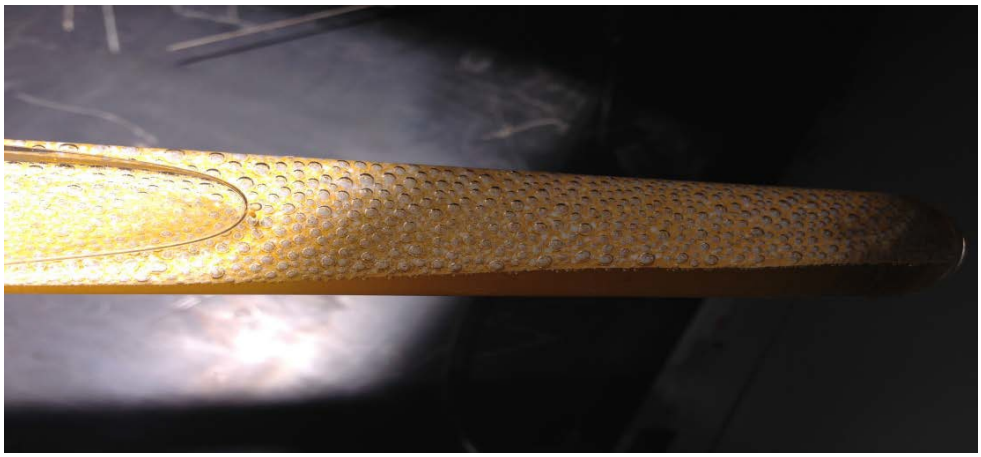

Figure 2.4-6. Bubbles of hydrogen gas on abraded Teflon strip

The perfluorinated Teflon is of course highly hydrophobic, so that in powdered form it floated on the surface during photo experiments, avoiding contact with the platinized photocatalyst. To avoid this issue, platinized photocatalyst (70% by weight) and Teflon powder (30% by weight) were pressed into a pellet and added to the system. More gas evolution was observed from this system, if for no other reason than considerably more photocatalyst was employed.

The surfaces of different types of Teflon treatments were analyzed through electron microscopy. The samples were sputter-coated with a thin Au layer to prevent charging effects. Images of Teflon sheeting, abraded Teflon sheeting and Teflon powder are shown in Figures 2.4-7, respectively.

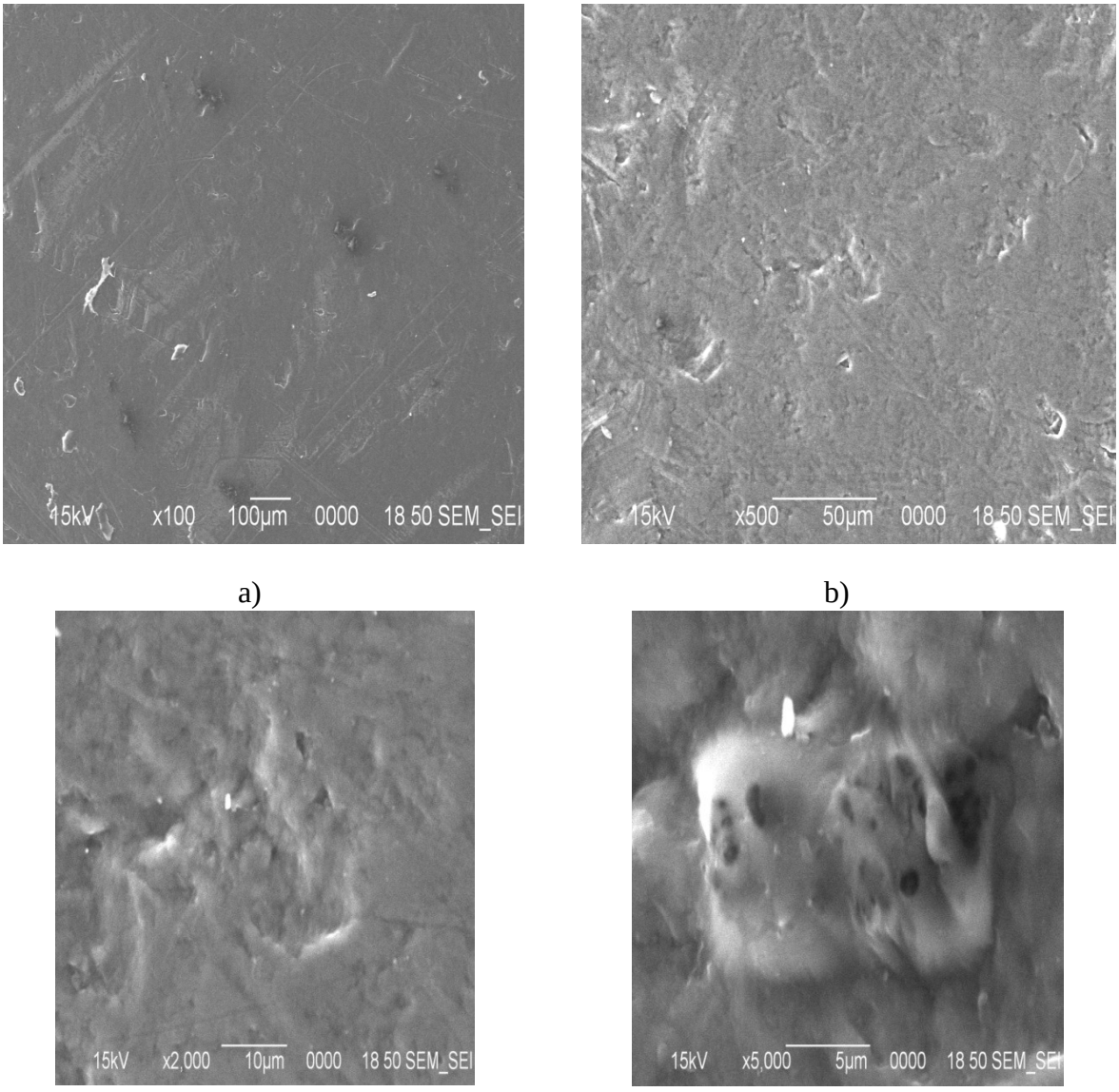

Figure 2.4-7. SEM images of Teflon sheet.

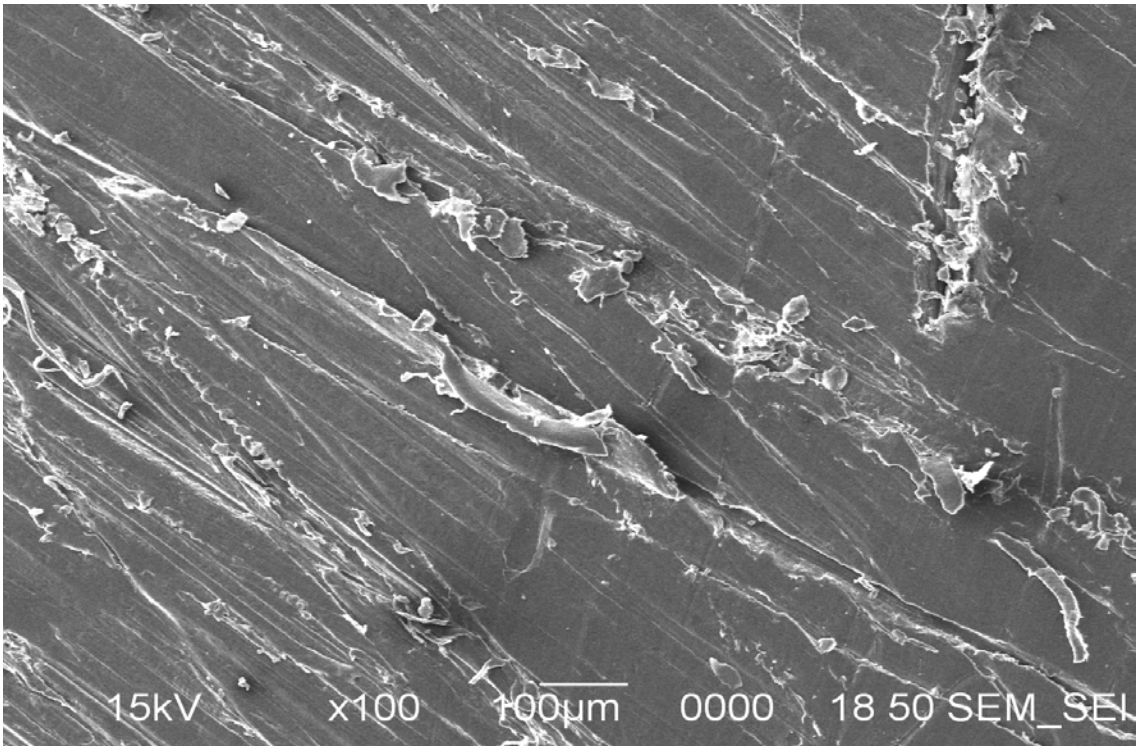

(a)

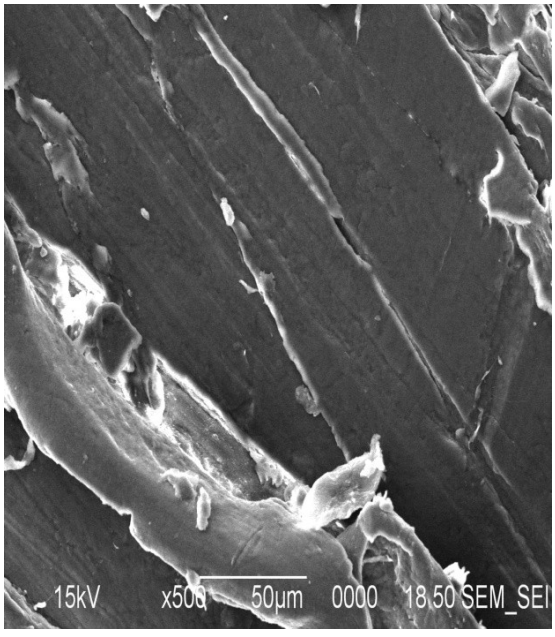

(b)

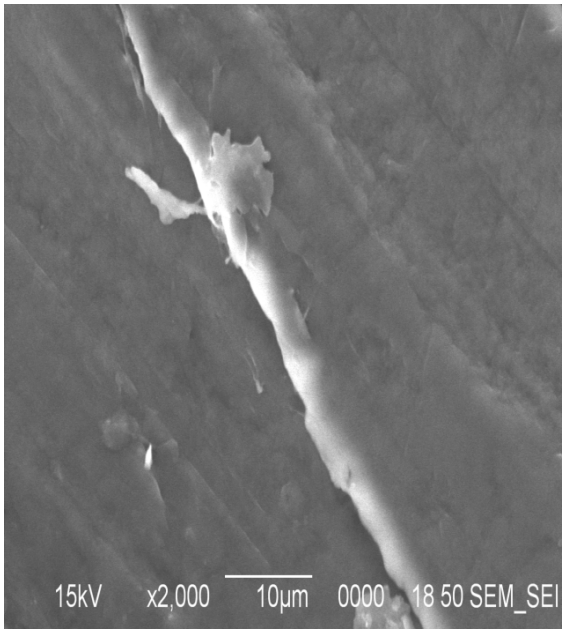

(c)

Figure 2.4-8. SEM images of abraded Teflon sheet.

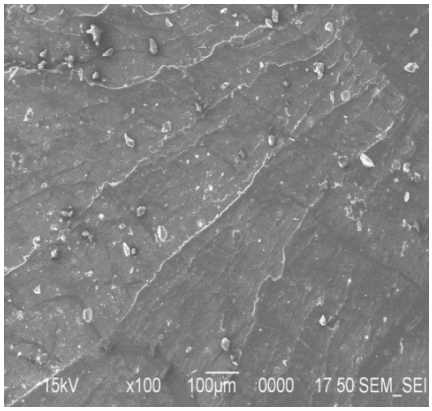

(a)

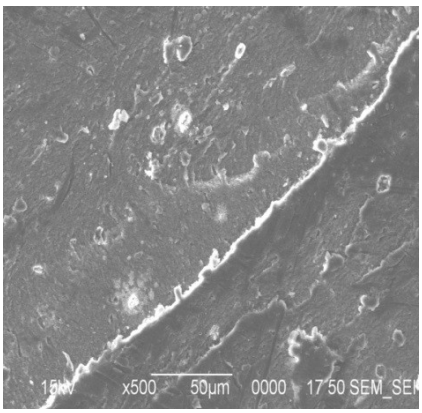

(b)

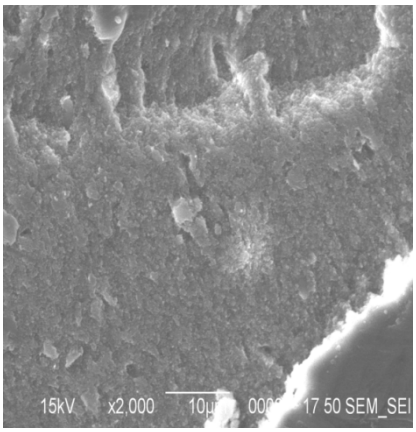

(c)

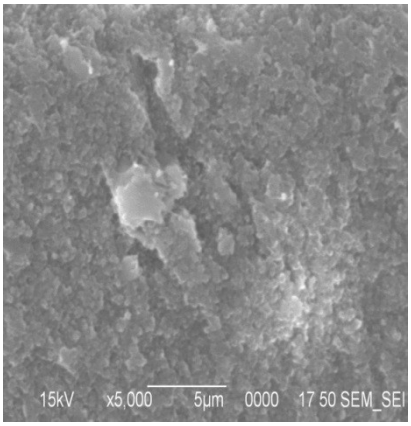

(d)

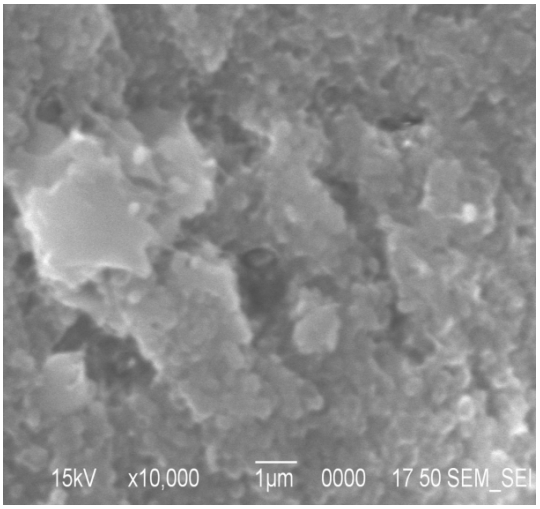

(e)

Figure 2.4-9. SEM images of Teflon powder pressed into a pellet.

The sandpaper abrading of the Teflon sheet was apparent. The Teflon powder appeared to be made from 500 nm spherical particles, some of which had agglomerated into larger particulates. It was concluded that Teflon facilitates the photolysis by promoting H_2 bubble formation, thus removing products from the reaction zone and enabling the photoreaction to proceed.

Teflon is a very low surface energy material. If hydrophobic interactions are the key to fast photoelectrolysis, then possibly using a surfactant would help. Triton X-100, a common non-ionic surfactant employed in polarographic analysis, is a highly adsorptive liquid that may promote bubble formation. Its molecular structure is shown below in Figure 2.4-10. The left hand side of the molecule as drawn is hydrophobic, while the right hand side is hydrophilic.

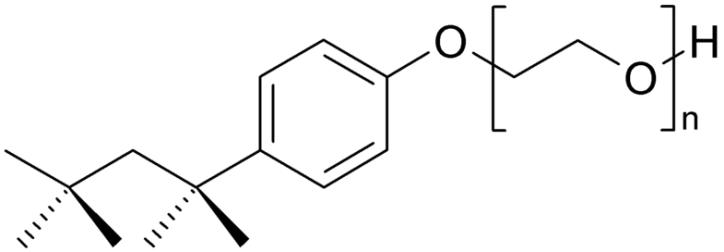

Figure 2.4-10. Molecular structure of Triton X-100.

However, the surfactant must be stable against photoreaction. A few drops were added to a standard sulfide/sulfite solution with Pt-CdS. After a two-hour photolysis, the solution had turned pink! That had never been observed before in all the previous experiments, so it had to be due to decomposition or complexation of the surfactant with other reagents. If surfactants are to be employed, one with greater photostability must be identified.

Blending a low surface energy additive such as Teflon® to the photocatalyst caused an improvement in H_2 gas evolution, which is directly related to the effectiveness of sulfide removal. Another way to alter the bubble-forming capacity is to add a surfactant to the solution. Accordingly, two drops of surfactant (Triton X-100) added to the system (25 ml of 0.24 M Na_2S and 25 ml of 0.34 M Na_2SO_3 in a 50 ml test tube containing platinized photocatalyst) showed decreased uniform bubble size and increased hydrogen gas volume. Hydrogen gas evolved was less when compared to abraded Teflon sheet, but together (abraded Teflon sheet and the surfactant) in the system gave more hydrogen gas than both alone as shown in Table 2.4i. After letting the solution stand for some time it turned pink, showing that the surfactant was not photostable. Having to add surfactant to the sulfide scrubber more or less continuously would be problematic, as the decomposition products would build up in the system and eventually start interfering with the photocatalyst performance, both from adsorption and also blocking the incoming illumination.

Table 2.4i. Effect of surfactant on hydrogen gas evolution

Sample #	Contents in the test-tube	Gas evolved (ml)
1	25 ml of 0.24 M Na_2S and 25 ml of 0.35 M Na_2SO_3 , 1 g of platinized CdS and abraded	15

	Teflon sheet.	
2	25 ml of 0.24 M Na_2S and 25 ml of 0.35 M Na_2SO_3, 1 g of platinized CdS and 2 drops of Triton X-100 surfactant	13
3	25 ml of 0.24 M Na_2S and 25 ml of 0.35 M Na_2SO_3, 1 g of platinized CdS, abraded Teflon sheet and 2 drops of Triton X-100 surfactant	16

To know if the photocatalyst can perform under different solution conditions, the following experiments were performed with 1.8 g of platinized adsorbent (CdS), under simulated sunlight.

Different solutions of varying sulfide concentration were prepared, keeping pH constant at 10. The sulfide concentrations tested were 0.24, 0.20, 0.15, 0.10, 0.05, and 0.01 M Na_2S. The results are shown below in Table 2.4j.

Table 2.4j. Effect of sulfide concentration on gas evolution.
pH 10; no sulfite added

Sample #	Concentration of solution	Volume of gas evolved (ml)
1	0.24 M Na_2S	8
2	0.20 M Na_2S	7
3	0.15 M Na_2S	6
4	0.10 M Na_2S	6
5	0.05 M Na_2S	5
6	0.01 M Na_2S	5

From Table 2.4j, it is evident that as the concentration decreased from 0.24 M to 0.01 M, volume of gas evolved also decreased, from 8 ml to 5 ml. The fact that gas evolution dropped only 37.5% (actually 60%, as these values include a 3 mL background) with a 96% drop in sulfide concentration indicates a nonlinear effect, where the rate limiting step is not directly dependent on sulfide concentration.

A solution of 0.24 M sodium sulfide was prepared and the pH was varied from 5 to13 keeping the concentration constant. To the prepared solution, one gram of adsorbent (platinized MoS_2) was added and this solution was exposed to a 1000 W xenon arc lamp for 2 h. The gas evolved was measured.

Table 2.4k. Effect of pH on gas evolution and sulfide oxidation.
0.24 M sodium sulfide solution

Sample number	pH	Volume of gas evolved (ml)
1	5	33
2	6	20
3	7	18
4	8	9
5	9	9
6	10	12
7	11	9

8	12	9
9	13	9

From Table 2.4k, at pH 5-7 the volume of gas was the highest. This result is misleading, because most of the sulfide at that pH consists of dissolved H_2S gas. Warming the test solution under illumination likely caused substantial amounts of H_2S to be evolved along with the H_2. From pH 8-13, evolved gas volume remained the same, as most of the sulfide was dissolved hydrosulfide ion, HS^-(aq). The comparatively higher value for sample 6 is considered to be an artifact. It would appear that for constant sulfide concentration, reaction rate is independent of pH.

For the actual landfill, the ability to influence scrubber pH will be quite limited. Landfill gas consists primarily of methane, carbon dioxide, and nitrogen. Of these, only carbon dioxide would influence the pH of an aqueous scrubber solution. It behaves as an acid gas, undergoing hydrolysis to generate carbonic acid:

$$CO_{2\,(g)} + H_2O_{\,(aq)} \longrightarrow H_2CO_{3\,(aq)} \longrightarrow H^+_{\,(aq)} + HCO_3^-{}_{(aq)}.$$

Scrubber pH will thus be determined more from the equilibrium between CO_2 and water than anything else. Based on equilibrium calculations, we estimated that scrubber pH could be as low as 3.9, assuming CO_2 content of 40% by volume.

To confirm this hypothesis, we visited the landfill (New Springfield, OH) with the intent of directly measuring pH of an aqueous solution in equilibrium with landfill gas. An experiment was conducted where landfill gas was bubbled continuously into 150 ml of water in a 4-neck round bottom flask. pH and ISE (Ion Selective Electrode) potential were measured simultaneously with time. The setup of the experiment is shown in Figure 2.4-11. This was done on a cool day (< 30 F), so the temperature of the solution in the flask was only 10 ˚C. All the readings are shown in Table 2.4l.

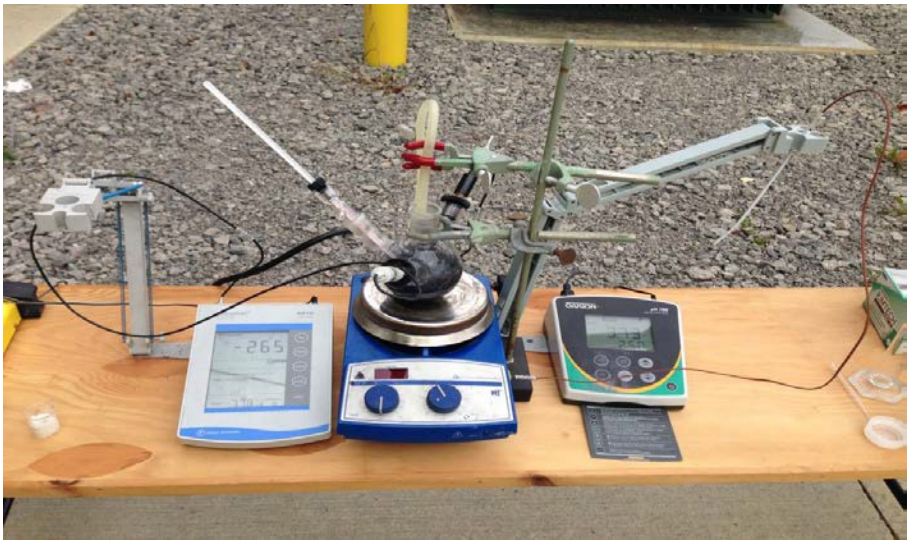

Figure 2.4-11. Set-up for the landfill gas experiment

Table 2.4l. pH and ISE readings for landfill gas (bubbled into water) with time

Sample #	Time (min)	pH	ISE (mV)
1	0	5.98	35
2	1	4.28	-25
3	2	4.23	-144
4	3	4.22	-266
5	4	4.21	-338
6	5	4.21	-353
7	6	4.21	-356
8	7	4.21	-357
9	8	4.21	-358
10	9	4.21	-358
11	10	4.21	-359
12	11	4.24	-361
13	12	4.24	-361
14	13	4.25	-361
15	14	4.25	-361
16	15	4.25	-362
17	16	4.25	-362
18	17	4.25	-362
19	18	4.25	-363
20	19	4.25	-363
21	20	4.28	-364
22	21	4.29	-364
23	22	4.30	-364

The pH did drop from near neutrality to as low as 4.2 in a matter of minutes. This corresponds reasonably well with earlier measurements putting the CO_2 content of the landfill at 36% by volume. The ISE reading corresponded to a very low sulfide concentration, much less than what 120 ppm should generate. At room temperature (25°C) back in the laboratory, the final pH was 4.21 and ISE was -252 mV, an even lower sulfide concentration.

A second experiment was conducted in which landfill gas was also bubbled into 150 ml of water containing 1 gm of platinized molybdenum sulfide in a 4-neck round bottomed flask. pH and ISE were measured with time at 10 °C. Results are shown in Table 2.4m.

Table 2.4m pH and ISE of landfill gas (bubbled into water with Pt-MoS_2) with time.

Sample #	Time (min)	pH	ISE (mV)
1	0	3.77	71
2	1	3.72	-117
3	2	3.71	-229
4	3	3.70	-256
5	4	3.69	-276
6	5	3.69	-285
7	6	3.69	-288
8	7	3.69	-288

9	8	3.69	-288
10	9	3.69	-288
11	10	3.70	-285
12	11	3.70	-283
13	12	3.70	-282
14	13	3.70	-280
15	14	3.70	-279
16	15	3.70	-277
17	16	3.70	-275
18	17	3.70	-274
19	18	3.70	-272
20	19	3.70	-271
21	20	3.71	-271
22	21	3.72	-270
23	22	3.72	-268
24	23	3.72	-268
25	24	3.72	-266
26	25	3.72	-266
27	26	3.73	-266
28	27	3.73	-266
29	28	3.73	-265
30	29	3.73	-265

The MoS_2 powder already added some measure of acidity to the solution, so that the CO_2 content from the landfill gas was unable to lower pH any further. ISE potential leveled out at a more positive value than before, indicating an even lower sulfide concentration. This may be attributable to sulfide adsorption by MoS_2. At room temperature back in the laboratory, pH was 4.26 and ISE was -196 mV.

The low sulfide readings would suggest that the presence of carbon dioxide in landfill gas serves to decrease the dissolution of H_2S into pure water. Therefore, an experiment was conducted back in the laboratory to observe the effect of CO_2 on H_2S dissolution. By continuously monitoring pH and ISE readings, a 100 ppm H_2S in methane mixture was bubbled into the system for 15 minutes. Then CO_2 was bubbled into the system to decrease the pH to 4.20. ISE readings were taken once CO_2 purging began. It was seen that ISE potential increased over 200 mV, corresponding to a sulfide concentration drop of over 3 orders of magnitude. From the results listed in Table 2.4n, it is evident that CO_2 present in the system decreases the dissolution of H_2S.

Table 2.4n. Effect of CO_2 on H_2S dissolution

Time (min)	pH Reading	ISE Reading
0	7.22	23
1	7.64	-131
2	7.58	-232
3	7.58	-343
4	7.58	-419

5	7.59	-440
6	7.62	-469
7	7.64	-503
8	7.66	-519
9	7.68	-534
10	7.68	-543
11	7.71	-551
12	7.72	-552
13	7.73	-559
14	7.74	-559
15	7.75	-562
CO_2 bubbled into the system		
16	4.48	-351
17	4.45	-348
18	4.42	-347
19	4.42	-345
20	4.42	-341

The H_2S concentration was once again measured to compare to values during earlier sampling opportunities. From Figure 2.4-12, it is clear that the concentration of hydrogen sulfide in the landfill gas is now 200 ppm, up 40% from earlier measurements. This could be due to many factors, such as seasonal temperature, variable gas flow rate through the landfill (it is held under negative pressure with the use of compressors), and fluctuations in solid waste composition. Color change is observed from white to dark brown. This higher reading will necessitate even greater measures to control sulfur entry into the SOFC.

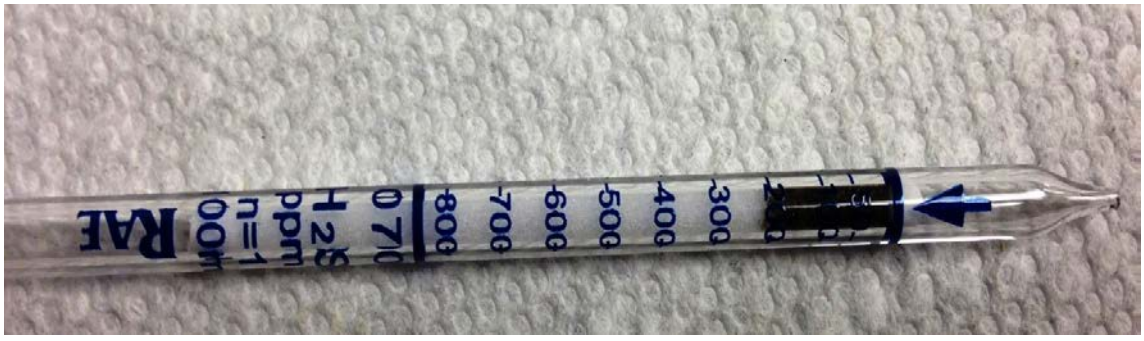

Figure 2.4-12. H_2S concentration in landfill gas detected by RAE tubes

Despite what was learned from the experiments above, it was decided to continue on and assess the ability of MoS_2 to adsorb and photochemically decompose H_2S in landfill gas. The first step was to immobilize the MoS_2 adsorbent on a substrate, so that sulfide solution could be made to flow across it. The adsorbent was painted onto a 0.125" acrylic plastic plate as shown in Figure 2.4-13. To paint the plastic surface, 1 part of poly (methyl methacrylate) is mixed with 9 parts of

solvent (methylene chloride) and 9 parts of solid filler (70% platinized MoS_2 and 30% Teflon by weight).

Figure 2.4-13. Acrylic flat painted with a mixture of platinized MoS_2 and Teflon.

The painted substrate was then mounted in a "flat cell" with glass window as shown in Figure 2.4-14. The cell was designed to accommodate the 4" square acrylic flat and allow for open illumination across the surface. The separation distance between the aperture of the Xe lamp and the flat cell will be approximately 12 cm.

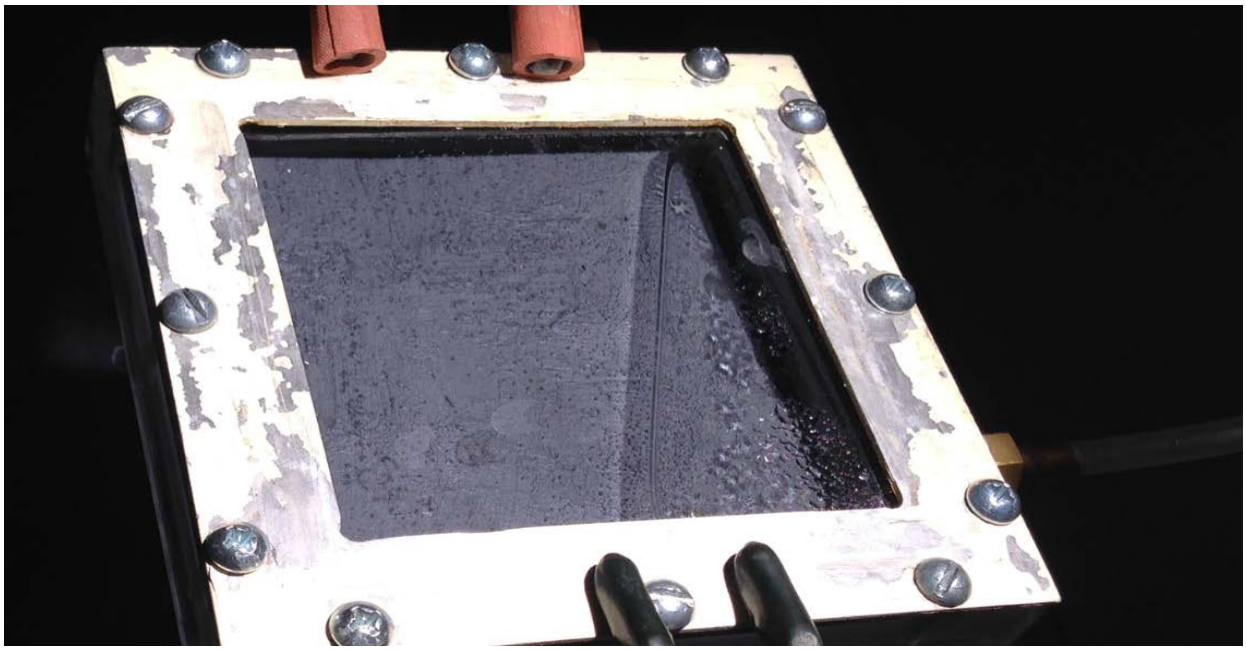

Figure 2.4-14. Flat cell containing platinized molybdenum sulfide adsorbent on 4" square acrylic substrate.

The simulated landfill gas conditions were pH = 4.2 and H_2S concentration = 50 ppm. The cell was placed under a solar simulator while scrubber solution was circulated through it. Any pressure build-up inside the cell was measured by gas evolution into an inverted graduated cylinder. The entire apparatus is shown in the schematic below (Figure 2.4-15).

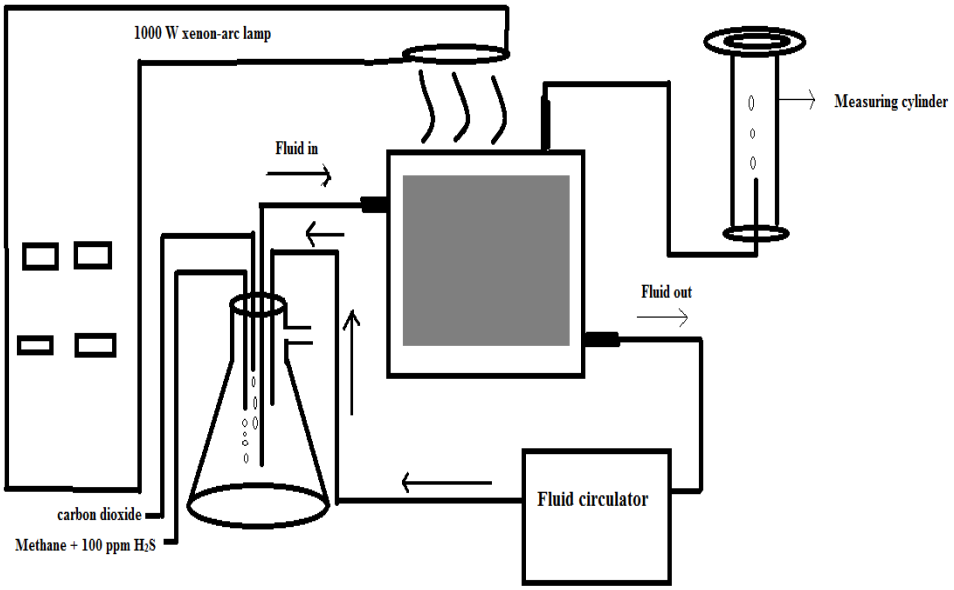

Figure 2.4-15. Schematic of simulated landfill gas scrubbing experiment.

The experiment was conducted for 2 hours continuously under simulated sunlight (1000 W xenon arc lamp). Working cell volume was 100 ml. About 124 ml of gas was collected into the cylinder. Gas chromatography was used to characterize the gas evolved in the photo experiment. A simple schematic of the gas chromatograph with thermal conductivity detector is shown in Figure 2.4-16.

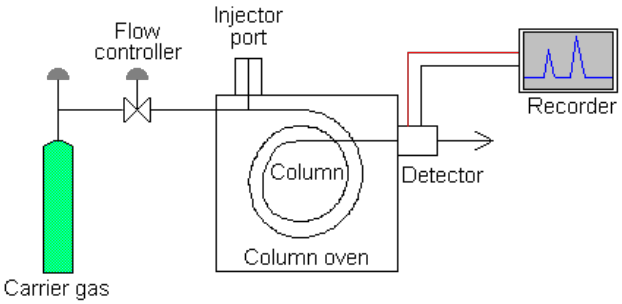

Figure 2.4-16. Instrumental components of gas chromatography

Gas evolved from the photo-experiments was tested by manually injecting samples into the gas chromatograph. Temperatures of injector, column and detector were 43 °C, 63 °C and 32 °C,

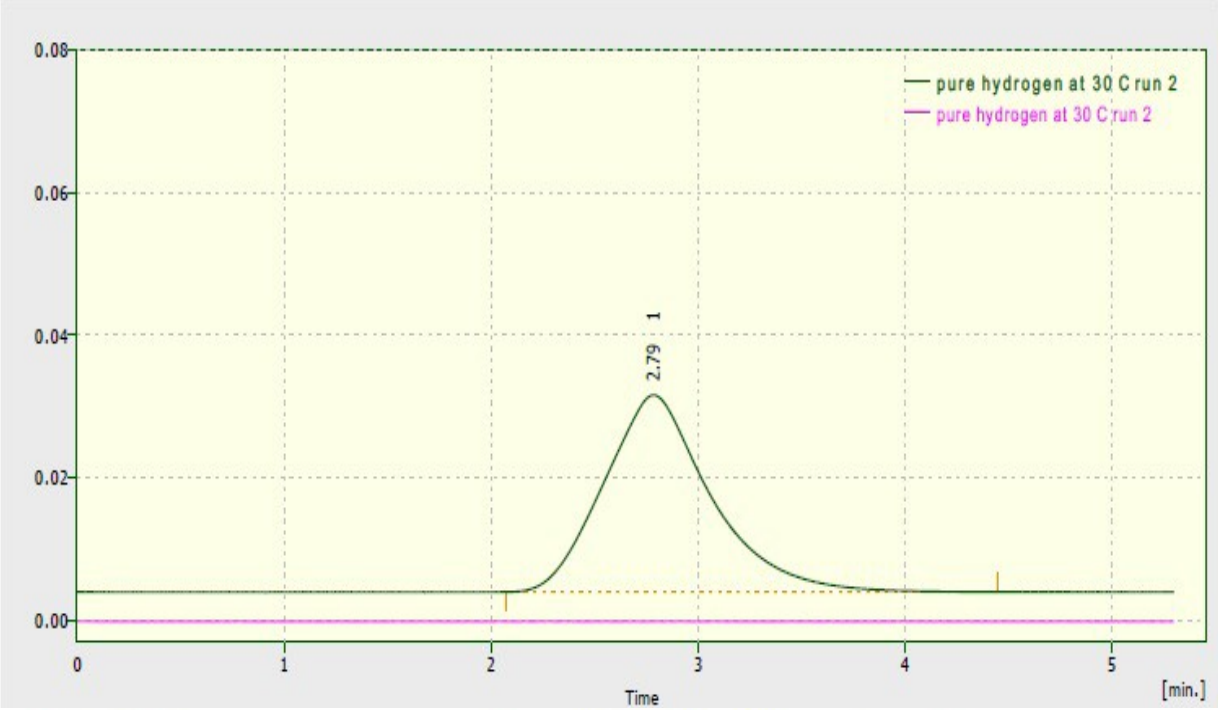

1/16/2014 9:47 AM Chromatogram C:\Clarity Lite\WORK1\DATA\pure hydrogen at 30 C run 2.PRM Page

Result Table (Uncal - pure hydrogen at 30 C run 2)

	Reten. Time [min]	Area [mV.s]	Height [mV]	Area [%]	Height [%]	W05 [min]	Compound Name
1	2.787	997.200	27.666	100.0	100.0	0.54	
	Total	997.200	27.666	100.0	100.0		

Result Table (Uncal - pure hydrogen at 30 C run 2)

Reten. Time [min]	Area [mV.s]	Height [mV]	Area [%]	Height [%]	W05 [min]	Compound Name
No peak to report						

Figure 2.4-17. Gas chromatograph of pure hydrogen at 32 ˚C

respectively. The type of column used was a Poropak Q adsorbent packed in stainless steel tube that was 8 feet long and 0.125 inch in diameter. The particle size of the adsorbent was 80/100 mesh. Detector temperature was maintained at 50 mA. Argon was used as a carrier gas, as it more sensitivity for hydrogen.

Sample injections of 1.0 ml of the following gas samples were made and the chromatographs collected are shown in Figures 2.4-17-20

1. Pure hydrogen
2. Pure air
3. 1:1 hydrogen to air
4. Gas evolved from landfill simulation experiment

1/13/2014 7:38 PM Chromatogram C:\Clarity Lite\Work1\DATA\pure air at 30 C.PRM Page 2 of 2

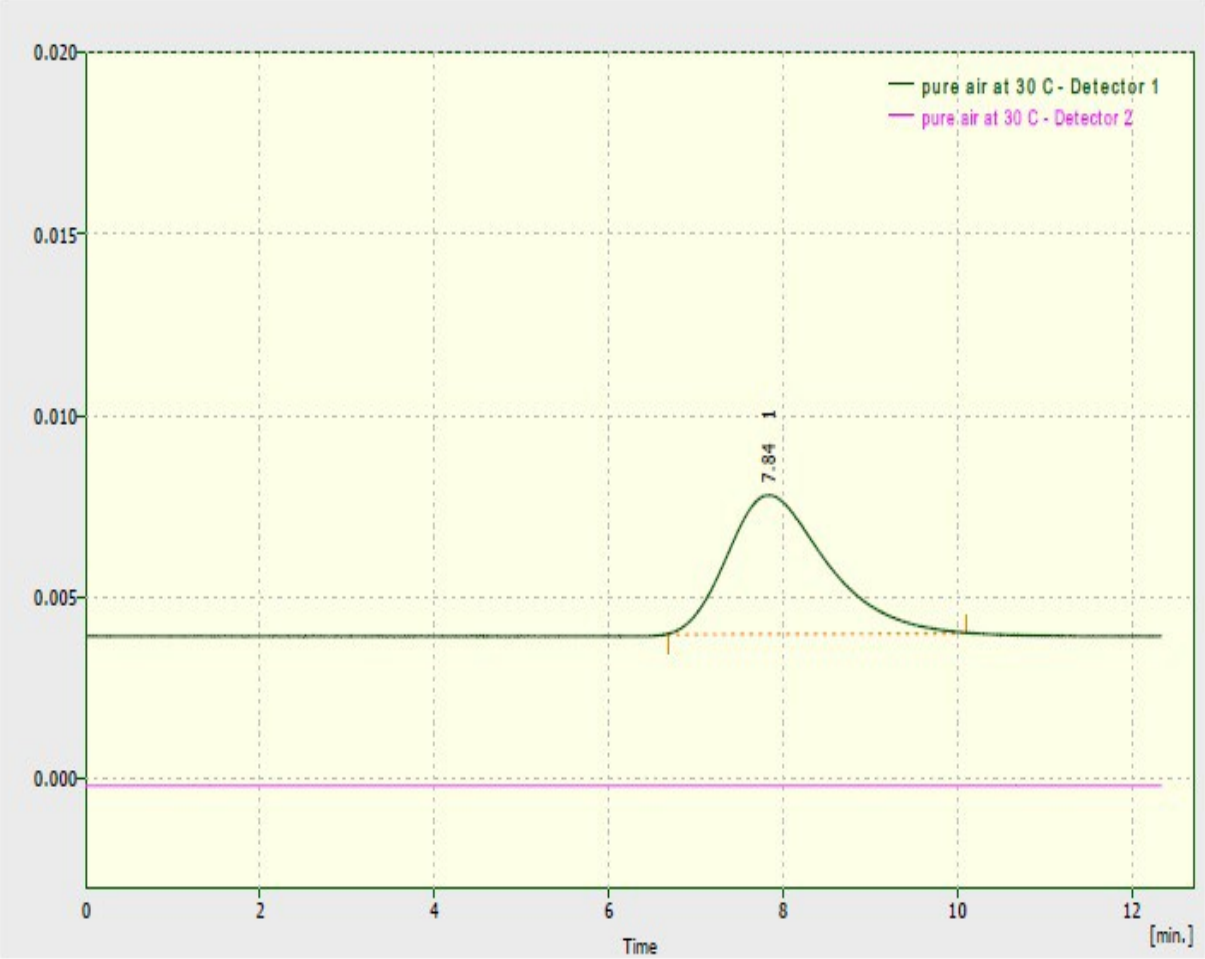

Result Table (Uncal - pure air at 30 C - Detector 1)

	Reten. Time [min]	Area [mV.s]	Height [mV]	Area [%]	Height [%]	W05 [min]	Compound Name
1	7.844	304.180	3.823	100.0	100.0	1.21	
	Total	304.180	3.823	100.0	100.0		

Result Table (Uncal - pure air at 30 C - Detector 2)

Reten. Time [min]	Area [mV.s]	Height [mV]	Area [%]	Height [%]	W05 [min]	Compound Name
No peak to report						

Figure 2.4-18. Gas chromatograph of pure air at 32 ˚C

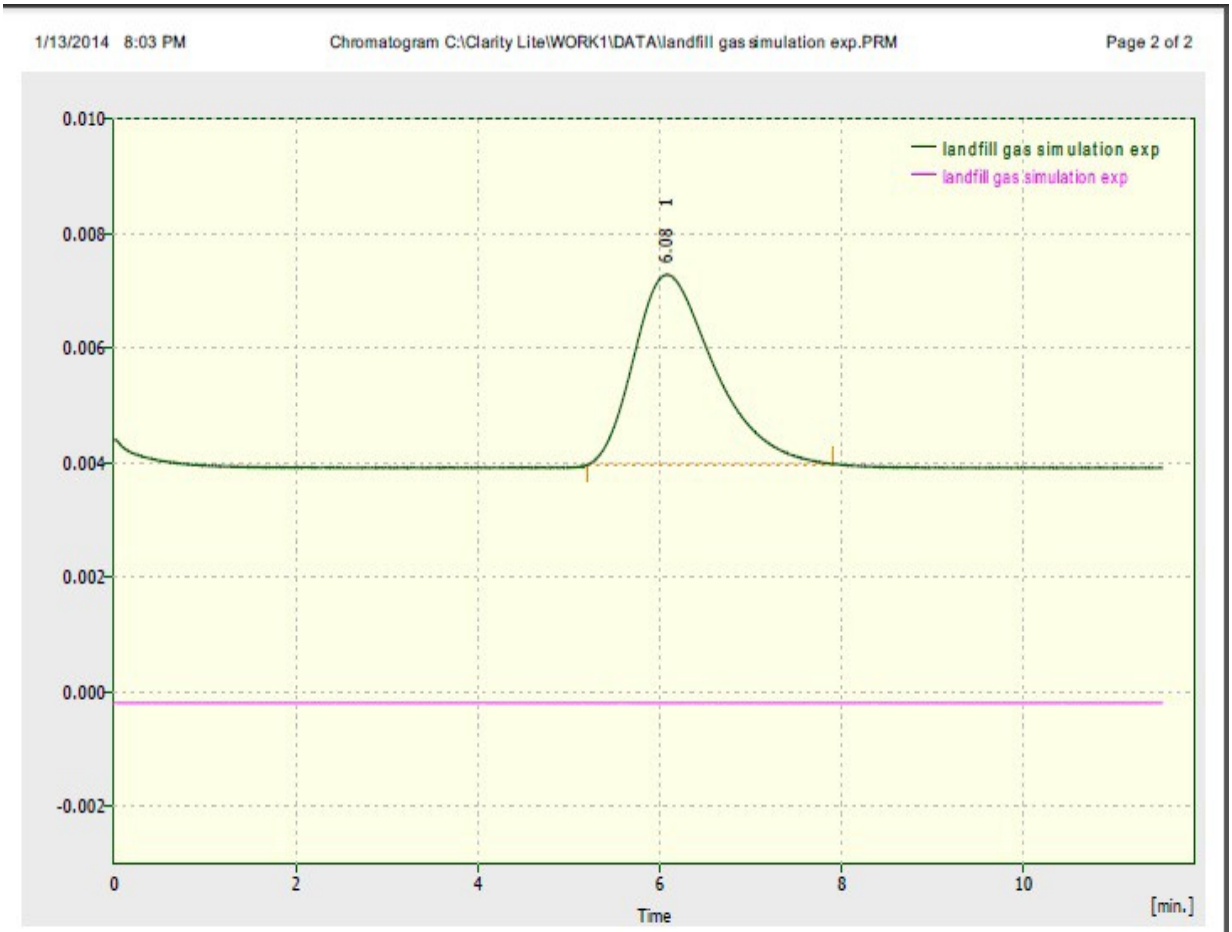

Result Table (Uncal - landfill gas simulation exp)

	Reten. Time [min]	Area [mV.s]	Height [mV]	Area [%]	Height [%]	W05 [min]	Compound Name
1	6.076	204.128	3.325	100.0	100.0	0.94	
	Total	204.128	3.325	100.0	100.0		

Result Table (Uncal - landfill gas simulation exp)

Reten. Time [min]	Area [mV.s]	Height [mV]	Area [%]	Height [%]	W05 [min]	Compound Name
No peak to report						

Figure 2.4-19. Gas chromatograph of 1:1 ratio of air and hydrogen at 32 ˚C

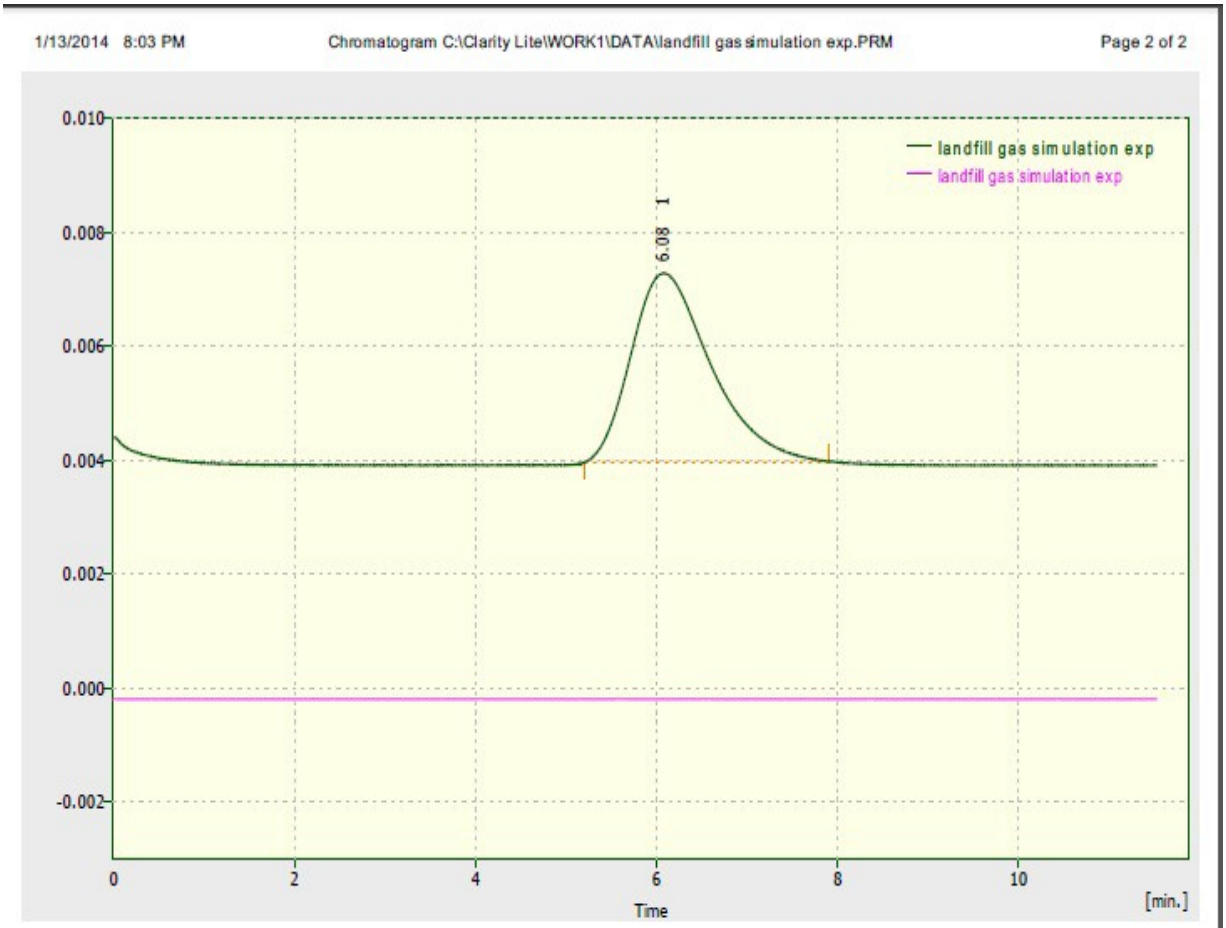

Result Table (Uncal - landfill gas simulation exp)

	Reten. Time [min]	Area [mV.s]	Height [mV]	Area [%]	Height [%]	W05 [min]	Compound Name
1	6.076	204.128	3.325	100.0	100.0	0.94	
	Total	204.128	3.325	100.0	100.0		

Result Table (Uncal - landfill gas simulation exp)

Reten. Time [min]	Area [mV.s]	Height [mV]	Area [%]	Height [%]	W05 [min]	Compound Name
No peak to report						

Figure 2.4-20. Gas chromatograph of gas evolved from landfill gas simulation experiment at 32 ˚C

These figures confirm that we did not make any hydrogen. We consider this a confirmation of the CO_2 effect on the solubility of H_2S in water making much less sulfide available for the photocatalyst. It also means that another method should be employed to clean up landfill gas. Nonetheless, composition of impurities in landfill gas was reduced sufficiently to allow successful operation of the test fuel cell.

Subtask 2.5 Comparison to a PEM fuel cell system.

A proton exchange membrane fuel cell was received and assembled. The gas mixing and current/voltage monitoring systems installed for the Probostat⇔ button cell testing were also employed in this subtask. Current-voltage behavior was observed for humidified H_2 vs air in order to obtain baseline performance of the fuel cell. The resulting data is plotted below in Figure 2.5-1. The power output of the cell across a load resistor is also plotted.

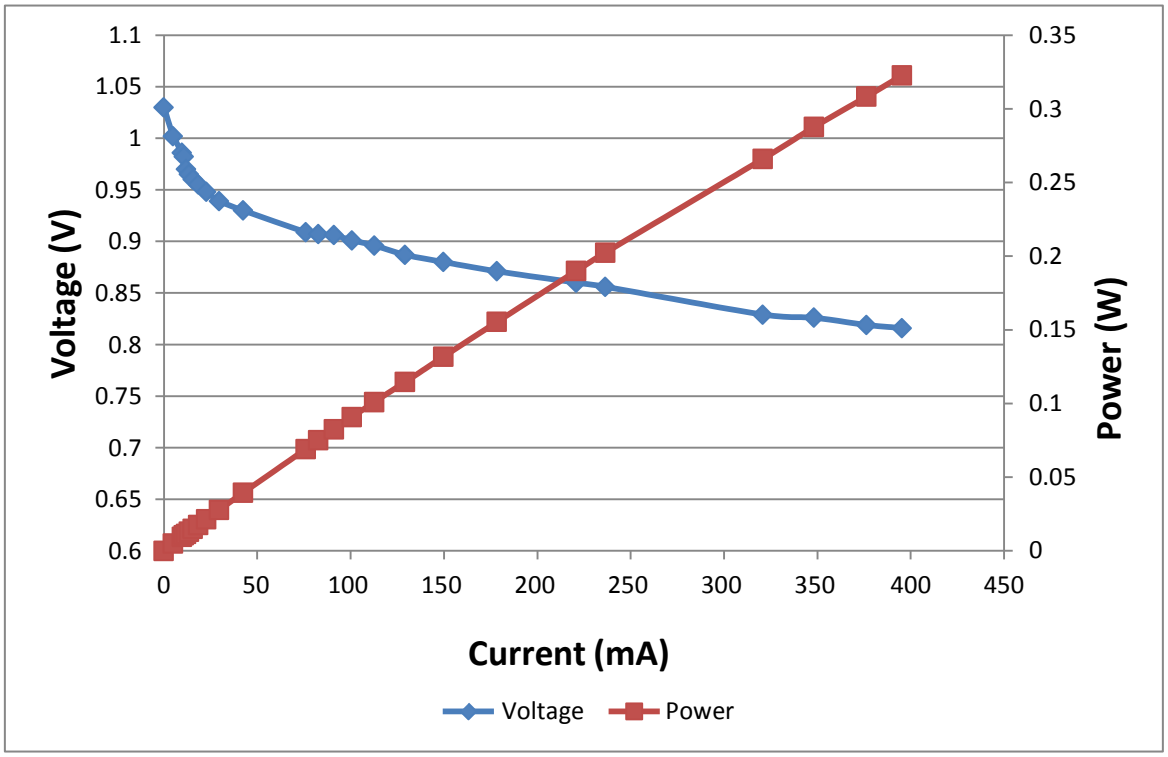

Figure 2.5-1. Dual plot of voltage and power vs current in a 25 cm^2 PEM fuel cell. The H_2 was pre-humidified in a water bath at 80 ^oC and the fuel cell was heated to 80 ^oC.

It is seen that, at least under ultrapure H_2, a PEM cell at moderate temperature delivers electricity as efficiently as an SOFC at high temperature. This was not unexpected, although various components of landfill gas are expected to effect the performance of the PEM cell. The baseline performance under H_2 is shown below in Figure 2.5-2.

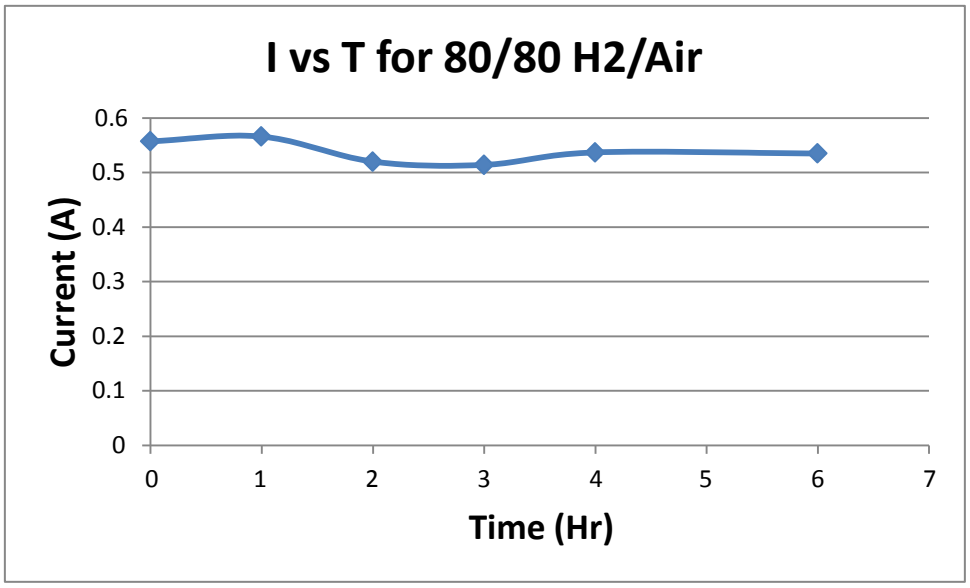

Figure 2.5-2. Current vs time for a 25 cm^2 PEM fuel cell run on humidified, ultrahigh purity H_2 versus air.

It is shown that after more than six hours of continuous operation, there is hardly any drop in current in comparison to the initial value. A slight deviation from steady state was observed in the two to four hour range. This could be due to many extraneous factors, including changes in humidification level, fluctuations in line voltage fed to the fuel cell heater, or temporary water condensation build-up inside the cell.

The following describes our findings upon feeding simulated landfill gas into the electrochemical cell. As shown in Figure 2.5-3 below, a feed gas consisting of 1:1:2 $CH_4/CO_2/H_2O$ entering the PEM cell at 80 ^oC was unable to sustain a voltage, decaying to zero output after just over an hour's operation. This is in contrast to the SOFC at 750 ^oC, which can sustain current and voltage output from this feed gas mixture indefinitely.

A similar feed gas mixture with 25 ppm H_2S was also tested with identical result. The passivation effect with CH_4 and CO_2 was overwhelming enough that the usual catalyst poison had little additional effect.

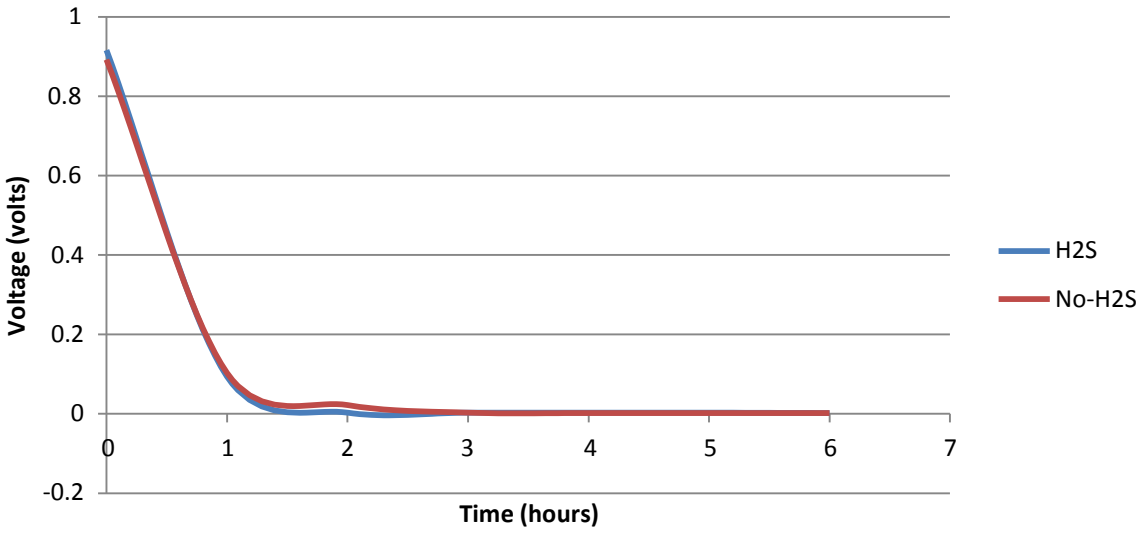

Figure 2.5-3. Voltage vs time for synthetic landfill gas (25% CH_4, 25% CO_2, 50% H_2O), with and without 25 ppm H_2S applied to a PEM fuel cell.

A summary of the impact of various diluent gases is shown below in Figure 2.5-4. The blue trace shows the effect of CO_2. The cell output is more or less constant up to > 90% diluents, or <10% H_2, before falling off. It is expected that the current would decay at very low H_2 pressure even in the presence of inert gases. In fact, CO_2 is essentially performing as an inert gas, serving only to reduce the concentration of reagent H_2. The effect of CH_4 (green trace) is similar, showing a very slow decay until the concentration limit of H_2 comes into play above 90% dilution. While the CH_4 is not appreciably acting as an electrocatalyst poison, it is nevertheless a particularly negative result, as it shows that the fuel value of landfill gas cannot be extracted by the PEMFC. The only way landfill gas could be used with a PEMFC would be to decompose the CH_4 outside the fuel cell either via steam reforming or pyrolysis and then feed the resulting H_2 and CO_2 into the cell.

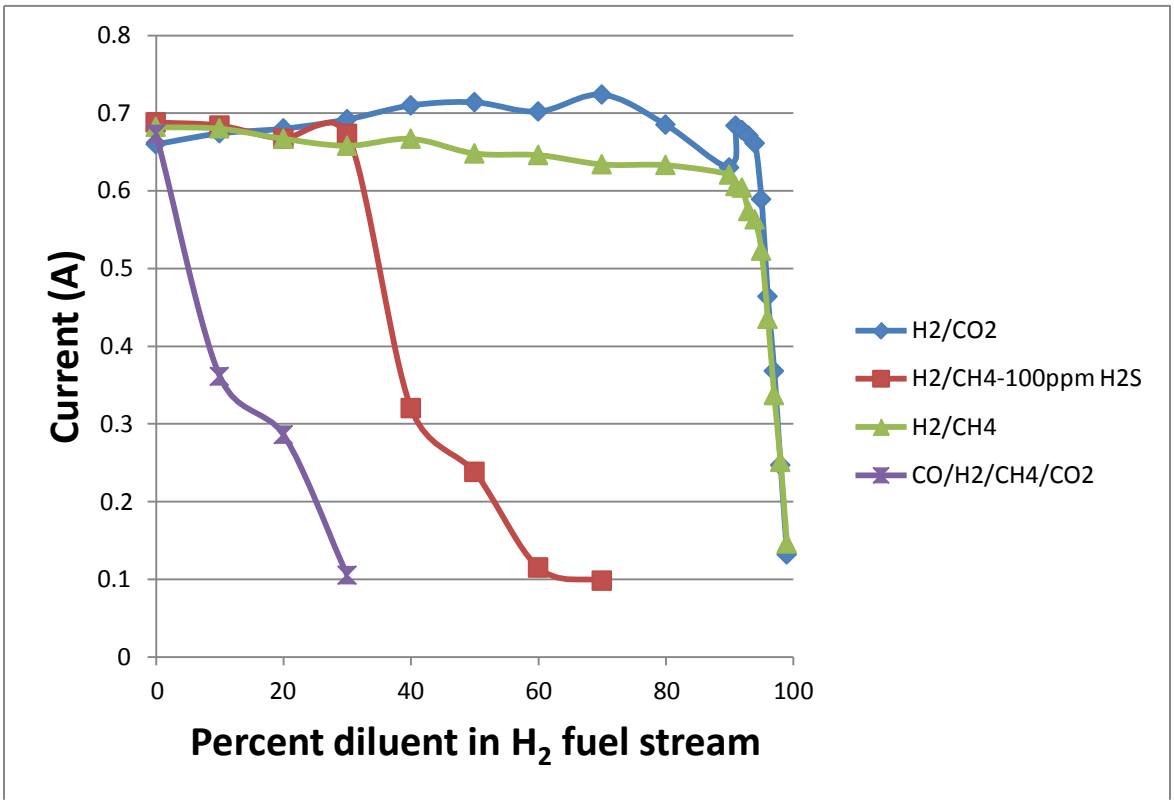

Figure 2.5-4. Current decay in a PEM fuel cell due to dilution with landfill gases.

The effect of H_2S is more pronounced. In the red trace, CH_4 is once again the diluent, but this time it contained 100 ppm of H_2S. The current dropped precipitously at only 30% diluent. This corresponded to a H_2S content of only 30 ppm. Thus H_2S will adsorb strongly to Pt and reduce its ability to electro-oxidize fuel.

Finally there is the effect of carbon monoxide. It is not a prime constituent of landfill gas per se, but would be formed at some level due to incomplete steam reforming:

$$CH_4 + H_2O \rightarrow CO + 3H_2$$

We did not employ pure CO, but rather made use of a calibration gas containing 25% each of CO, H_2, CH_4, and CO_2. Since CH_4 and CO_2 had been shown to be largely inert and H_2 was the active fuel gas being diluted, the four-component mixture could be used and deliver an unambiguous effect due to CO. This blended gas proved to be more than enough diluent CO, as the slightest introduction of the calibration standard caused a drop in current. Thus if a PEMFC were to be operated with landfill gas as the fuel, the gas would have to be treated for sulfur removal, and then processed in a reformer large enough to drive the equilibrium far toward the products, so that negligible CO would flow into the fuel cell.

Subtask 2.6 Analysis of a fuel cell running on landfill gas.

Due to the chemical instability of landfill gas, we were attempting to set up our fuel cell at the landfill, so that the feed gas to the fuel cell would consist of new gas just released from the earth. An agreement prepared by YSU counsel was signed by all parties, but then the landfill people produced a liability waiver of their own that tended to contradict the original language. It was too late to negotiate out the differences, as the landfill owners (Waste Management) were planning to begin feeding their gas to a commercial combustion generator starting in January 2013; site work had already begun, and they did not want us coming into a work zone and setting up equipment.

Therefore, we determined to go back to the original idea of going to the landfill, filling gas cylinders via compressor, bringing them back to the laboratory, and operating a fully instrumented SOFC. While some of the H_2S content will be lost due to chemisorption on the inner walls of the cylinders, we had made a decision to reduce H_2S down to single parts per million anyway; the proportions of the major constituents in the gas could be stored without change. As it turned out, the on-site alterations left intact the barb fitting where we had been collecting gas samples. We still have permission to come on-site and collect gas.

An important parameter in the evaluation of landfill gas as fuel for solid oxide fuel cells is the amount of carbon monoxide that is produced. This is the primary criterion by which the US Environmental Protection Agency classifies a landfill as a major or minor polluter. Hence it is imperative to have a valid measurement method for CO available.

This has been achieved using gas chromatography. Using a Gow-Mac gas chromatograph with a thermal conductivity detector, unambiguous determination of CO can be made, at least as a primary constituent. In Figure 2.6-1 below, a chromatogram for a gas mixture consisting of equal parts H_2, CO_2, N_2, CH_4, and CO is shown. Hydrogen is scarcely detectable, as its thermal conductivity is similar to that of the helium carrier gas, and so sensitivity is quite small. The other gases can be detected without difficulty. A two-column/bypass approach was adopted, wherein a bypass valve between the two columns controls whether a given gas constituent in a sample passes through one or both columns. In our case, all the gases pass through both columns except CO_2, which is kept out of the second column. That column contains molecular sieves that would otherwise be contaminated.

As a result, CO_2 is first to the detector, as it was not trapped in the second column with the other components (save for H_2, which appears as a small blip around 2 min). The peak near the 4 min mark is actually an artifact created when the bypass valve switches back to two-column mode. The order of elution from the second column was N_2, CH_4, and finally CO.

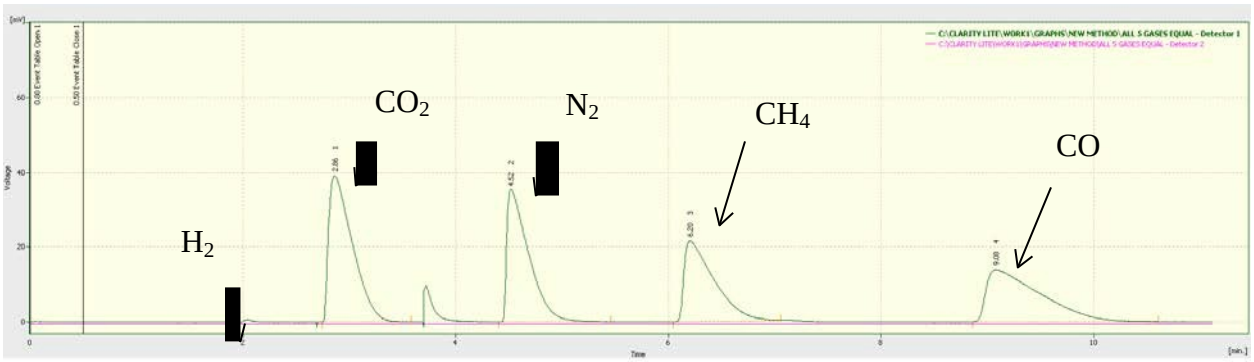

Figure 2.6-1. Chromatographic calibration curve for a gas mixture containing equal amounts of H_2, CO_2, N_2, CH_4, and CO.

The methodology used in subtask 2.5 was employed using a sample of real landfill gas and run through the SOFC operated at 750^{o}C. . The fuel cell and oven are ready, the chromatographic method is ready, the chemisorptive H_2S scrubber is ready, and the humidifier is ready.

Task 3 Plasma Controlled Turbine Blades

The objective of this task was to evaluate the improvement that could be gained by manipulation of the wind turbine blade during operation. Orbital Research was identified as a subcontractor based on their development of adjustable wind turbine blades. The plan was to install two identical wind turbines on a common site so that the performance of a wind turbine operating with standard blades could be compared against the adjustable wind turbine blade. YSU was to provide a site for the installation of the wind turbines and analysis of the energy collection data.

Subtask 3.1: Site Selection

Early in the development of this project, the wind turbines were intended to be installed on top of the YSU football stadium, selected based on high elevation, wind speed, building structure, and access for the researchers. Figure 3.1-1 shows the elevation, about 250 feet above the ground.

Figure 3.1-1: YSU football stadium, camera facing west

This site was also deemed appropriate due to the presence of concrete structures that would provide an excellent mooring site for the turbines, as shown in Figure 3.1-2. The main structural column will be attached as shown and additional guy lines attached between the turbine and the stadium roof.

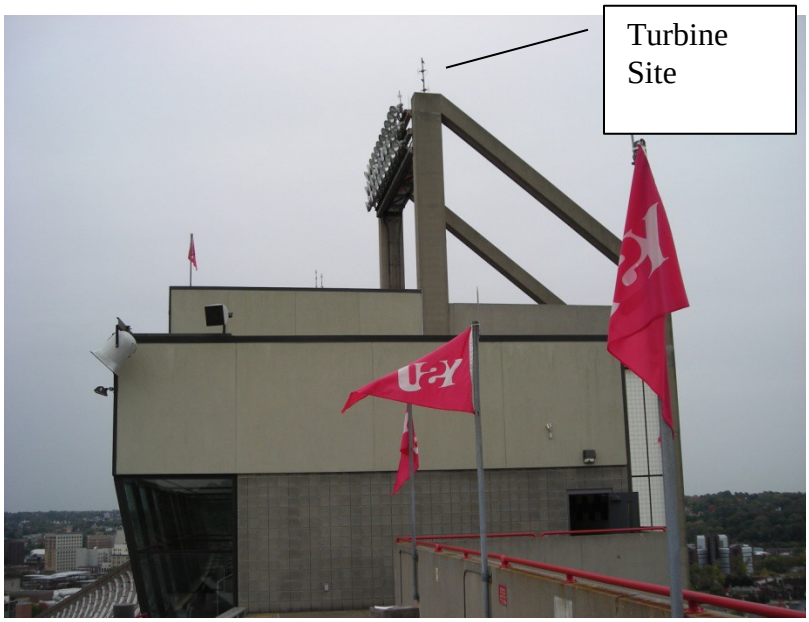

Figure 3.1-2: YSU football stadium, camera facing south

An anemometer was purchased and installed on the site, and initial data was collected. Correlations were made to 5 year and 30 year historical data from the local airport.

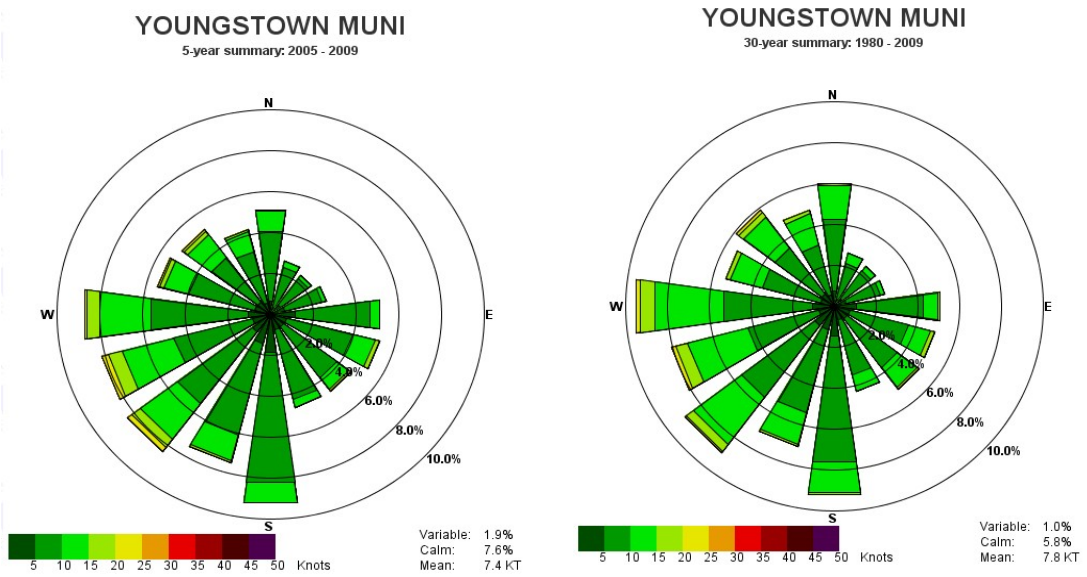

Figure 3.1-3 Summary of 5 and 30 year wind direction at Youngstown airport (source NOAA), shows that the prevailing wind is predominately from the west or the south.

The percentage of hours that the turbine spends at each wind speed is also avaiable from the airport data.

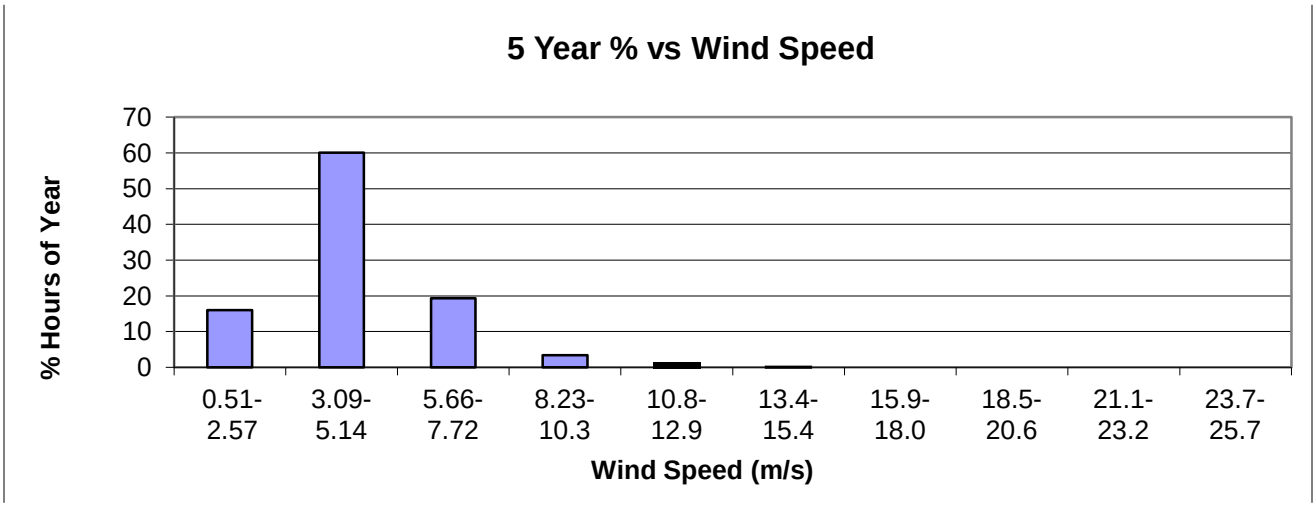

Figure 3.1-4 Summary of 5 year wind speed for Youngstown Airport (Source NOAA)

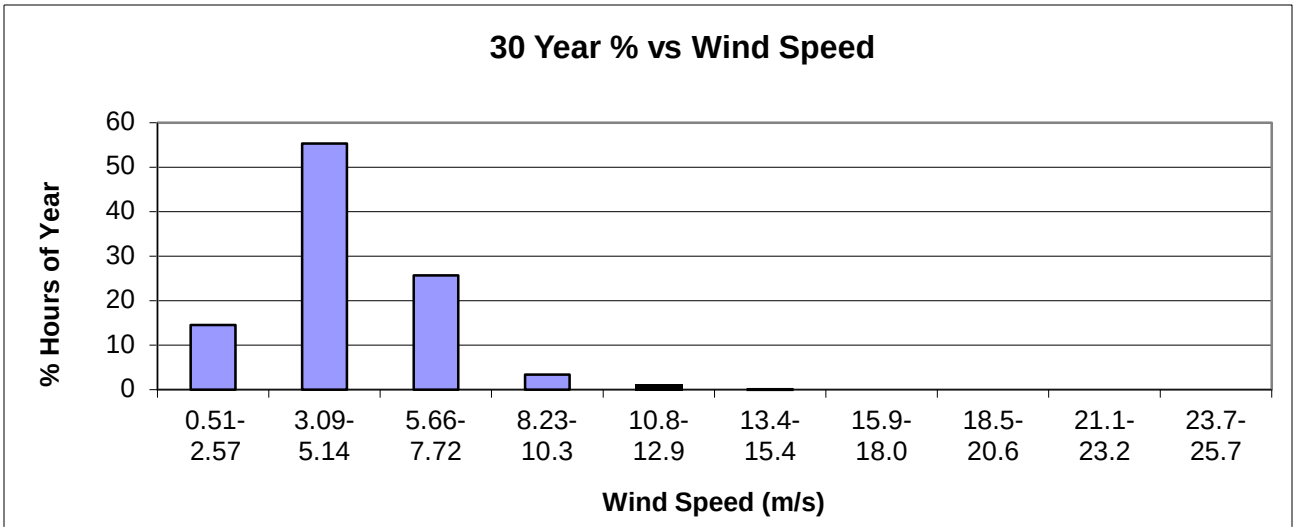

Figure 3.1-5 Summary of 30 year wind speed at Youngstown Airport (Source NOAA)

Review of Figures 3.1-4 and 3.1-5 shows a slight shift in the wind speed. The 5 year wind data has 5% more time in the 3.09 to 5.14 m/s speed interval, and about 5% less time in the 5.66 to 7.72 interval.

After reviewing the wind and geometric restraints, it was determined that the turbines would be installed facing west as shown in Figure 3.1-6.

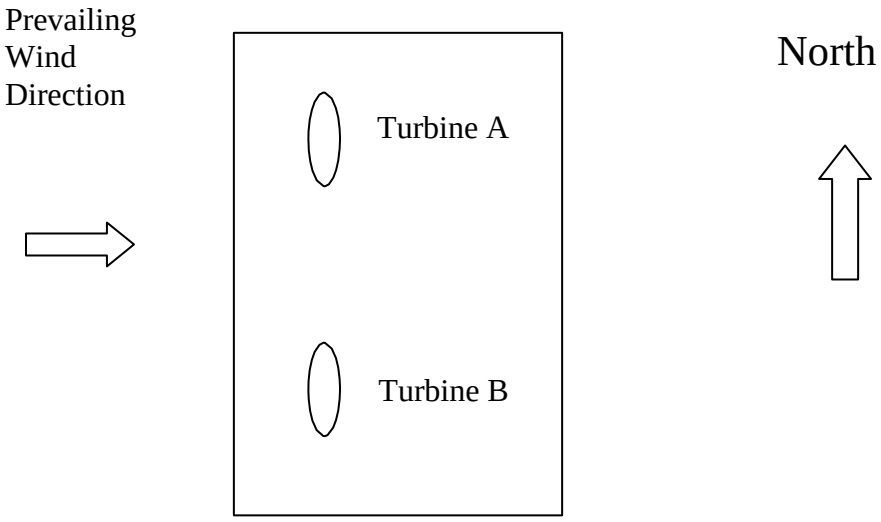

Figure 3.1-6 General Layout of Turbines

Further analysis was undertaken using computational fluid dynamic simulations on YSU Stambaugh Stadium, allowing us to visualize the flow structure around the YSU football stadium and determine/estimate the height and locations of shear layers and to identify most favorable locations to install the wind turbines.

CFD simulations were done on a full scale YSU Stambaugh stadium, with wind speed of 4.5m/s from 45 deg SW used. CFD grid contained in excess of 3.5 million tetrahedral elements.

Turbulence model used was RNG k-epsilon (linear turbulence solver in FLUENT). Time averaged simulations showed the presence of shear layers that extend at least 10-15m (~ 33-50ft) above the first light tower, as shown in Figure 3.1-7. This suggests that the boom or the pole holding up the wind turbine should be tall enough to exploit the high wind velocity. The trade-off however, could be the turbulent nature of the winds up in that height, which are a function of the instantaneous direction and other gusts etc.

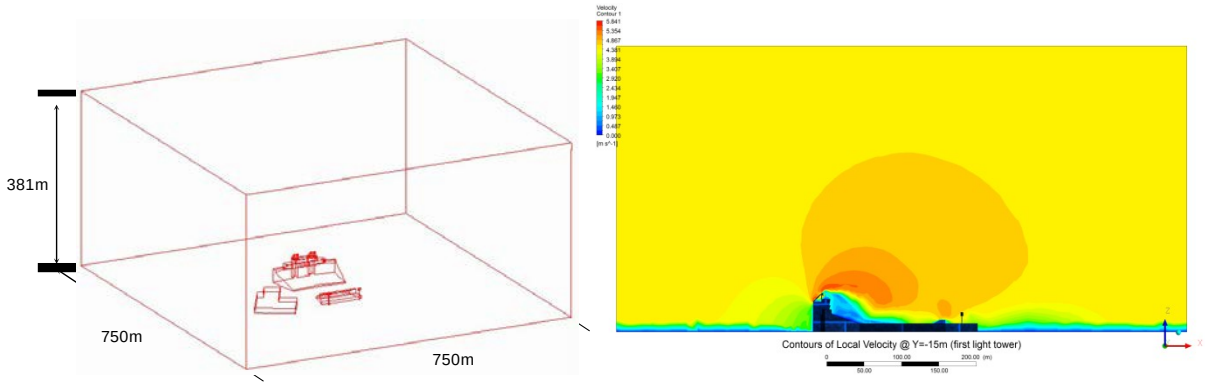

Figure 3.1-7: Schematic of the CFD domain at Stambaugh Stadium; Velocity contours at the first light tower.

Prior to final installation of the wind turbines atop the stadium roof, one additional structural evaluation was completed. Unfortunately, the site was determined to be unable to support the loads from the turbine and tower for high wind operation and for raising and lowering loads. As a result, the proposed location was rejected and work began to identify an alternate site.

The new site will use a ground- based system, selected using the criteria from before: (1) favorable wind speeds, (2) ease of installation, (3) visibility to the campus and public. A full detailed specification will be prepared and the installation efforts will be sent out for bid. While not as high above the ground, a ground-based installation will cost less and take less time than retrofitting an existing structure.

Several alternate sites were considered, as shown on the map in Figure 3.1-8:

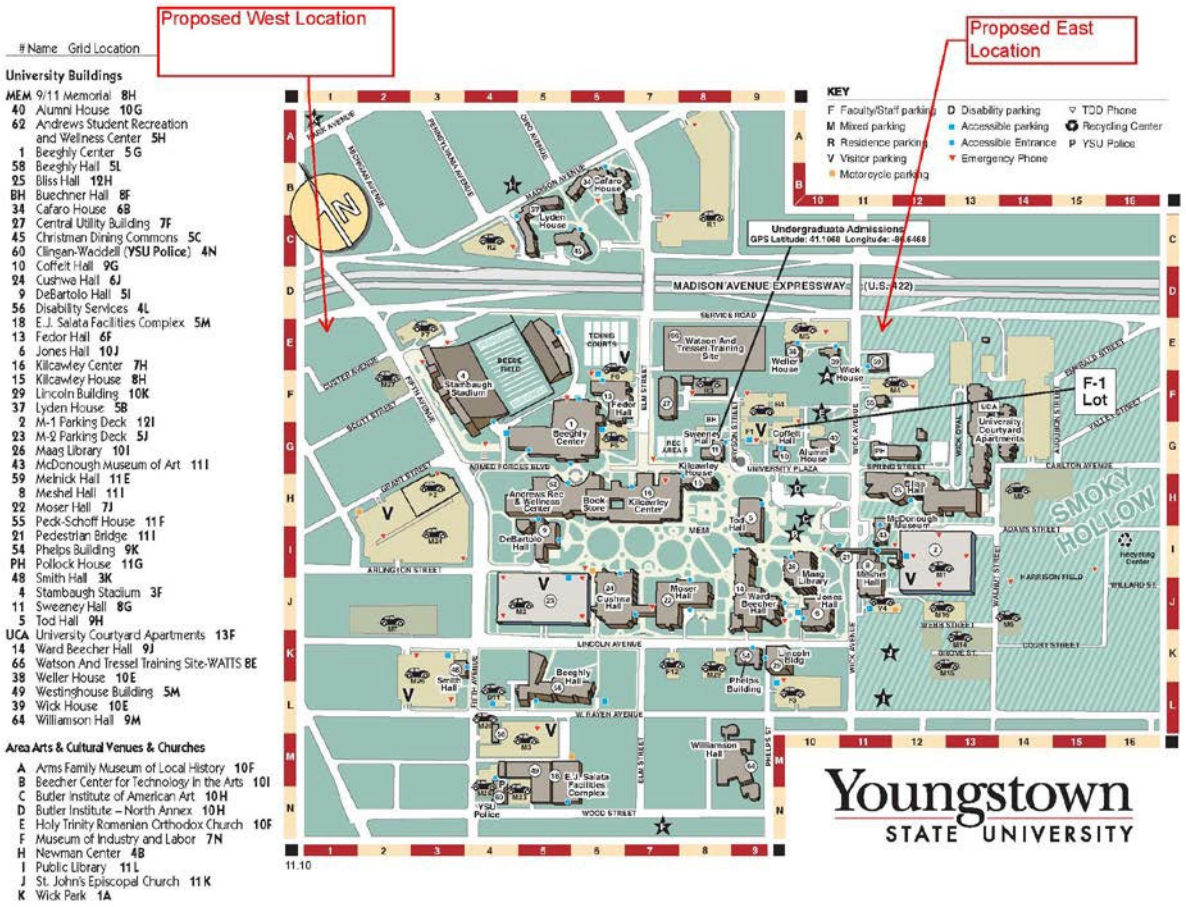

Figure 3.1-8 Proposed Turbine Locations

Installation at the East location was selected based on the criteria of availability, access for large cranes, nearby electrical service, and high visibility from the freeway.

Renderings of the installation at the new site was then prepared. The installation objective was combined with installation of another turbine being developed for a second project, but is included in the original renderings.

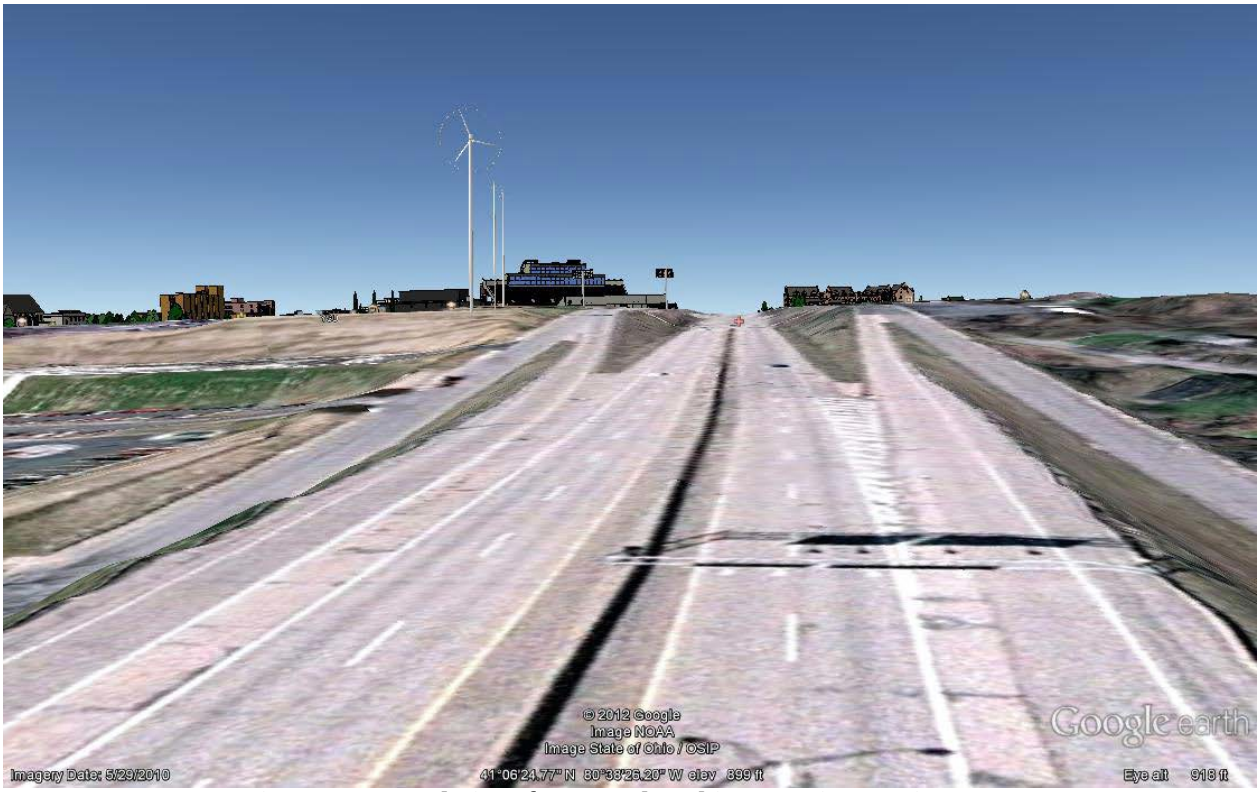

Figure 3.1-9 Rendering of Proposed Turbine Locations Facing West

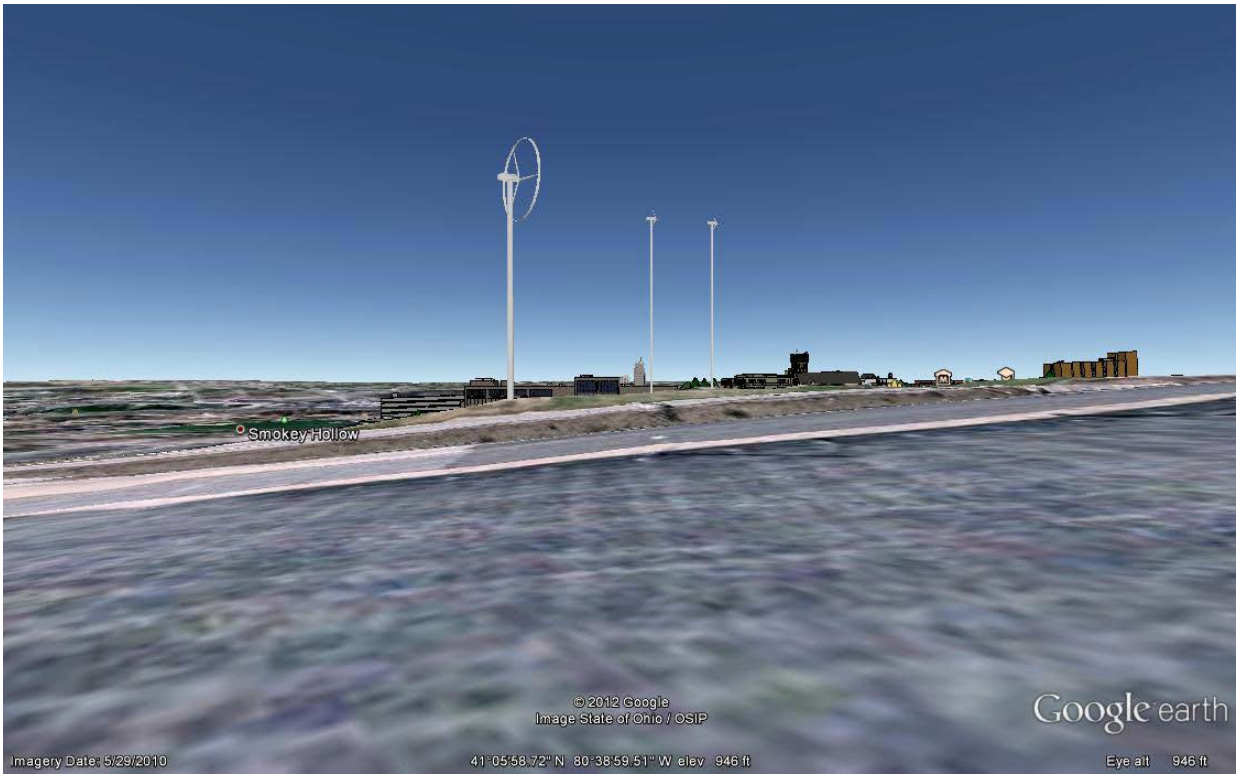

Figure 3.1-10 Rendering of Proposed Turbine Locations Facing Southwest

A wind analysis was completed for the alternate site, from which it was determined that the wind is predominantly from the south west, as shown in the wind study below:

Directional Wind Data at 50 Meters

Tabular Data Calculation Using Closest Data Point Within 1 KM.							Weibull Parameters	
Direction:	Frequency:		Power:		AVG. Wind Speed:		c	k
N	5.50	%	2.55	%	4.18	m/s	0.797	2.490
NNE	3.59	%	2.3	%	4.41	m/s	0.843	2.066
NE	2.49	%	1.43	%	4.00	m/s	0.767	1.779
ENE	2.47	%	1.48	%	4.22	m/s	0.806	1.944
E	3.58	%	2.39	%	4.67	m/s	0.878	2.254
ESE	5.14	%	4.02	%	4.87	m/s	0.951	2.509
SE	7.06	%	7.71	%	5.30	m/s	1.033	2.244
SSE	5.79	%	5.44	%	4.82	m/s	0.949	2.008
S	6.26	%	5.82	%	5.03	m/s	0.969	2.162
SSW	7.59	%	9.54	%	5.66	m/s	1.089	2.293
SW	9.47	%	13.49	%	5.93	m/s	1.140	2.331
WSW	9.92	%	13.12	%	5.64	m/s	1.103	2.256
W	9.55	%	12.15	%	5.54	m/s	1.112	2.459
WNW	8.13	%	8.26	%	5.19	m/s	1.032	2.456
NW	6.75	%	6.38	%	4.86	m/s	1.027	2.702
NNW	6.70	%	3.92	%	4.36	m/s	0.876	2.709

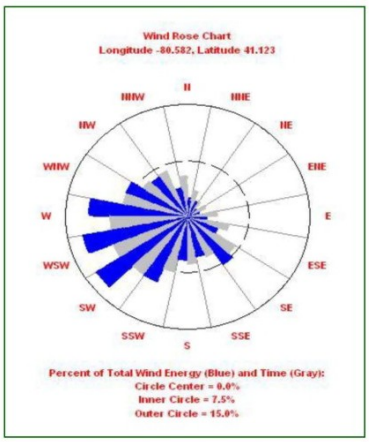

Figure 3.1-11 Directional Wind data at 50 m

The installation of the two turbines was successfully put out for bid, based on the site plan described in Figure 3.1-12.

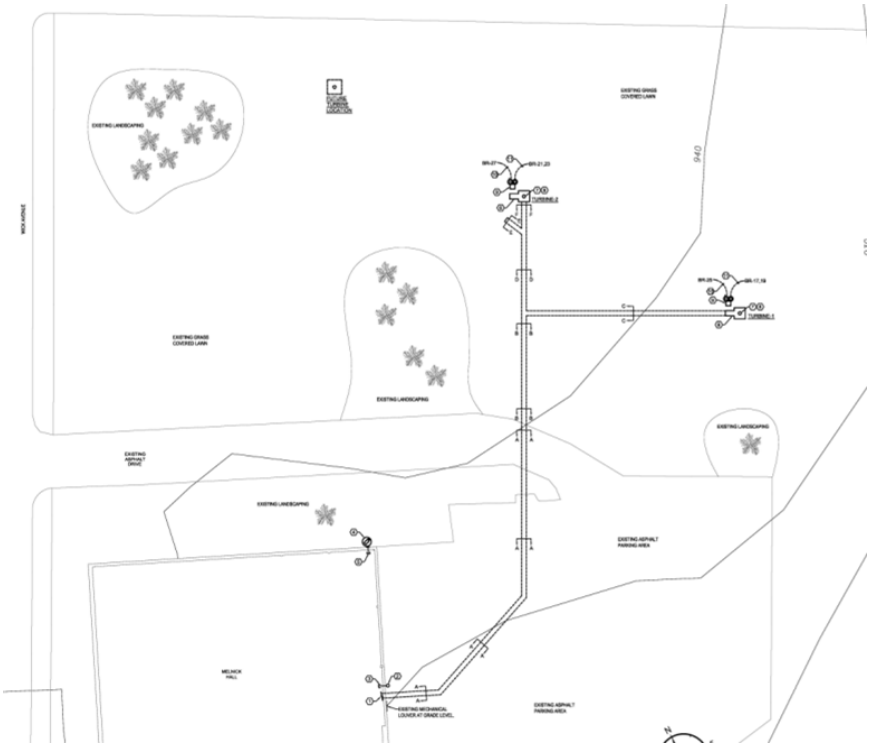

Figure 3.1-12 Approved Turbine Locations Facing West

Unfortunately, in August 2012 the DOE funding agent made YSU aware that a historical impact review was required as the proposed site is in an Ohio historical district. The team is working to prepare this significant document as quickly as possible.

YSU submitted a Section 106 Review to the Ohio Historic Preservation Office: Resource Protection and Review for the installation of the turbine near Melnick Hall. Because the Melnick Hall location was determined to be in an historic district, it was determined that additional approvals were required to install turbines on that site.

Professor Mike Costarell was awarded a sabbatical from Youngstown State University for the 2013-14 academic year. Responsibility for this aspect of the project was then assigned to Professor Ron Griswold, who oversaw the completion of the historical review. A meeting was held with the YSU representative to the Ohio Historic Preservation Office to explain the site selection process, and a letter of support from the Mahoning County Historical Society was ultimately requested and received. Professor Griswold provided many photos of the proposed turbine site during an in-person meeting with the Ohio Historic Preservation Office in Columbus, Ohio.

On Sept. 3, 2013, a letter was sent describing the site selection process, and included support from Dr. Donna DeBlasio of YSU's Center for Applied History. A separate letter of support was transmitted by H. William Lawson, Executive Director of the Mahoning Valley Historical Society. A preliminary review by our local advocates (Dr. DeBlasio and Mr. Lawson) requested that the turbines be painted to blend with the skyline colors, thereby minimizing any visual interference with the local surroundings.

On October 21, we received a response from Mr. Justin Cook, History Reviews Manager from the Ohio Historic Preservation Office. Mr. Cook supported the proposed mitigation, but requested further action to maintain the historic aspects of the region. He states:

> Mitigation in the form of a deliverable that promotes preservation objectives will be required to resolve the adverse effect in accordance with 36 CFR Section 800.6. I have reached out to Dr. DeBlasio and Mr. Lawson for information about local preservation priorities and to solicit ideas for possible mitigation deliverables that promote them. I would welcome input on this matter from others within the University, the community at large, and the Department of Energy as well. Once stakeholders have agreed on mitigation, a stipulation in a Memorandum of Agreement (MOA) will require its completion. Execution of this MOA will conclude the consultation process and fulfill DOE's responsibilities under Section 106.

Mr. Cook further recommended that DOE become more actively involved in the development of this MOA. Because there are two different installations of wind turbines, funded through two different DOE projects, coordination amongst DOE offices was required.

YSU received an MOA from Casey Strickland that was forwarded to all parties for review. The mitigation included a walking tour in May and June of 2014, which was completed in advance of our receipt of the final letter of approve. Contracting for installation of the subject turbines at the approved location was then completed.

With the installation contractor hired, pre-construction testing of the soils at the site determined that tower foundations previously thought to be adequate, needed to be redesigned. The new foundation design was approved by our engineering consultant and construction authorized.

Mobilization to the site should occur before the end of February with project completion anticipated by May 30, 2015.

The installation of the towers, turbines, and associated equipment was complete in May 2015. The weather station originally installed on Stambaugh Stadium was transferred to the Melnick Hall site and is operational. Unfortunately, in all of the construction delays, one of the wind turbine controllers was misplaced. Efforts to obtain a replacement were unsuccessful. A plan was developed to allow for operation of both towers and collection of data. The photographs below show the installed turbines in location behind Melnick Hall.

Figure 3.1-13: Photographs showing installation of wind turbines at the Melnick Hall location

Subtask 3.2: Wind Turbine Selection

Orbital and YSU worked with The Renaissance Group in reviewing several wind turbines in the 1-2.5kW power limit. Manufacturer's reputation, size, ease of use, ease of installation and price was the main driving factor in limiting the size of the turbine to under 2.5kW. After carefully reviewing the various model available in the market the team selected the ARE 110 (2.5kW). The ARE 110 provides a very long life with little maintenance due to their relatively low rotational speeds (low RPM). The turbines large swept area (10.2ms^2/110sq.ft), high-efficiency blades, purpose built alternator, and optimized power electronics ensure maximum energy capture from a wide range of wind speeds. **Figure 3.2-1** shows a typical ARE 110 wind turbine (installed).

Figure 3.2-1 – Picture of ARE110

A preliminary installation concept drawing is shown below, wherein a steel shelf or corbel is used to transfer the tower and turbine load to the concrete column, not the roof deck.

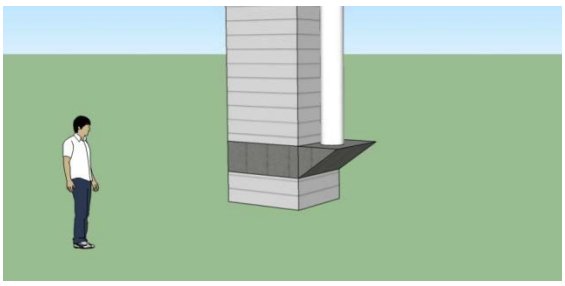

Figure 3.2-2: Turbine Tower Corbel Concept

After it was determined that the turbines could not be located on the roof of Stambaugh Stadium, a conventional installation process was developed for installation at the Melnick Hall site. Two wind turbines were installed side-by-side at the Melnick Hall site to compare their performance.

Subtask 3.3 Collect Baseline Data
A HOBO weather station was installed on the roof of Stambaugh Stadium to collect wind speed and direction information. Communication needs included a 120 kb/s internet connection to transfer wind data, web camera pictures, and power data readings to YSU faculty and corporate partner Orbital Research in Cleveland. Internet connectivity in the Stambaugh lodges is not available, and computer support need to develop and implement a communications plan.

The system three-dimensional anemometers, shown below, were installed and utilized for the initial collection of wind speed data.

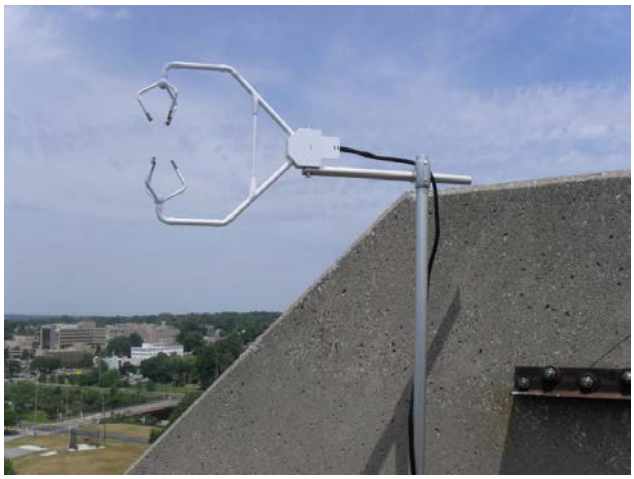

Figure 3.3-1: YSU 3D anemometer installed on the stadium

Initial observations from this information have a few trends. First, the data is comparable to that from off-campus sources. The data shown below in red is from the YSU stadium, elevation 1145 feet above sea level (FASL), while the data in blue is from a site on the west side of Youngtown, elevation 1004 FASL. The data at the YSU station was similar to the off campus data below 12 miles per hour and diverged above this value.

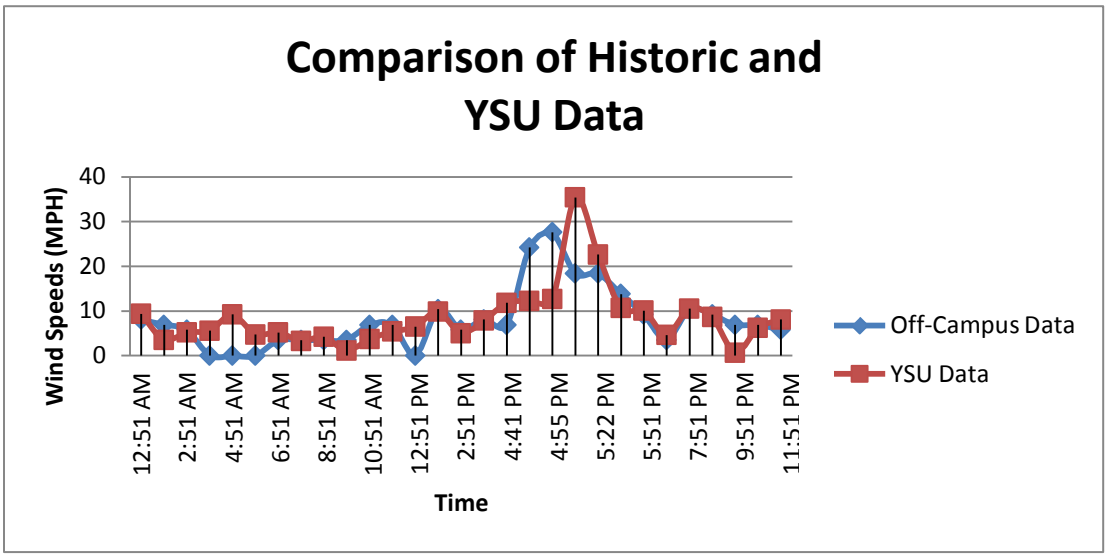

Figure 3.3-2

Second, the wind profile near the stadium shows significant change due to the land and the structure. One key assumption in turbine design is that the wind approaches in a uniform plane that is perpendicular to the turbine. However, buildings and other permanent features change the direction of the wind, sometimes with the adverse effect of lift and drag characteristics of the airfoils.

As shown in the Figure 3.3-3 below, the vertical component of the velocity was at times 15 to 30% of the total velocity when viewed as fraction of vertical velocity (V_z) to the total velocity (V). When interpreted as an angle, the effective velocity, angle of attack, and therefore lift and drag properties are much different than assumed.

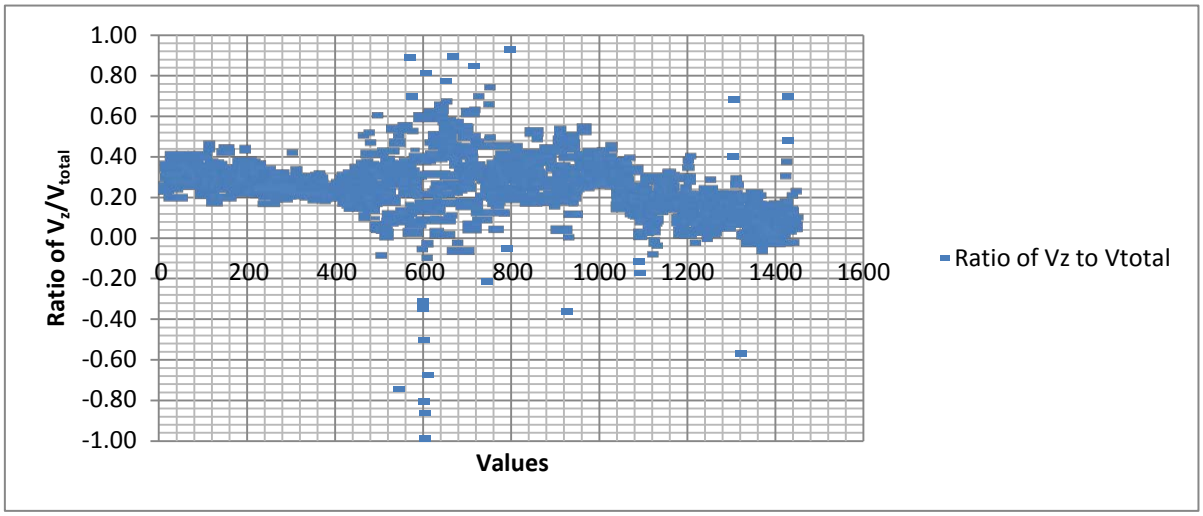

Figure 3.3-3: Ratio of Vertical Velocity to Horizontal Velocity

During the period prior to final installation at the Melnick Hall site, GET installed a portable anemometer at the location to begin collecting wind speed data. Figure 3.3-4 shows a sample of the data collected every fifteen minutes between September 10 and 30, 2014. The average for this time period was 4.7 mph.

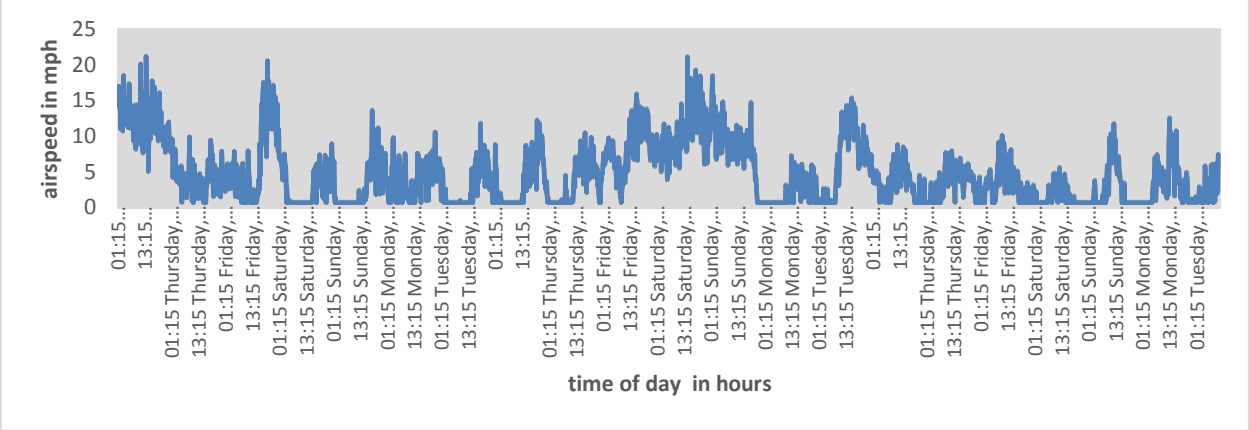

Figure 3.3-4 Sample Wind Speed between September 10 to 30, 2014

Subtask 3.4 Conduct System Analyses
Because of the long delays associated with the installation of the turbines, it was determined that this task would be combined with other subtasks. As a result, no separate analysis of the wind turbine systems at the ultimate Melnick Hall site was completed.

Subtask 3.5: Evaluate and Optimize Aerodynamically Enhanced Turbine Blades
Work under this subtask was conducted to evaluate three potential prototype designs via computational and experimental programs. A trade study of the merits of each approach was initiated to down select promising designs to one for fabrication. The final prototype will be installed on one of the turbines located at YSU for testing.

The following figure shows concepts of three methods under evaluation for aerodynamic enhancement of the turbine blades.

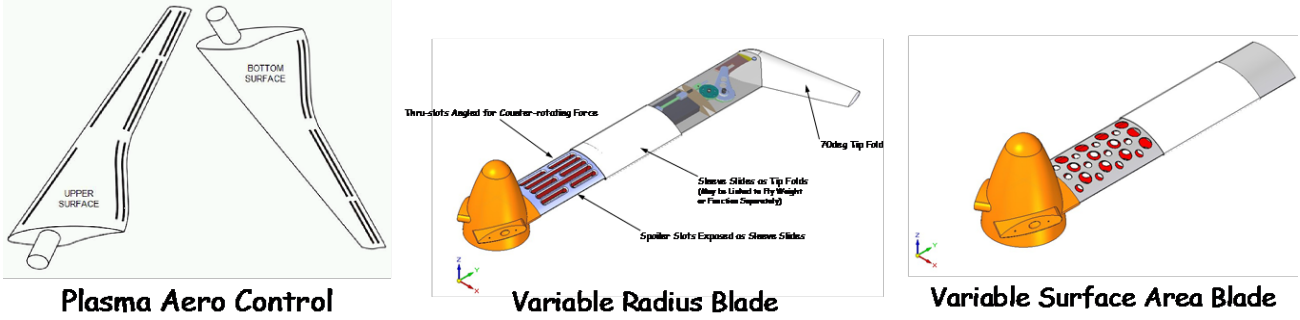

Figure 3.5-1: Concepts of various methods for enhancement of the turbine blade designs.

Modeling

Orbital Research explored several technologies to increase the performance of small wind turbines. Two of these technologies have been modeled in computer simulation using MatLab. The first technology is a variable radius system that allows the wind turbine to expand its radius at low speeds to capture more energy and then as the turbine achieves near optimal rotational speed for power generator the system passively reduces the blade radius to keep the turbine at near constant speed over a range of wind speeds. The second technology is a plasma actuator applied to the leading edge of the blade. This plasma actuator affects the lift and drag characteristics of the blades at low angles of attack, increasing the efficiency of the turbine by virtual shaping of the blade. The third technology, a variable surface area system, has been conceptualized and will be analyzed in the near future.

The base-line turbine is a model based on the performance specification of the ARE-110, 2.5 kilo-watt, 1.8m radius, 3 bladed turbine. For comparison the variable radius model and plasma model are compared to the model of the ARE-110 and use the same generator model. This is to model the idea that we will be retrofitting the ARE-110 turbine with the new blade system. The lift and drag coefficient for the model are an approximation and the same lift to drag coefficients (ie the same foil shape) is used on the two technology demonstrates being compared to the ARE-110.

The variable radius model is conceived such that the radius of the turbine disk can change from a maximum of 2.5m down to 1.8m. This would be implemented by a blade that has a telescoping section to increase the radius of the blades. This is a ~40% increase in radius from the base line. The system utilizes a counter mass, spring and damper system to passively control the radius of the blade. The model system was designed to begin retracting the blades when a shaft speed is ~1.7% below the designed input speed for the generator and finish full retraction of the blades at 1.1% over the designed input speed of the turbine. It is assumed that if shaft speed were to continue to climb after full retraction the shaft speed is then controlled with the system usual brakes and furling mechanisms.

The plasma system uses a single dielectric barrier discharge plasma actuator that injects momentum into the boundary layer of the air flowing around the airfoil. This technology requires custom design airfoils to work most effectively. In the model presented here the same lift and drag coefficient curves are used as the above but with modification to simulate the potential change, a similar but plasma enabled airfoil would achieve. The changes for the particular placement of plasma actuators modeled are a small increase in coefficient of lift and small decrease in coefficient of drag at low angles of attack.

Power curves for the three models mentioned above are shown in Figure 3.5-2, below. The baseline (ARE-110) model, the variable radius model and the plasma enable model. This figure shows the power produced (watts) by each model at a given wind speed (m/s).

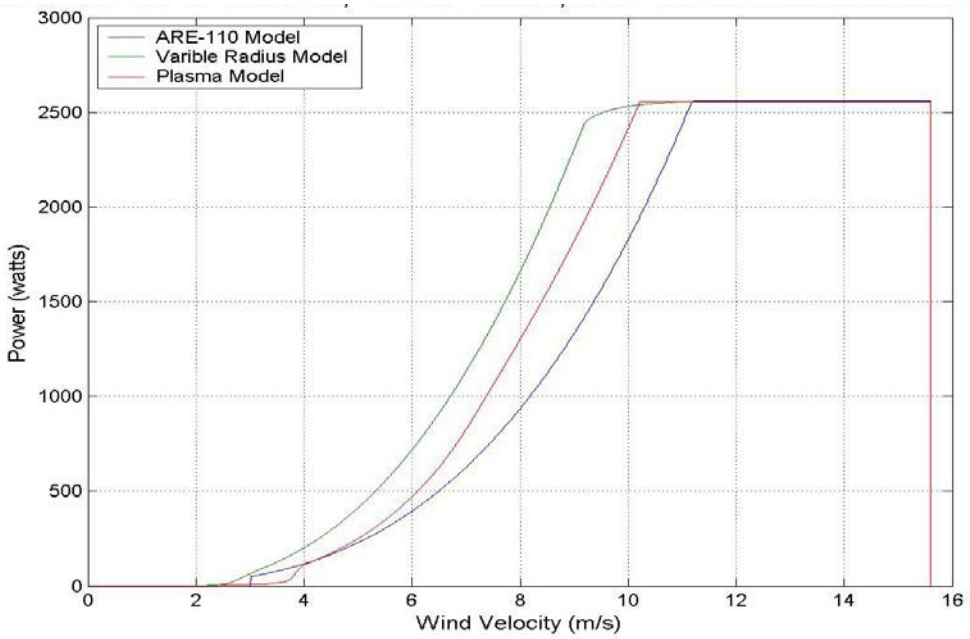

Figure 3.5-2: Graph showing power curves for the three turbine models.

The results of additional modeling indicate a considerable increase in energy production. Figure 3.5-3 below shows the power curves from Figure 3.5-2 multiplied by the Weibull probability curve of each wind speed, based on wind survey data from the YSU wind turbine site. The figures in the upper right hand corner are the expected monthly total power produced in kW-hr.

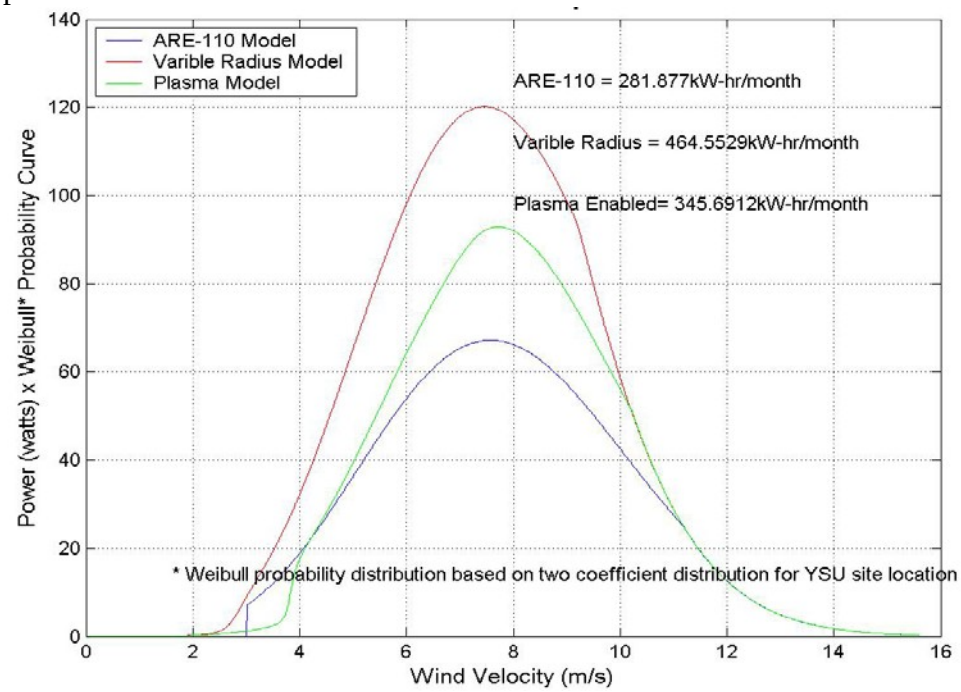

Figure 3.5-3: Expected power output based on blade characteristics and local wind conditions

Both curves generate an encouraging 23 to 65 % increase in energy generated per month.

Wind Tunnel Testing (University of Toledo subcontract)

The wind tunnel models of turbine blade sections were fabricated and sent to University of Toledo. A description of the blade profile used for testing is shown in Figure 3.5-4.

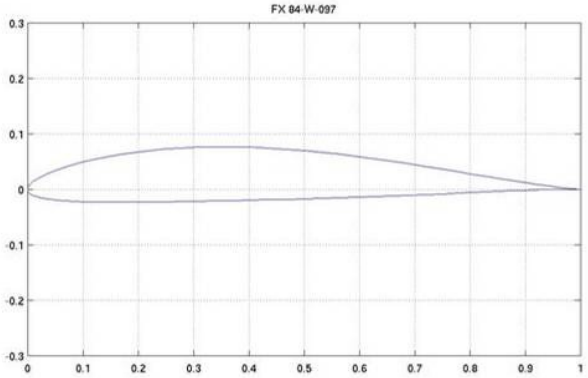

Figure 3.5-5a: Blade profile used to build the wind tunnel model for evaluation of plasma flow effectors.

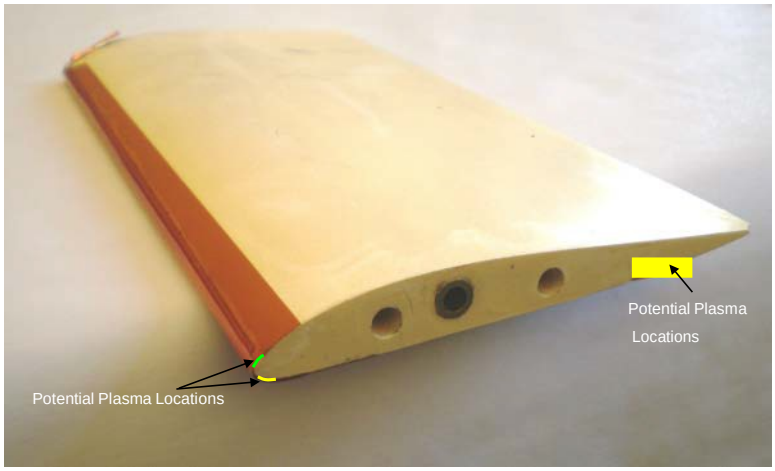

Figure 3.5-4b: Photo of the blade wind tunnel model showing the location of plasma devices.

Work was initiated at University of Toledo through the development of a test plan and experimental setup, as shown in Figure 3.5-5).

Figure 3.5-5: Air Foil Cross-Section Mounted In University of Toledo's large cross section Wind Tunnel.

In the initially proposed set up, the airfoil cross section was place in the U. Toledo's 3ft x 3ft wind tunnel cross section. Shakedown tests were performed to ensure integrity of the experimental setup. During these tests, high frequency radio frequency (RF) signals generated by the plasma generation unit were noticed in the data acquisition (DAQ). This RF signal was significant and interfered with the wind tunnel hardware (stepper motor used to change the angle of attack) and the load cells used for force and moment detection. The plot in Figure 3.5-6 illustrates the strength of the RF signal. The plot shows the non- dimensional calibration curves for the force balance/load cell setup. For a known set of weights, these curves should be similar for both the plasma OFF and ON cases. The plot in Figure 3.5-6 clearly suggests otherwise. The unwanted RF signal impeding the electronic balance/load cell setup necessitated an alternative testing method.

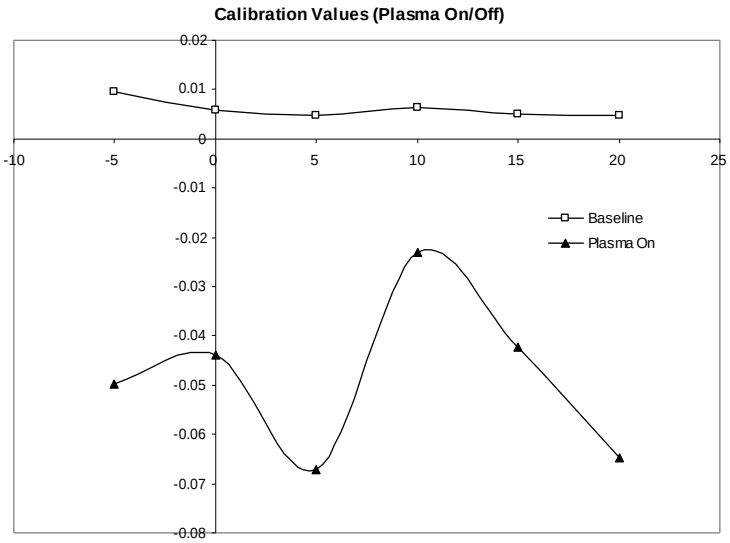

Figure 3.5-6: Calibration Values Comparing Baseline to Plasma on Values. Calibration values for both plasma on and off, under good testing conditions, should be relatively similar; these are not.

This balance and wind tunnel does not use electrical signal for data acquisition or wind tunnel control and therefore does not have interference issues from the plasma system. The mechanical force balance has a smaller resolution compared to the electronic load cell/strain gage and can measure smaller changes to the lift and drag on the airfoil, which will be beneficial at lower speeds. Figure 3.5-7 and Figure 3.5-8 shows the modified mechanical force balance and wind tunnel along with the acquired baseline data.

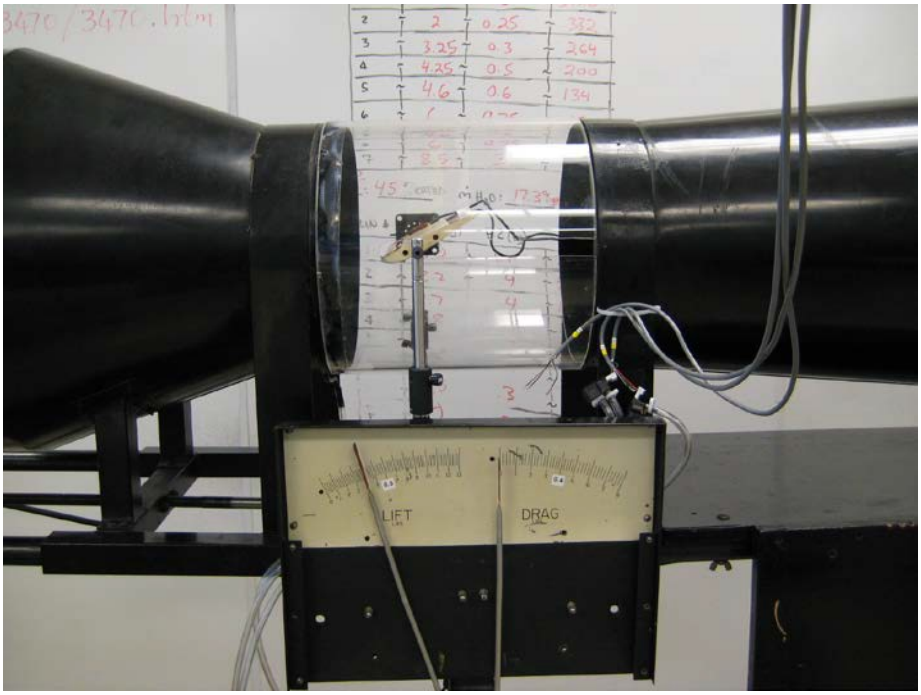

Figure 1.5-7: Mechanical force balance.

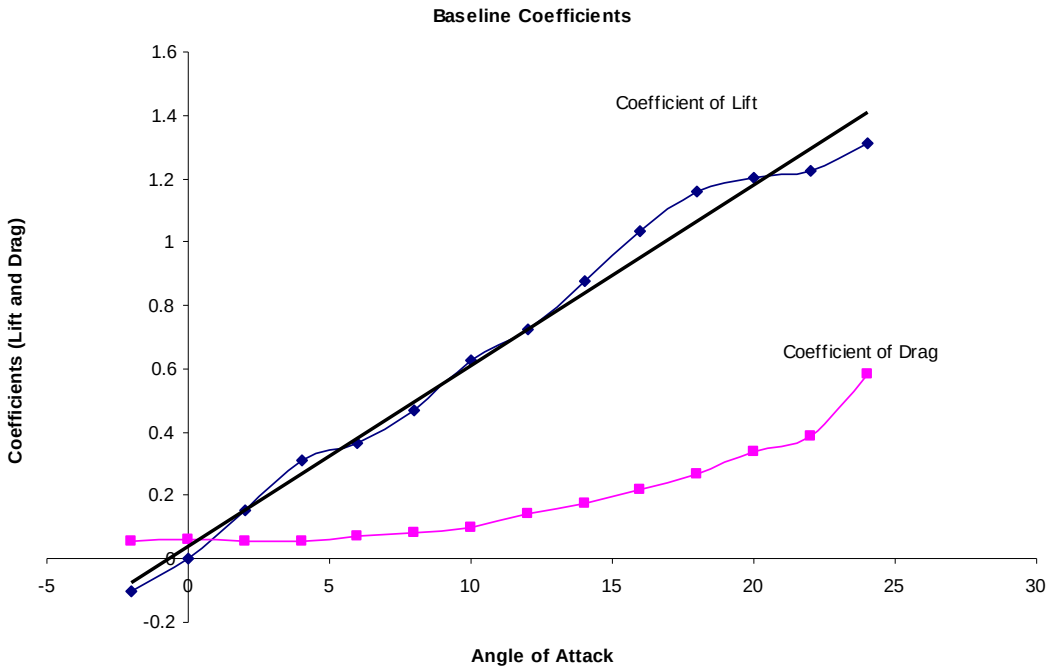

Figure 3.5-8: Baseline Data from mechanical force balance.

The experiments which consisted of wind tunnel experiments on 2-D airfoils with plasma actuators were conducted at the University of Toledo's (UT) wind tunnel. The initial plan of the experimental study was to conduct the wind tunnel tests at the UT's 3ft x 3ft tunnel. A model was designed and built at Orbital which included plasma actuators. The actuators were installed on the lower portion of the leading edge in an effort to try and control the leading edge separation bubble. During the wind tunnel tests, the following conclusions were made:

- The model and intended test speeds were small for the size and normal operating speed of the wind tunnel. The resulting aerodynamic forces were relatively small and difficult to measure accurately with the normal wind tunnel balances.
- The high voltage AC signal generated significant RF noise, which significantly interfered with the wind tunnel force balance and load cells, thereby affecting the force balance output. Efforts to eliminate/minimize the RF noise by shielding the leads by creating a Faraday cage were largely unsuccessful.

To mitigate the above concerns, it was decided to relocate the test to a 12" diameter wind tunnel at UT. The 12" wind tunnel test section setup is shown in **Figure 3.5-9**. The reasons for using a smaller wind tunnel are the following:

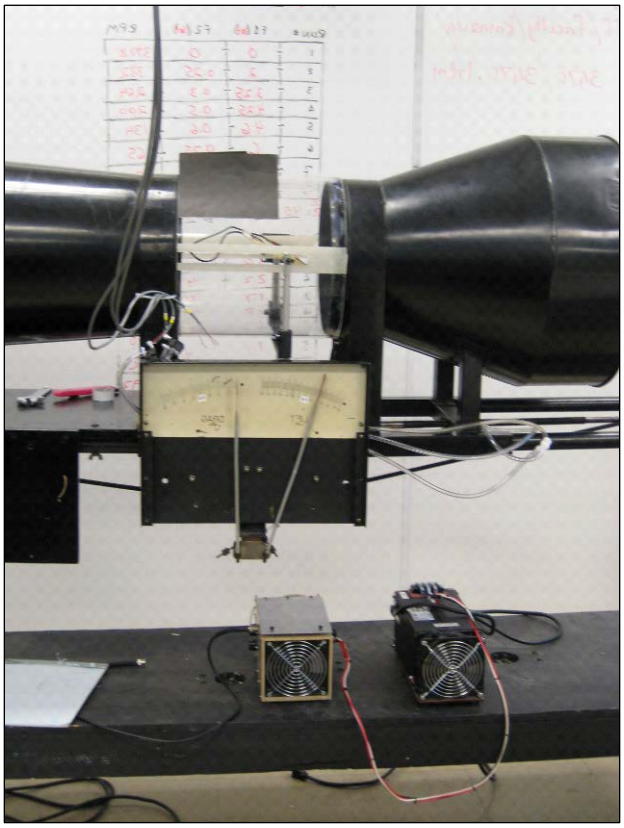

Figure 3.5-9: UT's 12" Wind Tunnel Test Section

- The tunnel is designed to operate at the speeds of interest for testing. The size of the tunnel also matched that of the model very well
- The tunnel has a fully mechanical force balance that would not have noise issues from the high voltage AC signal.

A limitation with the mechanical balance was that the resolution was not as fine as the electronic ones used in the larger tunnel. Since any improvements smaller than the balance resolution will represent minor improvements, it was decided that this limitation was negligible. **Figure 3.5-10** shows the airfoil in the 12" wind tunnel test section.

Figure 3.5-10 Airfoil model in the wind tunnel

Two plasma actuator concepts were tested. The first was to control the stagnation line with a plasma actuator on the windward (lower) surface near the leading edge. The second was to control the circulation at the trailing edge. The setup for the latter is shown in **Figure 3.5-11**. A semi-circular trailing edge is formed by embedding a brass rod along the trailing edge of an airfoil. A plasma actuator is placed on the top of the trailing edge for increasing circulation, and another on the bottom for reducing circulation.

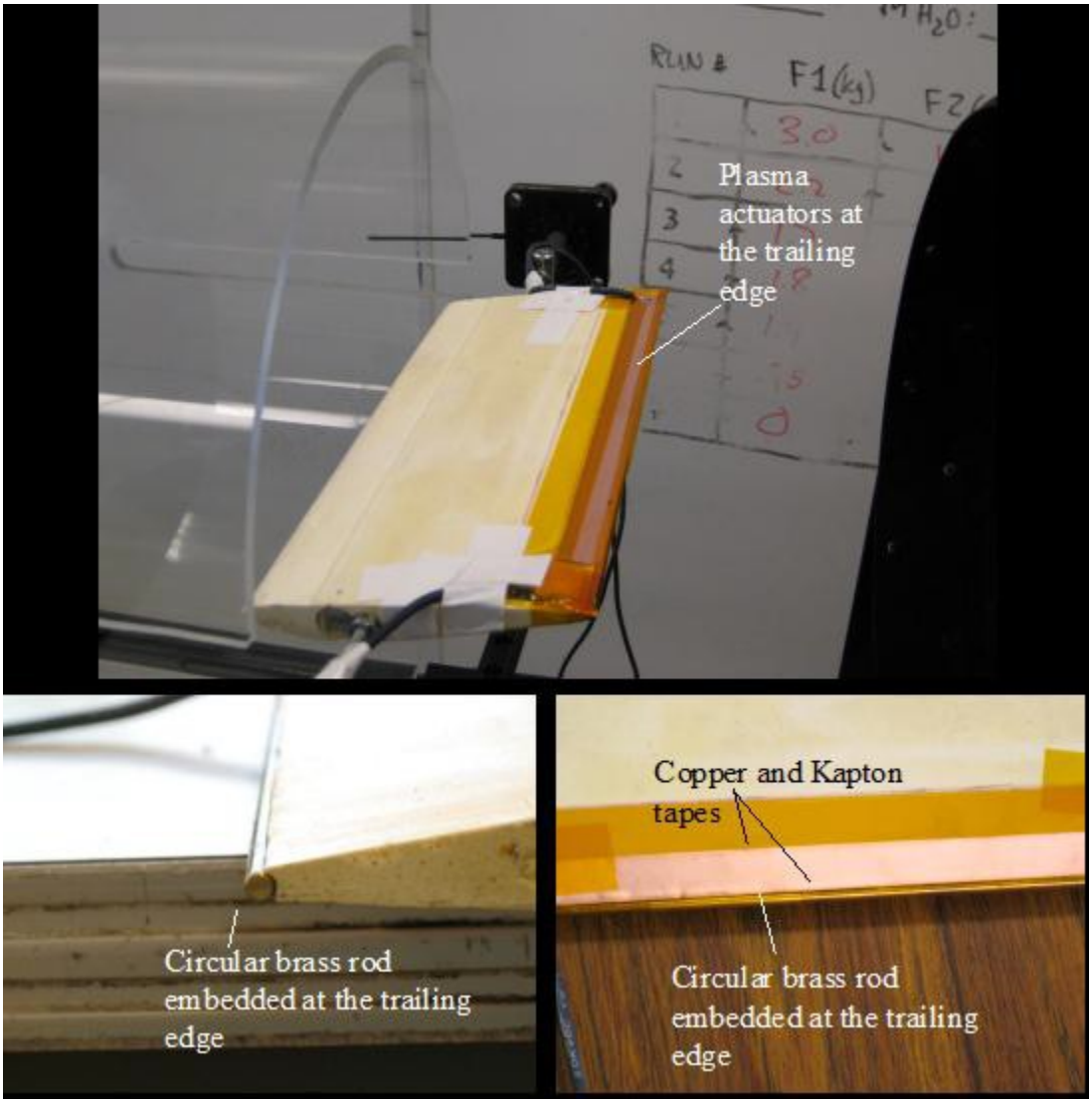

Figure 2.5-11: Plasma actuator for circulation control on the trailing edge

Plasma actuator wind tunnel tests were performed with the following conditions:

- Airfoil Geometry – HS 2412b
- Model size – 6" chord x 12" span
- Wind speed: 12m/s (27mph)
- Balance: Mechanical lift and drag balance
- Plasma setting: $9kV_{p-p}$, 50% duty cycle and 132Hz modulation frequency

Figure 3.5-12 shows the lift and drag results for the airfoil model with leading edge plasma control. The error bars shown include only the uncertainty due to the balance resolution. Small increases in lift and reductions in drag can be seen for the plasma cases. Similar effects can be seen from **Figure 3.5-13** which shows the lift and drag results for the airfoil with trailing edge circulation control using plasma actuators.

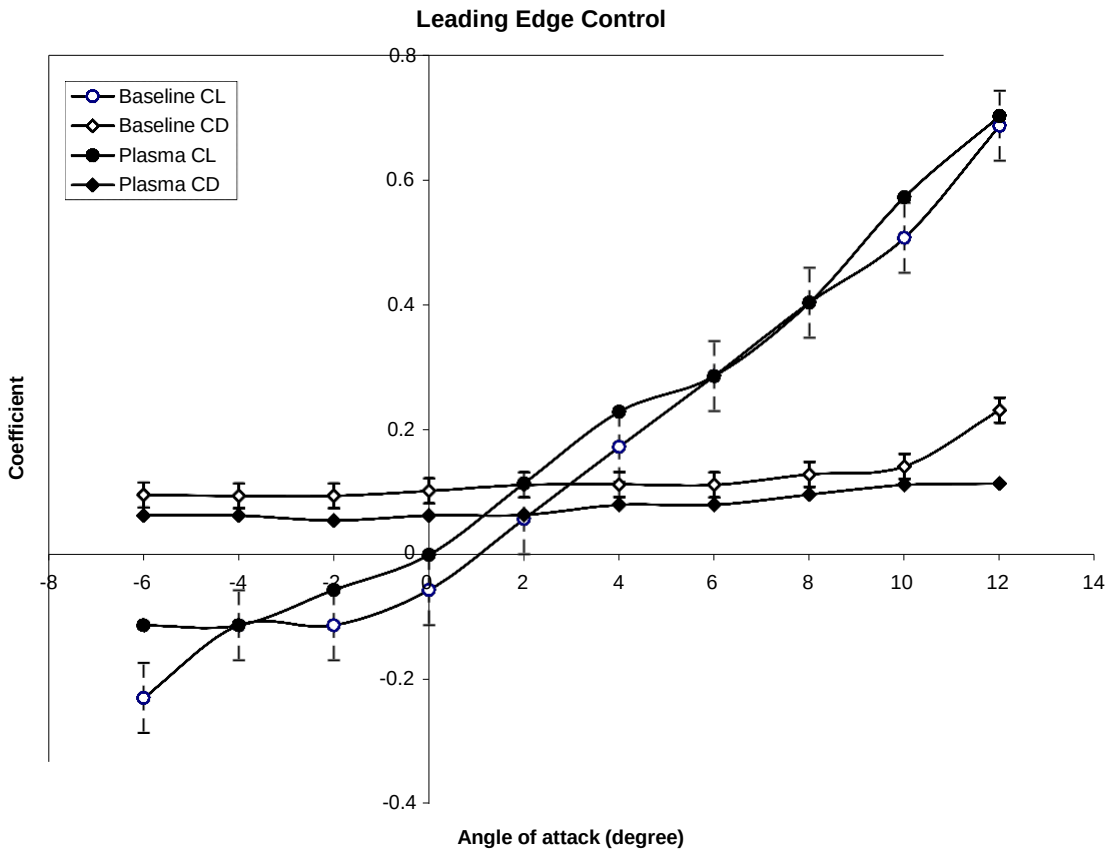

Figure 3.5-12: **Lift and Drag coefficients of the leading edge control plasma actuator**

From these tests and previous wind tunnel tests conducted by the Orbital team, the effect of plasma actuators to improve the aerodynamic characteristics of airfoils has been demonstrated. However, the use of plasma actuators poses significant challenges which are discussed below.

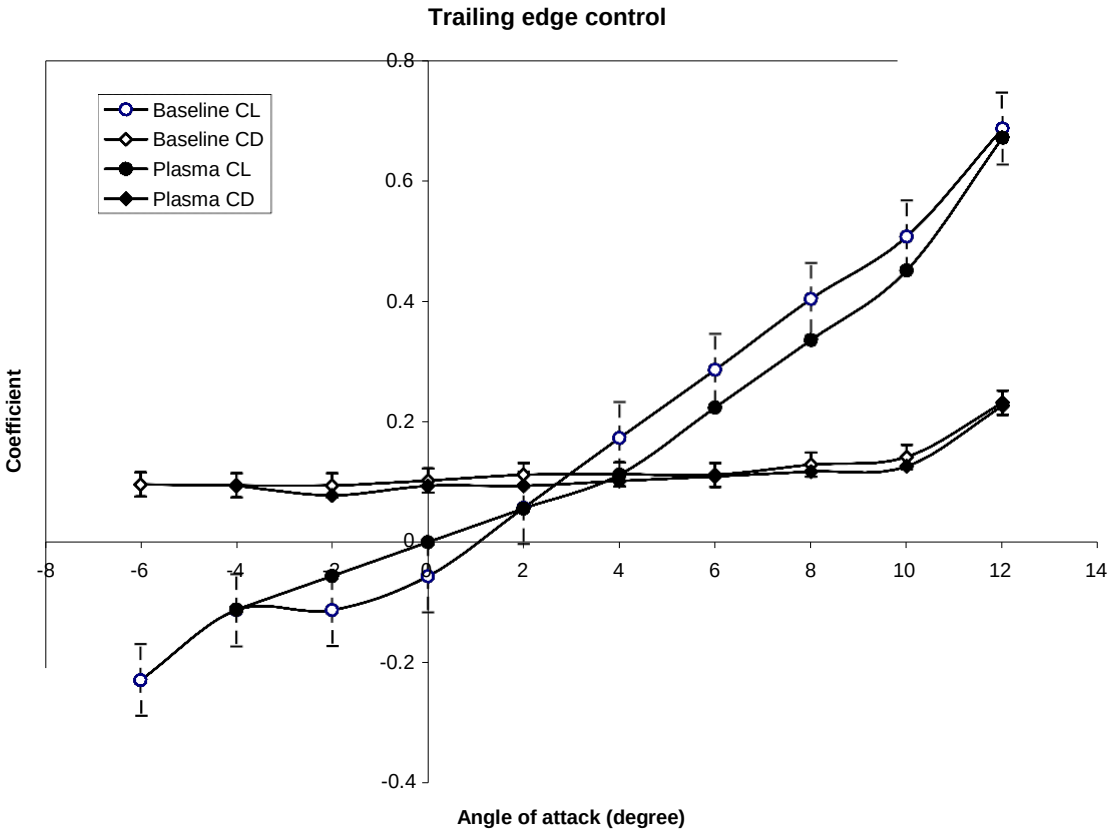

Figure 3.5-13: Lift and Drag coefficients of the trailing edge circulation control plasma actuator

Although plasma actuators demonstrated effectiveness as a flow control device to improve lift, reduce drag, control separation, delay stall, reduce buffeting and noise, the practicality of their use for real-world applications has not been demonstrated.

The materials used to build plasma actuators for most research purposes are copper as the main electrode material and Kapton, Macor and Teflon as the dielectric material. They are typically available as tape from most industrial suppliers. A plasma actuator made up of tape will most definitely not survive on a wind turbine for any sustained operation. The plasma actuators made of the tapes mentioned above are highly susceptible to arcing or punching through and are extremely sensitive to edge gap, surface preparation, cyclic loading, bending and stretching. Until more robust materials are identified, the use of plasma actuators for practical applications, especially on a wind turbine is not feasible.

Due to these factors, the Orbital team decided to design and develop a mechanical flap system as the flow control device to improve wind turbine efficiency.

Mechanical Flap Design Evaluation

Orbital completed a mockup of the variable radius blade, thus demonstrating the feasibility of a purely mechanical approach to changing the blade length and thereby increasing the energy capture of the blade. If the behavior model suggests that this approach is best, a dynamic model of the blade actuation while rotating will be prepared, so that the spring constant and dampening factors for the final turbine demonstration can be specified.

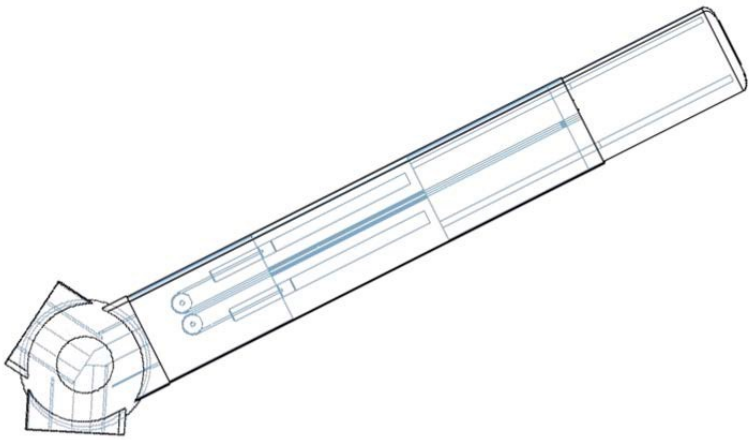

Figure 3.5-14a: Solid model of Variable Length Blade

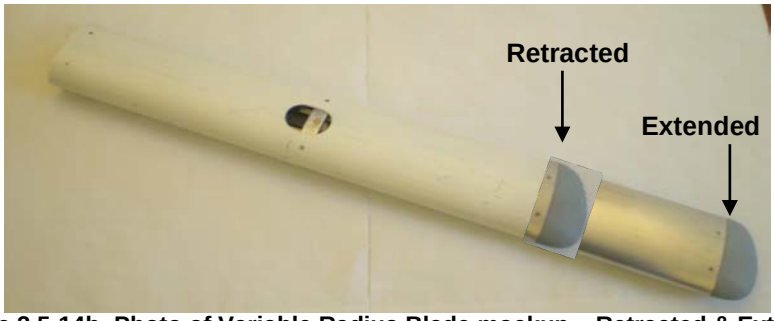

Figure 3.5-14b: Photo of Variable Radius Blade mockup – Retracted & Extended

Figure 3.5-14c: Photo showing some of the internal mechanical components of the mock up Variable Radius Blade

Typically, a Gurney flap is a small flat tab projecting from the trailing edge of a wing/airfoil. In almost all cases, it is set at a right angle to the pressure side (bottom side) of the wing, and extends about 1%-2% of the wing chord. The exact dimension needs to be scaled according to the boundary layer. The effectiveness of the Gurney flap has been demonstrated in many practical applications such as automobile racing and high-performance acrobatic airplanes.

The Gurney flap when deployed, increases pressure on the pressure side, and decreases pressure on the suction side. This helps the boundary layer to stay attached all the way to the trailing edge of the suction side of the airfoil – thereby increasing lift.

CFD simulations were performed on the turbine blade airfoil with and without the Gurney flap to estimate the amount of lift increment. 2-D CFD simulations were performed using Ansys as the primary flow solver at 65m/s across a range of angle of attack (-15 to +50). SST k-epsilon was chosen as the turbulence model. **Figure 3.5-15** shows the coefficient of lift versus angle of attack (alpha) for both the baseline airfoil and airfoil with 2% Gurney flap. The plot shows a significant increase in the lift coefficient across all angles. Multiple refined meshes were created by appropriately refining the mesh around the airfoil and wake to more accurately resolve the drag. In CFD the quality of the mesh can have a profound effect on the drag – as the drag is affected by wake along with separated flows over the airfoil, whereas the lift is a function of flow over the geometry.

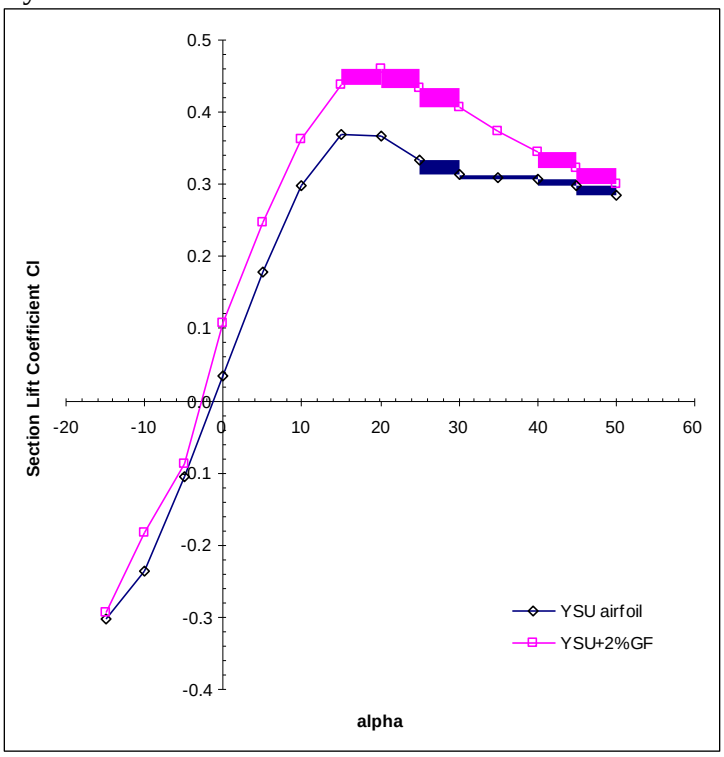

Figure 3.5-15: Coefficient of Lift vs angle of attack

Figure 3.5-16 shows velocity contours around the baseline airfoil (above) and the airfoil with 2% Gurney flap.

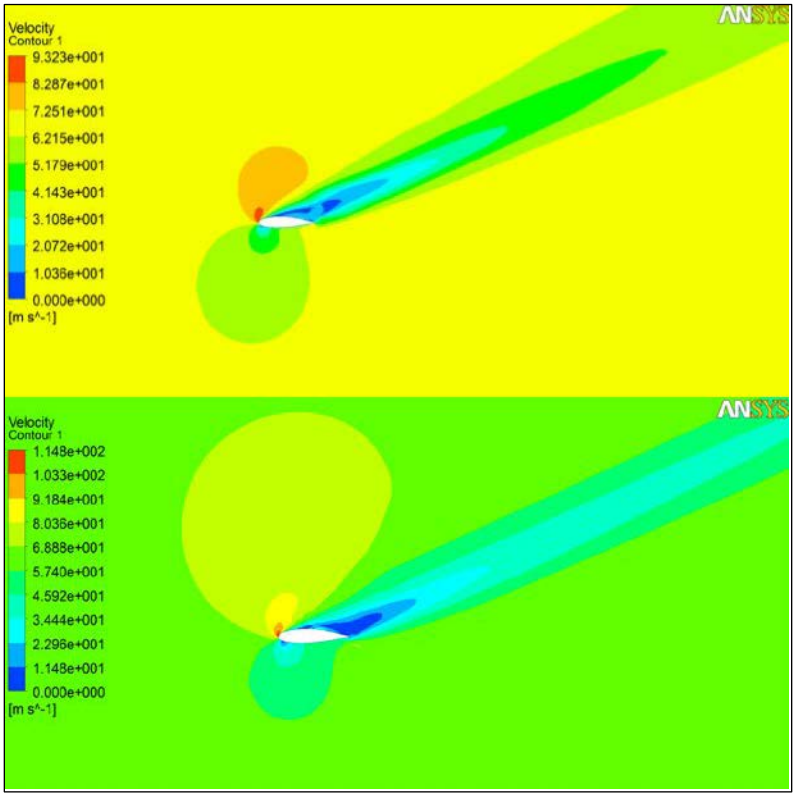

Figure 3.5-16: Velocity contours around baseline airfoil (top) and airfoil with 2% Gurney flap (above)

In conjunction to the simulations, Orbital also designed and built a Gurney flap mechanism for the wind turbine blades. **Figure 3.5-17** shows the design of a Gurney flap on the ARE 110 turbine blade. A proof of concept model was constructed in Orbital's lab on an aftermarket turbine blade.

The model is of a Gurney flap design which is an "all on or all off" deployment type. There are no intermediate positions. A variety of materials are being used with consideration being given to low mass and corrosion resistance:

- Stainless steel (22 gauge)
- 2024 & 6061 Aluminum
- Nylon 6/6

The flap itself is a modified stainless steel hinge section which will give a 0.375" deployment height. The mechanism was designed to present the lowest profile possible when stowed, and will be located on the leeward side of the blade at the trailing edge. Aluminum tracks at each end of the flap will direct the flap motion and offer support for the flap.

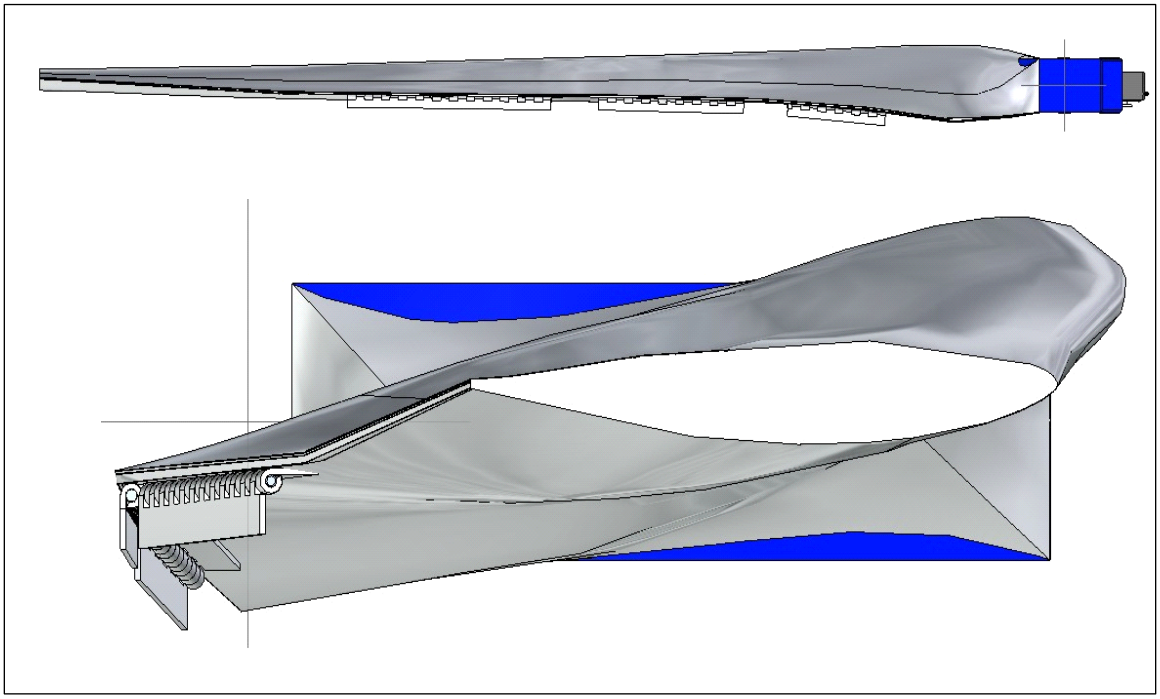

Figure 3.5-17: Gurney flap design on the ARE 110 turbine blade

A high torque RC servo is used as an actuator for the flap mechanism. A sheathed pushrod will be attached to the servo bell crank at one end and to the flap bell cranks at the other end. The servo will be located in the open area of the hub near the base of the blade. A small diameter hole will be drilled through the blade to communicate the hub area to the blade surface to allow fitting of the pushrod. (see **Figure 3.5-18)**

Figure 3.5-18: Lab prototype of the Gurney flap mechanism

The Gurney flap mechanism uses three standard servos to drive the flaps on each blade. A microcontroller controls each servo independently, since some servos require separate calibration. An accelerometer is used to determine the rotational rate of the wind turbine, and a Zigbee module allows the unit to communicate to ground station.

The entire circuit is powered by a 2,200 mAh Lithium-Polymer battery pack. The battery pack is charged by an on-board generator which produces 9 volts. When the circuit is not in use it goes into sleep mode, disables the Zigbee transmitter, and disables power to the servo motors. Periodically the circuit will wake and determine if any function needs to be performed. A block diagram of the circuit is shown in Figure 3.5-19.

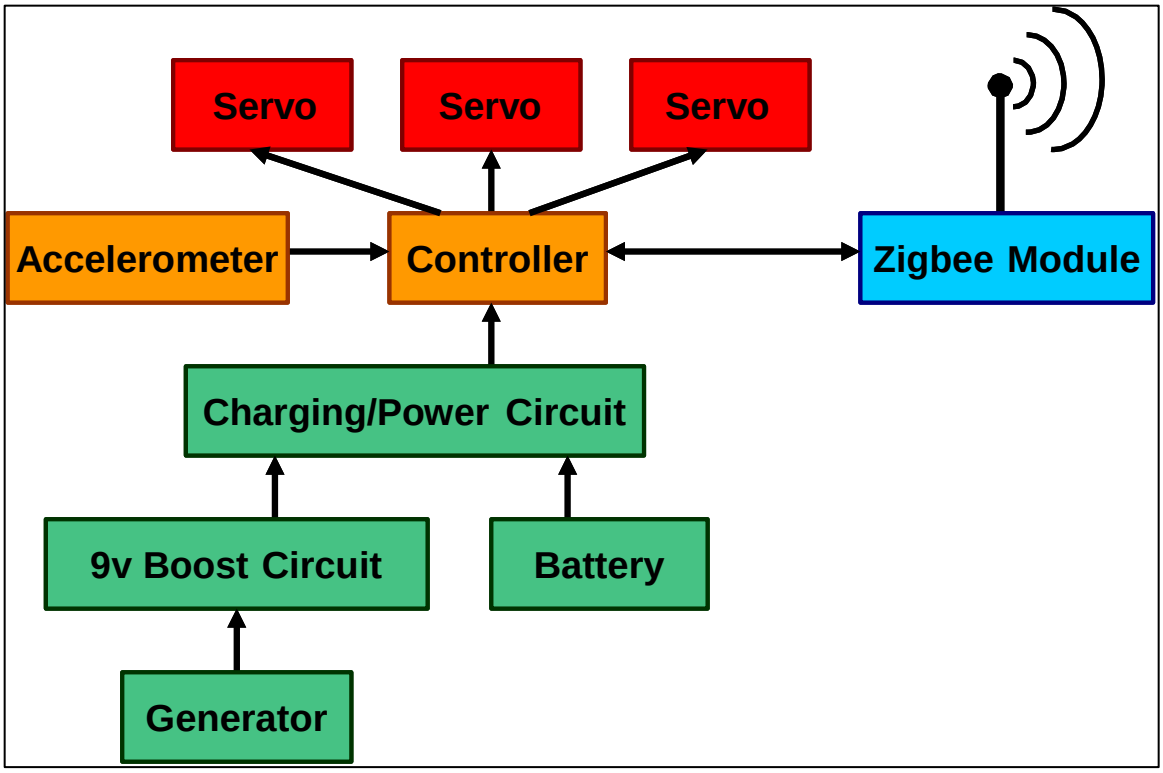

Figure 3.5-19 - Gurney flap Servo Driver Block Diagram (Red- actuator; Orange-control; Blue - communication; Green-Power)

The gurney flap mechanism on each blade is controlled by three independent servos. The electronics control each blade's servo position based on the current spin rate of the wind turbine, which is measured by an onboard accelerometer. A large 37 Wh Lithium-Polymer battery powers the electronics and is also housed in the enclosure. The electronics module communicates with a ground station with an attached low-power Zigbee transceiver, allowing manual control of the servos.

The entire system is 200mm long, 66mm tall, and 90mm deep excluding the external connections. All external connections are made with water-proof connectors and all critical components are protected from moisture and are mounted in a water-proof (weather-proof) container.

Figure 3.5-20 on the next page shows the servo controller unit.

Figuze 35-211- Gurney llap suvocoi\DIIer(...,);wilhbaUery(n..W.);wilhw roof .,..,...,..,..W
Q:loUonl)

The fabrication of the Gurney flap mechanism was completed. All three mechanisms have been installed on the blades as can be seen in Figure 3.5-21. Servo motors to actuate and control the Gurney flap mechanism were installed at the root of the wind turbine blades. A shroud to cover the linkage was also designed.

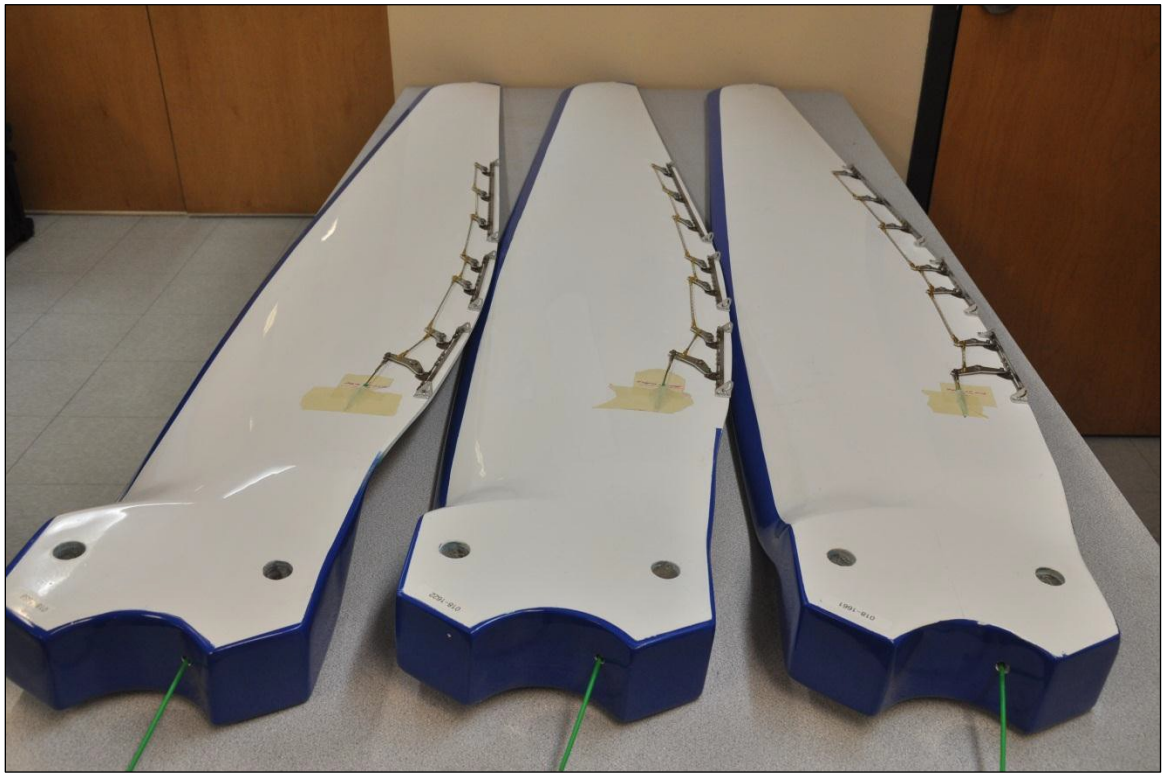

Figure 3.5-21 – ARE 110 Wind turbine blades with Gurney flap mechanisms installed on their trailing edge.

Subtask 3.6: Evaluate System Performance of Enhanced Blades

Due to delays in the installation of the wind turbines, no actual data was obtained within the contract period. At this time, the turbines are installed and operational at YSU with standard blades. We are in contact with Orbital Research and in discussion as to how best the required data can be obtained. YSU is seeking a faculty resource that can work with facilities staff to install the Orbital blades, collect the required power performance data, and work with Orbital staff to complete analysis of these results.